UNIVERSITA' DEGLI STUDI DI PADOVA
Dipartimento di Ingegneria Industriale DII

Corso di Laurea Magistrale in Ingegneria dei Materiali

GMAW, SMAW and GTAW weldability assessment of high-silicon bainitic TRIP steel

Supervisor: Manuele Dabala'

Student: Edoardo Bregolin 2021047

Academic year 2021/2022

...alla mia famiglia

Abstract

The thesis work consists of verifying the weldability of a bainitic TRIP steel through GMAW, SMAW and GTAW processes using conventional high-strength commercial filler metals. The project was carried out in cooperation with INE S.p.A., which provided all the services and materials needed to perform the welds. The weldability of the steel was evaluated by visual inspection with penetrant dye liquid and metallographic characterization using optical (OM) and scanning electron microscope (SEM). The analysis was focused on the detection of hot and cold cracking in welded materials, residual stresses caused by welding processes, hardness properties of thermally affected zones, identification and quantification of microstructural components, that were examined by XRD diffraction. The welded specimens were then subjected to austempering heat treatment in order to obtain the characteristic bainitic structure of the steel studied. The mechanical properties of the welded specimens (yield stress and UTS) were estimated by tensile tests.

The results obtained are promising: critical events, compromising weldability, as hot and cold cracking did not occur, defects generated on the weld bead or on the plates' surface, when subjected to welding processes.

Index

0. Introduction

This experimental thesis work concerns the analysis of the weldability of a medium carbon, high silicon carbide free bainitic steel, assisted by TRIP effect (transformation induced plasticity), which belongs to the AHSS (Advanced high strength steels)

This steel grades, in recent decades, achieved more and more attention from the industrial sector and in particular from the automotive one. The main reasons for that are the incredible values of mechanical strength that match also with a high ductility and toughness. These characteristics make these steels serious candidates for uses where both a high failure resistance and stiffness must be accompanied by a markable deformable behaviour.

The high and balanced mechanical properties of a metal are not enough to ensure a good use in exercise, it must be also prone to undergo the usual industrial processes to make complex structures. The principal process that permits to obtain systems with more than one metal part join with others is welding. Welding processes are joining processing that are characterised by several critical aspects that must be taken into account during the structure fabrication. In particular, among these critical aspects, chemical composition of the base material and filler, metallurgical issues, welding techniques and parameters, are most important. Neglecting these aspects can lead to weak and unstable weld bead that would be the main reason for a further failure of the entire structure.

For example, not all the steel grades are suitable for being welded: steel weldability depends on the sensibility of the material to the localized changes in temperature that could lead, for example, to generation of brittle phases. The presence of particular alloying elements can determine the different behaviours of the steel, which could be more or less favourable to be joined with one another. Moreover, the kind of microstructure of the steel plays an important role in the formation of brittleness due to reactions with environment.

One important aspect on the determination of the weldability of the investigated steels is the analysis of the effect of silicon: silicon is necessary, in order to obtain a carbide free bainitic microstructure, because its low solubility in cementite that suppresses carbide precipitation during bainitic react in, therefore it should be higher than 1.5% (wt.%). This can lead both to advantages and drawbacks in terms of mechanical properties and, more important, in terms of the weldability.

In this study different welding strategies are analysed, considering the principal process parameters to find the best combination of them in order to obtain a stable and safe weld. This will ensure the application of this steels in a lot of industrial sectors, valorising their mechanical properties with also the possibility of building complex structures.

1. Bainitic steels

1.1 General composition and properties

In TRIP steels the main characteristic is the combination between high strength and at the same time a high ductile material. These properties can be achieved with an accurate control of the heat treatment process parameters, alloying and deformation at room temperature of the metal. The typical microstructure of this steels consists in a multi-phase system with bainitic ferrite, and a significant amount of carbon enriched retained austenite, which can be generally in form of films or blocks [1].
TRIP effect regards the martensitic transformation of retained austenite induced by application of strain. The transformation of austenite in martensite causes a markable localize work hardening effect, this postpones the insurgence of local necking and so improves the deformability of the metal at higher strain values [2]. Moreover, the increase in volume due to the diffusionless transformation of austenite cause a higher crack propagation resistance of the material in localized zone where these are initiated.
The work hardening that the material achieves thanks to the TRIP effect can be evaluated by the instantaneous work hardening coefficient *n* [2]. This is based on the correlation between the real stress and strain that are applied to the material during the tensile test.

$$n = \frac{\ln\left(\frac{\sigma_m}{\sigma_{m-1}}\right)}{\ln\left(\frac{\varepsilon_m}{\varepsilon_{m-1}}\right)}$$

Equation 1 Work hardening coefficient

The higher is the value of the work hardening coefficient, the higher is the deformability of the steel. This because the higher is the capacity of the retained austenite to transform into martensite and so achieve greater values of deformation without failure.
The morphology of retained austenite plays an important role in terms of TRIP effect: in fact, blocky austenite is the most prone to exhibits TRIP effect because its lower mechanical stability, related to its large size and lower carbon content. The blocky grains of austenite are less rich in carbon in comparison with films, this is traduced in a lower stability of the blocky grains that have higher tendency to transform into martensite when the external deformation is applied. This causes an increase in the steel brittleness.
Thus, is derived that carbon is fundamental in these steels and microstructures: it is the main alloying element influencing the stability of the thermal and mechanical austenite [2], this is considered as the tendency of the phase to transform due to external tensile stress application. With a high

austenitization temperature and a high holding time in isothermal treatment for bainitic formation, carbon-rich blocky austenite grains are obtained. With quantity of carbon higher than 1,6 wt.% within the austenite grain, it will be very stable, and its transformation could be only achieved at very high strain values. On the other hand, if low quantity of carbon into austenite grains is achieved (as <0,6wt.%) these will transform into bainite or martensite at very low strain magnitudes with the further lack of deformability of the steel and limited TRIP effect [2]. Both these situations limit the ductility of the steel.

Other factors that influence the austenite stability are morphology and size of austenite grains. In particular, if the grain structure is coarse the transformation due to external stress applied is achieved for low strain levels and, once austenite turns into martensite, cause the formation of long needles as long as the generation grain with a tremendous increase in brittleness. On the other hand, the smaller grains are more stable so higher values of strain must be reached in order to achieve the work hardening of the steel [2]. So, also in both these situations the material toughness is limited.

For obtaining an efficient TRIP effect the control of the retained austenite properties is fundamental. One indirect factor that controls the thermodynamical stability of the retained austenite is the austenitization temperature [3]. This could be seen in results of XRD tests [3] where the necking site of tensile test's samples and its retained austenite content is analysed. It could be stated that at certain values of the austenitization temperature, the fraction of retained austenite that remains in the necking site after deformation changes. In particular, it is found that with low austenitization temperature the reduction of the retained austenite quantity in the microstructure is lower than using a higher austenitization temperature [3]. Over a certain value of austenitization temperature this effect is not so evident. Essentially, as the austeinitization temperature increases a higher quantity of retained austenite transforms during deformation at room temperature which enhance the ductility of the steel due to a more markable TRIP effect [3]. This is due to an increase in the coarsening of the microstructure as the austenitization temperature increases, which cause thicker and so less stable blocky islands of retained austenite at room temperature.

This microstructure is generally obtained with a two-steps heat treatment named "austempering". This consists in the austenitization of the material for a certain time at certain temperature and successively rapidly cooled, to avoid reconstructive transformations, at temperatures, generally above Ms, and held isothermally in order until the completion of bainitic transformation. After that the material could be quenched or cooled in air without problems of undesired transformations.

Concerning the effect on the alloying element the presence of high and middle quantity of carbon enhanced the hardenability of the steel and, as previously described, increases the thermodynamical stability of austenite at room temperature.

Another important alloying element is silicon, its principal function is the prevention of formation of carbides in the bainitic ferrite grains, these would form consuming carbon from the austenite grains which would result depleted and less stable. Moreover, it avoids precipitation of carbides makes the metal tougher with high deformability and low brittleness.

Silicon plays a crucial role in the process of microstructure's generation: it has a very low solubility in the cementite, so it reduces its value of formation's free energy, so it creates a poor environment for cementite which will not precipitate into the bainitic ferrite laths. Essentially, silicon enhances the lag between the formation of bainitic ferrite and precipitation of carbides, which happens at low heat treatment temperatures [4]. Moreover, silicon retards the precipitation of cementite also during the tempering of a hypothetical martensite present in the microstructure, this would limit the brittleness of the further material with an earning in ductility [4]. The presence of silicon in the alloy is favourable also from the point of the welding process, this because it's a strong deoxidizer and could prevent the formation of defects and porosity on the weld bead. So, due to this obstacle to the formation of cementite in bainite, the retained austenite and in particular the film ones will be very rich in carbon. This promotes a further thermodynamical stabilization of these zones.

The same low solubility of silicon in the cementite characterizes also aluminium. Thus, it promotes the generation of carbide-free bainitic ferrite as silicon. The main advantage of using aluminium as alloying element in comparison with silicon, is the lower oxidizing tendency. This could be a strong advantage in particular for the reduction of generation of defects during welding processes. On the other hand, as the content of aluminium increases the Ms temperature also increases. This is traduced in a limited range of bainitic transformation temperature of the isothermal stage, so very fine bainitic microstructure is more difficult to be obtained.

Another important alloying element for these kinds of steels is manganese Mn. This plays a role of stabilization of the retain austenite at room temperature, it reduces the transformation curves temperatures of Bs and Ms. Moreover, it is a strong deoxidizer and desulfurizer so it will be useful also in the welding process to prevent the formation of porosity and hot cracking phenomena.

This particular microstructure led to achieve exceptional mechanical properties as hardness up to 690 HV, ultimate tensile strength UTS values of 2000-2200 MPa with a total elongation of 5-30 % at room temperature [5].

The importance of the presence and the stability of retained austenite could be highlighted by tensile tests and microstructural analysis [5]. It can be demonstrated that the material failed when it reaches a certain decrease of the content of retained austenite due to its transformation in martensite or the content of retained austenite becomes under a threshold value which states that there is no more percolation of the austenite in the structure: the failure of the material and the crack initiation occur

when the austenite grains are geometrically isolated, so if they are separated between each other and transform into martensite, the cracking in these will happen very fast and easily [5]. This is because the austenite is the tougher and less brittle phase that composes the microstructure, anyway a certain quantity of martensite (from 7 to 27 %) can be tolerated before the austenite quantity goes below the percolation threshold and the failure occurs [5]. Since martensite causes lower material ductility with a higher sensibility to cold cracking, during the transformation process with external strain applied, it would be more desirable to obtain the transformation of austenite in carbon-oversaturated bainite.
The great mechanical properties, given by the combination of high tensile strength and markable deformability, are not enough to ensure a complete industrial application of this steel. In fact, it must be prone also to be treated by one of the principal industrial processes: welding. The medium content of carbon and high amount of silicon and the high hardenability makes this steel apparently difficult to be welded. This is due to formation of brittle compounds such as carbides or oxides, and to the deterioration of the bainitic-austenitic microstructure, in the zone which undergoes high and uncontrolled temperatures. The deterioration processes of the structure in the weld bead and in the heat affected zone make the material weaker in these areas where the failure under mechanical load will occur.

1.2 Microstructure evolution

The presence of different alloying elements in the chemical composition of this kind of steel makes it very sensible to heat treatments. In particular, a middle or high content of carbon and high content of manganese reduces the temperatures of starting martensite transformation Ms and bainite one Bs). This enhances the stability of retained austenite and allows to obtain a finer bainitic microstructure due to lower temperature of isothermal heat treatment. Anyway, from the technological point of view, the most important effect of C and Mn is the shifting of CCT curves (perlitic and bainitic ones) on higher time values. This means a very high hardenability of the metal. Because of, after having been worked at high temperature and cooled in air at room temperature, the metal shows a prevailing martensitic microstructure, it could be stated that it is a "self-hardening" steel (see *Chapter 3.2*).

This is not always an advantage, for example in the case of welding process when the metal in localize zones reaches very high temperatures and its cooling path is not under control, decomposition of the microstructure and consequently deterioration of mechanical properties could be verified.

The main problem is the thermal stability of the retained austenite: due to reaching of high temperatures, for example in the joint zone, the austenite completely or partially decomposes and most of mechanical properties of the material such as ductility, strength and work hardenability capacity are lost.

Different decomposition mechanisms could characterize the austenite and the bainitic ferrite structure. In the case of austenite there is a strong difference in decomposition between film-like and blocky austenite. The blocky austenite grains before starting the degradation can be depleted by carbon due to the precipitation of carbides. Instead, the decomposition of film-like austenite is identified by the formation of an alternated structure of ferrite and cementite (red dots in *Figure 1*). The bainitic trip steels are susceptible to this deterioration processes for temperature above 450-500°C [6].

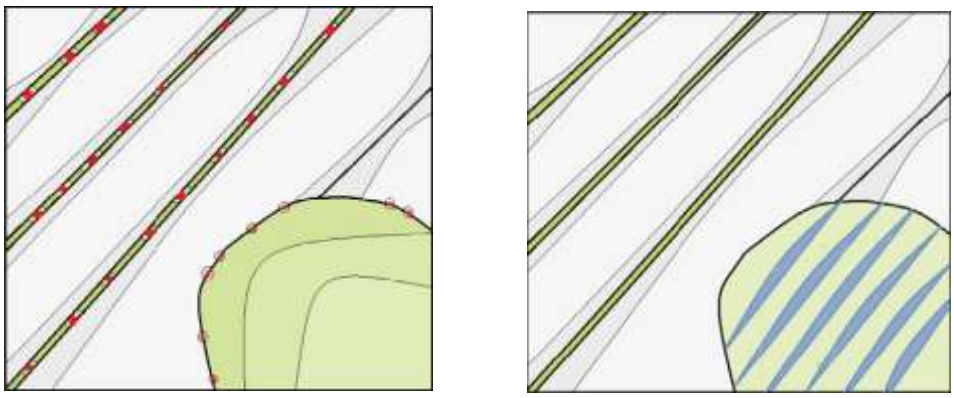

Figure 1 Possible decomposition mechanisms of film-like and blocky austenite [6]

If the blocky austenite grains have very low quantity of carbon due to the depletion for reaching high temperatures, these could undergo the transformation into martensite caused by a cooling stage to low temperatures. It must be specified that this would happen because of the low quantity of carbon into the austenite grains, these are unstable and prone to transform into martensite even with a low cooling rate like in air at room temperature (blue needles in *Figure 1*) [6].

If very high temperatures are reached and maintained for a certain time, the blocky retained austenite would transform into stable perlite, instead the film-like austenite will maintain its alternated structure of cementite nodules and ferrites because there isn't enough space to form perlite (alternated red and white stripes in *Figure 2*) [6]. Moreover, in situation of very high temperatures reached it could be verified the precipitation of carbides in the bainitic ferrite laths. These could be initially metastable carbides like Ɛ-carbide $Fe_{2,4}C$ which are further substitute by cementite Fe_3C (small red needles in *Figure 2*). If this transition is verified in the decomposition process, the presence of silicon retards the switch from metastable Ɛ-carbide to stable cementite [4] [6].

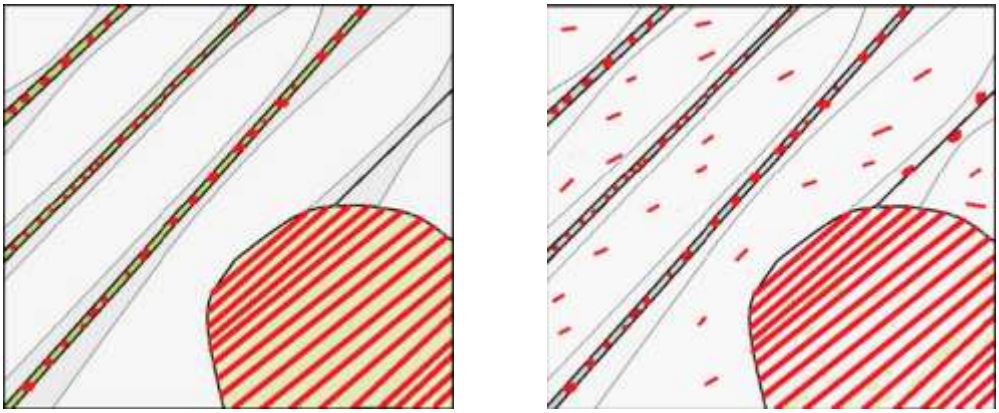

Figure 2 Formation of perlite and cementite in decomposition of bainitic ferrite and austenite structure [6]

These general decomposition stages of the TRIP steel microstructure can be divided in two different kind of deterioration processes: the direct decomposition and the indirect decomposition [6]. The indirect decomposition is the one that is correlated to the fast-cooling stage after tempering. In the first stage (*Figure 3*) there is no notable changes of the microstructure a part for the starting of precipitation of carbides in the bainitic ferrite laths. These, because precipitates in a metastable range of temperatures, could be Ɛ-carbides $Fe_{2,4}C$ [6]. In this first stage there is no markable changes also in the hardness of the material. In the second stage (*Figure 3*) due to a strong depletion of carbon from the blocky austenitic grains because of the carbides' generation, after the reduction of the temperature in the cooling stage, there is the generation of brittle martensite that forms in the carbon depleted austenitic grains. This phenomenon causes an increase in the hardness of the metal. In the third stage (*Figure 3*) there is a continuous depletion of carbon from the blocky retained austenite, more and more grains start to be unstable and decomposes into martensite at room temperature [6].

Moreover, in this stage there is the degradation of film-like austenite into alternated cementite and ferrite structure [6]. With this the highest value of hardness is reached, this is due also to the precipitation of brittle carbides at the austenitic-bainitic grains interface [6]. The fourth stage is the one where higher temperature are reached and the structure that is obtained is the one corresponding to the thermodynamical equilibrium, so composed by perlite and ferrite with nodular carbides that comes from the decomposition of the film-like austenite. This brings a reduction in the hardness of the material [6].

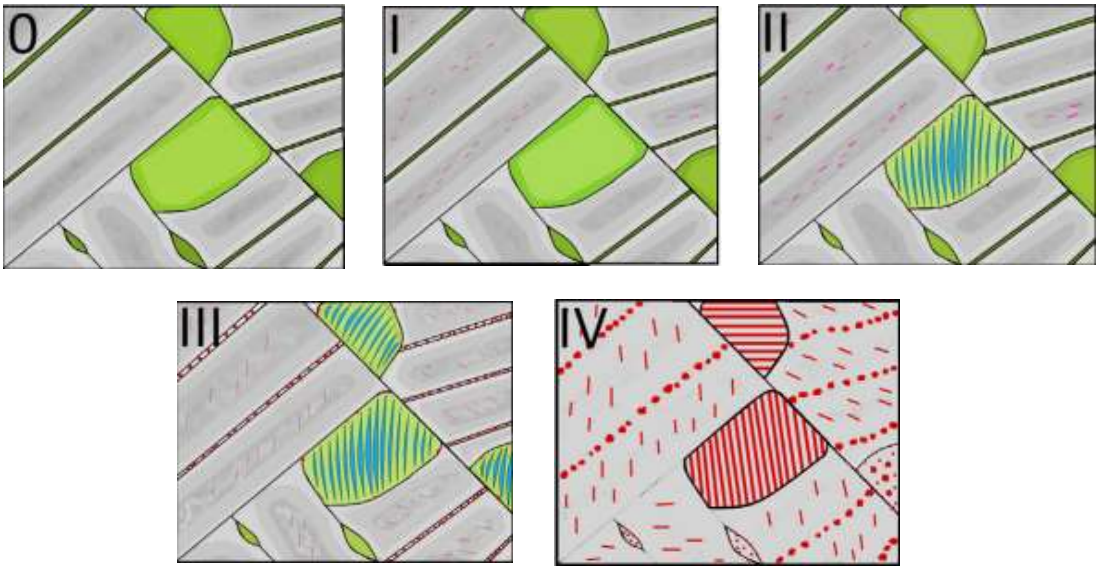

Figure 3 Indirect decomposition stages (heat and cooling treatment) [6]

The direct decomposition process is due to a continuous heating of the steel. In the second stage of this process, it can be noted that there isn't the formation of martensite due to the fact that the material is maintained at high temperature above Ms. In *Figure 4* due to the high temperature which the material is maintained (above 400-500°C) there is a strong depletion of carbon from the blocky austenitic grains, with the precipitation of brittle carbides with an acicular shape [6]. In the third stage of the direct decomposition, the main degradation that happens is the one of film-like austenite: this turns into an alternated structure of cementite and ferrite and causes a strong reduction in the hardness of the material [6]. This degradation mechanism is the one that brings the reduction of mechanical properties as hardness and tensile strength of the material. Moreover, in *Figure 4* is clear the depletion of carbon content from the austenitic grains (they become brighter in the picture) during holding time at high temperatures.

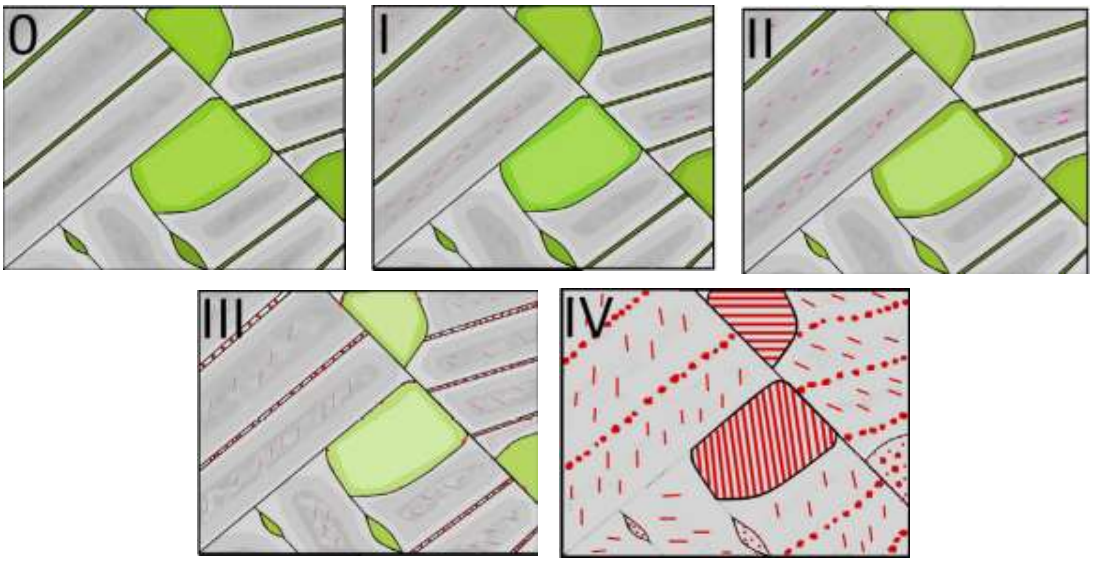

Figure 4, Direct decomposition stages (continuous heating) [6]

In *Figure 5* it could be seen the difference in the hardness evolution between the two types of decomposition processes. It must be noted that the direct decomposition, due to the degradation of film-like austenite in cementite and ferrite structure, causes a strong reduction in the hardness of the material. Instead in the indirect decomposition, the formation of martensite enhances the hardness of the metal, but with an increase also in the brittleness and cold cracking sensibility of the material [6].

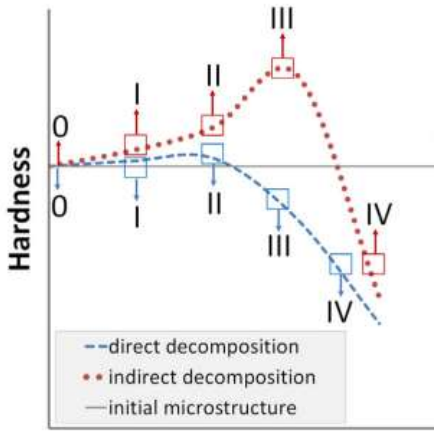

Figure 5, Hardness development in the two types of decomposition processes [8]

1.3 Cold cracking

One of the principal issues that could verify after welding processes is the generation of cold cracking phenomena. Generally, this process causes a reduction in the mechanical properties of the weld bead and the base metal, in particular it lowers the load-bearing ability and the energy adsorption capacity of the welded materials [7]. Avoiding cold cracking after welding procedure is a question of primary importance to preserve structure integrity. Cold cracking phenomena is also known as hydrogen embrittlement of the steel, this because the atomic hydrogen is the principal reason of cracks' initiation on the weld bead or on heat affected zone at room temperature (thermally altered zone due to welding process, see Chapter 2.4). The occurrence of this process must be adequately traced, this because the cracks could propagate also after some days from the production of the welded joint, with a catastrophic effect on the mechanical stability of the welded metals [8].

Usually, cold cracking will verify if three conditions are respected: a sufficient hydrogen pressure in the atmosphere or content in the metal, an enough sensitive material with a certain microstructure composition, a sufficient level of external or residual stresses applied [8]. The cold cracking phenomena is based on the diffusion of atomic hydrogen H^+ into the weld bead or in the heat affected zone during the welding process. Initially, the hydrogen is in the molecular form, which could come from a moist environment, or could be already present into the metal composition or in the filler metal wire/electrode. Successively, to diffuse into the metal or be adsorbed by the surface, it turns into atomic hydrogen and often occupy the interstitial sites of the steel atomic matrix [7]. The atomic hydrogen will diffuse into the metal structure and accumulate in the microstructure sites, this causes an increase in the hydrogen pressure that takes to the initiation of cracks. The two most important aspects from a thermodynamical and kinetic point of view are the diffusivity and the solubility of the hydrogen in the steel matrix. The lower is the diffusivity of hydrogen in the metal and the higher is its resistance to cold cracking, this is because the kinetic transport stage of H^+ into the metal would result as the limiting phase of the process. The higher is the solubility of the hydrogen in the metal and the lower will be the pressure generated in the accumulation sites, resulting in a lower probability of generation and propagation of cracks. Generally, the solubility of H^+ is higher in austenite in comparison with α-ferrite. For this reason, the utilization of austenitic stainless steels as filler metals in welding processes lead to strong reduction in the probability of obtaining cracks at room temperature [7].

In the most experimental analysed cases of high strength steel, the hydrogen embrittlement cracks have been found more often in the heat affected zone rather than in the weld bead [8]. This because the cracks are more prone to be initiated where a brittle structure is present, such as a martensitic one obtained with rapid colling after the welding process [8]. As in the microstructure evolution

description is explained (Chapter 1.2), if the TRIP steel undergoes rapid cooling after reaching high temperatures, the blocky retained austenite grains will immediately turn into brittle martensite. This would satisfy the second condition previously stated for the generation of cold cracking phenomena. Moreover, the displacive transformation of martensite will cause an increase in the residual stresses present on the metal surface, which will lead to a more favourable condition for the generation of microcracks and their further expansion.

Another factor that influences the sensitivity of the metal to the hydrogen embrittlement is the carbon equivalent: a parameter which is dependent on the chemical composition of the steel and in particular on the content of carbon (see Chapter 2.1). The higher is the value of carbon equivalent and the higher is the probability of generation of brittle phases, such as martensite, and so the more prone will be the material to undergoes cold cracking.

The possibility to act on the residual stresses condition of the metal is limited. For reducing the stress state of the steel, the right welding parameters must be chosen. The more important one is the pre-heating: increasing it will lead to a reducing in the cooling rate of the metal, and so a lower probability of generation of brittle phases will be achieved. Another option are the post welding heat-treatments of the specimen in order to reduce the residual stresses, such as annealing, and obtain a stronger condition of the welded metal.

1.4 Hot cracking

The hot cracking phenomenon consists in the differential solidification rate of the various phases which are in contact between each other, that cause the presence of lack of liquid in certain zones, and so generate tensile stresses that could take to formation of cracks. In carbide-free bainitic steels this issue could be present, it is a phenomenon governed by metallurgical and thermodynamical laws. In fact, the presence of various solute elements in high quantity can bring to segregation of these during solidification where its path doesn't follow the equilibrium one. These lead to the formation of small eutectics in the form of continuous intergranular or interdendritic films during the final stage of the solidification. There are many factors which influence the hot cracking phenomena like solidification temperature range, primary solidification, solute redistribution, solidification grain structure and others [9].

In the welding process HAZ heat affected zone, where high temperatures are reached by the material, undesirable transformations could happen. Because TRIP steels are rich of alloying elements that can segregate at grain boundaries, these low melting compounds (like sulphates, phosphorates) during heating up can produce liquid phase, which in the successive solidification stage results not homogeneous and so cause tensile stresses on the material [9].

The cracks forming are always intergranular or interdendritic, so following the path of grain boundaries or dendritic boundaries, that is caused by the generation of segregates and from these zones the cracking phenomena will start.

The generation of hot cracking behavior from the solidifying material is strongly dependent on the chemical composition of the alloy, in fact in function of the quantity and kind of solutes (alloying elements) the solidification process is controlled. For example, if an austenitic stainless steel is used for the welding procedure, it must contain very low quantity of S sulfur and phosphorous P because these have a very low solubility in austenite structure (compare to the one in ferrite which is higher), so during solidification they will highly segregate and produce low melting eutectoids that cause the formation of further differential shrinkage on the grain boundaries. Instead, other alloying elements like Ni and C have higher solubility in austenite so in these cases the solidification as austenitic structure is more convenient and less sensible to hot cracking [9].

Essentially, the chromium equivalent (ferrite stabilizers) and nickel equivalent (austenite stabilizers) determine the mode of solidification of a steel: this can be in ferrite mode or in austenite mode, so if the stabilized phase at room temperature will be α-ferrite or austenite. The ferrite mode is generally the preferred one because of the less tendency to segregation of alloying elements (like S and P) instead of the austenite mode and so less probability of hot cracking, there are anyway some exceptions. So, to enhance the ferrite mode solidification, in other words the stabilization of ferrite at

ambient temperature, more elements like aluminum must be added and elements like nickel or carbon must be reduced in order to achieve high hot-cracking resistance [9]. In carbide-free bainitic steels a certain quantity of carbon must be always present, the principal reasons are: the lower the quantity of carbon and the higher will be the Ms temperature, so the higher will be the sensibility of the metal to form martensite in the HAZ. Another reason is that as the carbon content decreases the temperature at which the bainitic transformation occurs will increase, this will result in a coarser final microstructure with bainite laths that are larger and so the material results weaker. Moreover, the quantity of carbon directly influences the strength of the bainite structure [9].

The presence of Mn is important for its effect on sulfur and on eliminating it forming MnS which can be easily removed from the metal, is also an element which improves the stabilization of austenite at room temperature and reduce the temperature of Ms. Anyway, a too high content of manganese could take to higher susceptibility to hot cracking phenomena of the material.

Silicon is the more dangerous alloying element for the hot cracking tendency, it is the one that have the higher tendency to segregate even at low quantity into the metal. In fact, over 0.65% wt. will cause problems in the hot cracking formation [9].

In general, for the development of a hot crack in the metal there must be a zone in the solidifying material which is a susceptible microstructure to this and must undergoes enough tensile strain for the propagation of the crack. Moreover, the generation and propagation of a hot crack happens in the as named “brittleness temperature range”, so an interval of temperatures which the liquid during solidification is isolated and no more feed of other liquid phase and so it differential solidifies and cause crack formation. In this range the material toughness is zero and so it will show cracking phenomena. This temperature range stands between the NST nil-strength temperature, so the temperature on heating at which the material strength is near zero, and the DRT ductility recovered temperature, the highest temperature below NST at which the material recovers a minimum ductile behavior [9]. Of course, during welding process the metal reaches the NST (at about 1300°C) and so with segregation of alloying elements and formation of isolated unfilled liquid zones, till it doesn’t return to the DRT it would undergo to hot cracking. When it passes the DRT the liquid areas will solidify and the steel recovers its toughness. Generally, for CFB metals this temperature range is quite narrow, more or less 50°C (higher is this temperature range and higher is the tendency of the steel to generate cracking), but this can be modified by the presence of certain alloy elements [9].

2. Welding processes

2.1 Weldability of steels

The “weldability” of a metal is defined as the attitude of the material to generate joints after the localized melting of the interested junction area. The two metals that are joined together could be the same, in this case the welding process is called “autogenic”, or could be two dissimilar steels, in this case the process is called “atherogenic”.

The target of this is to obtain a joint that is stable and durable, which maintains its chemical and physical properties during time in exercise, that ensure safeness in its use. Fundamentally a weld joint must have a good mechanical resistance equal or higher of the two surrounding metals which are joined. It must show a ductile behavior and not brittle, it must be clean from impurities (oxides, nitrides, sulfides) and defects. The weld bead must have very low sensibility to hot-cracking and cold-cracking phenomena.

The capacity of the steel to maintain its mechanical properties like hardness, strength and ductility in the thermally altered zone are strict correlated to its chemical composition, hardenability and cooling rate of the zone after the welding process.

2.2 MIG welding process and parameters

MIG stands for Metal Inert Gas welding process and is a subcategory of GMAW Gas Metal Arc Welding; it could be automatic or semi-automatic procedure.

It works with the generation of an electric arc between the based metal and the wire of filler metal that melts the two and made them to join. This is done in an inert gas atmosphere which is created by a pump directly on the arc area, and it allows to have the two metals that are joining together to be shielded from the environment avoiding the deposition of impurities or oxidation of the surface. Moreover, this gas is fundamental to generate a good and stable electric arc.

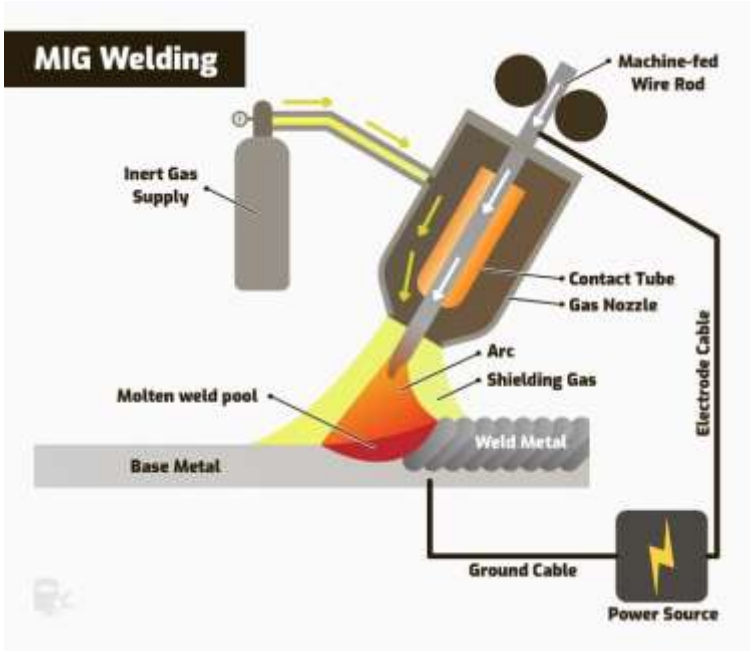

Figure 6 Representation of MIG welding process components [3]

The principal parameters that are controlled in this welding process are: welding current, arc voltage, welding speed, heat input, pre-heating, material of the filler metal, electrode size, gas flow rate, shielding gas composition, welding position.

The influence of the current in the MIG process is basically on the depth of the weld bead: higher is the current and higher is the dept obtained at the end of the process. The current is proportional and strictly correlated to the thickness of the material, it is also correlated to the welding speed [10]. The lower is the welding speed and the lower is the current, this is because if a too much high value of current with a low welding speed is used, the risk of obtaining the burn-through of the base metal is high, and of course this isn't desired [10]. On the other hand, with a lower value of current in comparison with a high value of welding speed a lower dept of the bead with very low resistance of the joint is obtained.

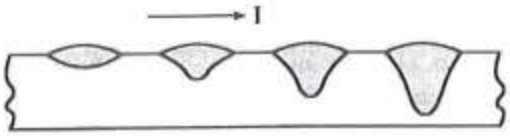

Figure 7 Infleunce of the current on weld bead dept

Another parameter that influences the dept of the weld bead is the distance between the tip of the electrode and the based metal: higher is this distance and lower is the penetration. For a short arc welding process is considered a tip distance of about 3-5 mm, for a spray arc is considered a distance of about 10-20 mm between the torch and the based metal. The control of this parameter is also important: normally as the current and/or the voltage increases, also the tip-to-work distance will increase to maintain a good dept and width of the weld bead [10].

The welding voltage doesn't affect too much the penetration, in some experiments it could be seen that the penetration doesn't change even if the voltage is decreased or increased. The welding voltage got the principal effect on the width of the weld bead: the higher is the welding voltage and the wider will be the bead [10]. It must be noted that there is a difference between the voltage of the arc and the voltage set on the welding machine. The voltage of the arc is the potential difference between the tip of the electrode and the material which forms the arc, this has a difference with the one displayed on the machine with values that can go from 1.5 to 2.5 volts higher in function of the size and length of the wire [10].

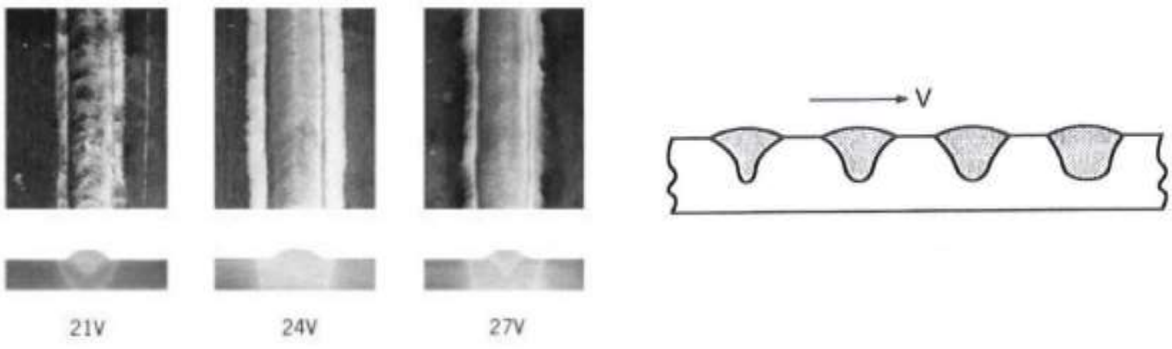

Figure 8 Effect of welding voltage on width of weld bead [10]

The effect of the welding speed on the bead is similar to the one of the arc voltage with more influence on the dept of the weld bead [10]. In particular, for values of low welding speed the weld bead obtained is of course wider and deeper than the one with a higher speed. The limit case of this is that if the speed is too low the deposited material accumulates on the front of the electrode path and don't permit the deposition of other [10].

The opposite case verifies if the welding speed is too high, at the limit of this situation the material which is deposited from the filler metal electrode doesn't have the time to melt the based material, this causes a very weak bead with a low quality of the interaction between the weld bead and the based metal [10]. This in any case is not even always verified: the value of welding speed, arc voltage and current are correlated and for a good welding result the right combination of these three must be reached.

Another parameter that is correlated with the welding speed is the deposition rate: this indicates the quantity of metal that is deposited in one hour of welding.

$$v_d = \frac{v_w}{m\ of\ wire\ in\ one\ kg\ of\ metal}\ [\frac{kg}{h}]$$

Equation 2 Definition of deposition rate [10]

Of course, in function of the density of the filler metal and the diameter of the wire which compose, the value on the denominator of this equation is determined differently.

The deposition rate (and so welding speed) can be used together with the distance tip-to-work: a low value of the welding speed with a higher value of the distance between the tip of the electrode and the based metal permit to have a lower value of the current with a controlled penetration of the weld bead and a higher stability of the arc [10].

In general, the three parameters that control the weld bead quality and shape are the welding current, voltage and speed. These three are all grouped in the heat input Q [kJ/cm] which is direct proportional to current and voltage and inversely proportional to welding speed.

$$Q = \frac{I*V}{v_w}$$

Equation 3 Welding heat input definition

A higher value of the heat input in general means that higher temperatures are reached in a lower time by the weld bead and based metal, the heat input value is also correlated to the characteristic cooling rate of the weld bead which is lower as the heat input is higher [11]. This means that these two are correlated with the following relations:

$$T_p \propto \frac{Q}{r^n} \qquad \Delta t \propto Q^n$$

Equation 4 and 5 Relations between peak temperature and cooling rate with heat input [11]

Where T_p is the peak temperature reached in a certain "r" distance of a point considered from the weld bead, "n" is a parameter that varies from 1 to 2 and it depends on the thickness of the material and the one of the workpiece.

Another important factor that must be considered in MIG welding is the filler metal, so the material that is used for the consumable electrode and is deposited on the based metal to make the joint [10]. The principal characteristics that must distinguish a good filler metal are the fact that it must not be sensible to hydrogen embrittlement, this depends on the diffusivity of hydrogen that must be low and solubility of that must be high in the filler metal crystalline structure [10]. This prevents the formation of cold cracking phenomena and the obtaining of a strong weld bead. The filler metal doesn't have to cause porosity when it's deposed on the based material. It must not generate dangerous compounds when it comes in contact with the base metal at such high temperature, as dangerous compounds are intended ones that cause embrittlement of the structure (oxides, nitrides, sulphates) [10].

There are five principal factors that influence the choice of the filler metal for the wire: the chemical composition of the base metal, the mechanical properties of the base metal, the shielding gas employed, the type of service or specifical requirements, the joint design [10].

The most important phenomena to avoid during welding is the oxidation of the weld bead when the filler material is deposited, and moreover the oxidation of the base metal near the weld bead. This is because it could take to the formation of oxides which are very hard but also very brittle, also the formation of porosity could come from the oxidation of the material near the weld bead. To avoid this many elements are employed in the filler metal composition to be oxidized during the process (even if the oxygen partial pressure is low due to the action of the inert gas), they form oxides that generate a glassy slag that deposits on the surface of the weld bead [10].

The most used elements for this task are silicon Si, it is used at percentage about 0,4-1% and it gives high deoxidizing service, the higher the quantity of silicon and higher is also the strength of the weld bead with a little reduction of the toughness, anyway if it goes above 1,2% it could cause cold cracking [10]. Another element used for deoxidation is manganese Mn, this is used in quantity from 1-2% and it increase the strength of the weld metal more than silicon, moreover it reduces the hot-cracking sensitivity of the metal [10]. Also aluminum Al, titanium Ti and zirconium Zr are very strong deoxidizer and can be employed in very little quantity like 0.2%. There is also carbon C which is used as deoxidizer, it is used in percentage from 0.05 to 0.12%, one problem is that if there is more than 0.12% it could form CO that when it's removed from the weld bead or the base metal it will leave porosity. Another problem of carbon is that the higher its value and the lower is the weldability of the material for the generation of carbides that make the structure brittle and weak with formation of cold cracking phenomena [10].

Together with the filler metal, the type of shielding gas determines the chemical composition of the weld bead. Three main gases are used to protect the steel from the external environment during welding process: argon, helium and carbon dioxide [10]. Moreover, the adding of small quantities of

nitrogen, oxygen and hydrogen in some situation is stated as advantageous. Argon is an inert gas; this means that it doesn't react with other elements to form compounds on the welded metal. These gases can be used in combination between each other in order to obtain the ideal welding atmosphere that surrounds the electrode.

One important property of the gas is its thermal conductivity: the higher is that and the higher will be the value of the arc voltage to maintain it stable [10]. For example, He and CO2 got a higher thermal conductivity than Ar, this means that with this last one a lower voltage could be used and the arc will remain in any case stable.

With the welding process of mild steels, the utilization of gas composed by Ar with a little percentage of O2 or CO2 are widely diffuse: this is because the presence of these elements maintains the arc stability and promote the melting between the tip of the electrode and the base metal [10]. Anyway, the filler metal electrode must be composed by strong deoxidizing elements (Si, Mn) that avoid the formation of oxides on the weld bead without generation of porosities on the metal. The employment of pure CO2 as shielding gas in MIG processes is not advisable: it is not an inert gas; this is because when the current goes through and heat the gas it breaks the bonds between oxygen and carbon and form active compounds that could react with the metal surface. The advantage of using carbon dioxide is that with this it can be used a fast-welding speed and deep penetration. On the other hand, for the reasons that are previously presented, the surface of a metal which is welded under atmosphere of CO2 is always oxidized [10]. So, its utilization is more common for mild steel in combination with Ar where the metal wire must have the presence of deoxidizing agents.

The two principal mixtures that could be used in MIG process are the Ar+O2 and Ar+CO2. The combination of argon and some percentage of oxygen is widely used: this ensures a high stability of the arc, it improves the wetting of the surface and the weld bead shape. It lets the metal to be fluid for longer time so it can flow on the weld bead toe and fulfill the whole cavity formed by the two metals that are joined together. Typical mixtures used for medium carbon steel are Ar with 2-5% of O2 [10]. The shielding gas composed by argon and low quantity of carbon dioxide CO2 produce more or less the same effects on arc stabilization as the mixture of argon and oxygen. The principal difference between the two is the fact that with CO2 a higher spray current transition is obtained, this means that higher value of current could be reached during the welding process for maintain the arc stable, which ensures high penetration of the weld bead in combination with high welding speed. Oxygen causes the reducing of the spray transition current [10]. The more used combination of these can be Ar with 10-25% of CO2.

2.3 MMA welding process and parameters

The Manual Metal Arc, also known as Shielded Metal Arc Welding (SMAW), is a welding process that is widely employed nowadays for the junction of a large variety of metallic materials. In this welding procedure, instead of MIG or TIG processes, there isn't the utilization of a shielding gas to protect the material from the atmosphere. This is an advantage for the fact that it could be done outdoors, where the other two processes cannot be taken. For this reason, this process is often employed for building of external structures. The weld bead is generated thanks to a consumable metallic electrode, which is coated with a layer of chemical and metal compounds (iron powders and others). An alternate or direct current pass through the coated electrode and generates an arc with the base metal, the molten electrode metal and flux is transferred across the arc to the base metal and generates the weld bead. During the striking of the arc both the core of the electrode and the coating are melted, with the contribution also of this last one to the composition of the weld bead. One of the principals aims of the electrode coating is the generation of shielding vapors and protective slag on the weld bead, this must be anyway removed from the final resulted joint [12].

The equipment which is needed for the welding process is essentially formed by an electrical generator, electrical wires, consumable coated metallic electrode, base metal to be welded.

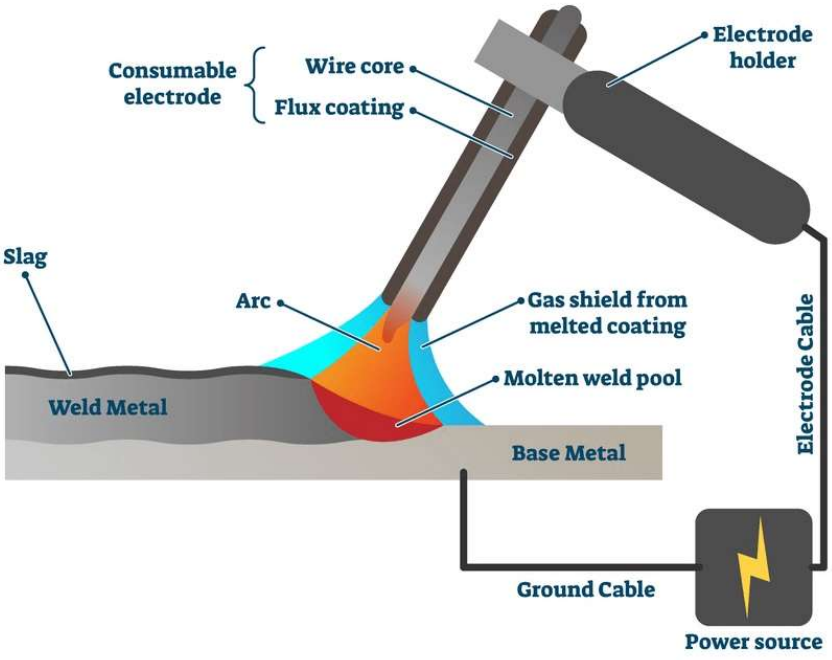

Figure 9 Representation of SMAW welding process components

The principle that stays behind the generation of the weld bead thanks to the electric arc could be explained through the "Electron Theory Arc Column" [13]. This theory explains the behavior of the particles that are interested in the formation of the arc and how the heat is generated and distributed. Essentially, when the current is applied to the circuit there is the accumulation of electrons at the negative pole, or the cathode. These electrons are immediately attracted by the positive pole, or the anode, and so being accelerated with a very high velocity and striking against that. The path that these electrons follow is in the interior of the arc column, this gives a certain contribution to the total heat developed by the arc [13]. The other heat contribution is given by the kinetic energy that is stored in these particles: when they strike the anode their energy is transformed into a great amount of heat. Consequently, the positive charges that are present at the anode are attracted by the negative side, in their returning to the cathode they produce an ionized gas layer that protects the electrons and the electrostatic unit within them. So, three principal areas could be recognized: the anode area, the plasma area and the cathode area. The great amount of the heat is concentrated on the anode area, due to the kinetic impact of the electrons on its surface. The plasma area is heated from the collision between the electrons and the ions that pass through the ionized gas, in this the lower amount of heat is produced. The cathode area is the medium heated one due to the ionic bombardment [13].
This happens when DC current is applied, by changing the polarization of the electrode and the base metal also the distribution of the heat is varied. This results in a different penetration or wideness of the weld bead at the end of the process, because 2/3 of the heat is distributed at the positive pole and the remaining 1/3 is located at the negative one. The Direct Straight Polarity Current is obtained by setting the electrode as negative pole (DCEN) and the base metal as the positive one. So, with this the 70% of the heat is localized at the base metal, obtaining a deeper penetration of the weld bead and a low consumption of the electrode. The Direct Reverse Polarity Current is stated when the electrode is the anode (DCEP) and the base metal is the cathode. In this case, the most amount of the heat is localized at the electrode tip. For this reason, thicker electrode must be employed in order to control its consumption during the welding process. The lower heat distributed on the base metal causes a wider and less deep weld bead, with a lower cooling time of the base metal.

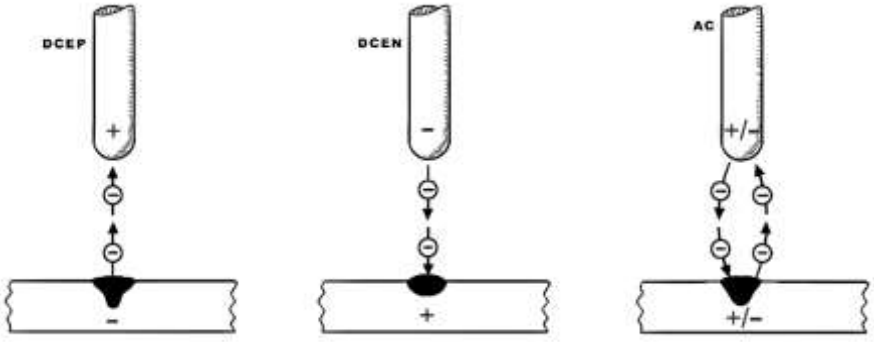

Figure 10 Scheme of different current types in MMA welding process [24]

If alternate (AC) current pass through the circuit, the interchange of electrons is equal between anode and cathode, with a uniform heat distribution between the two and the plasma area becomes the medium heated one [13]. A disadvantage of SMAW that is correlated to the current amplitude is that since the electrode is consumable and so reduces its length during the welding process, the heating resistance of the filler rod vary during time. For this reason, an adequate controlled value of current must be chosen to avoid the overheating and premature melting of the flux coating [13].

The consumable electrode composition is an important aspect that must be choose adequately, in function of the materials that will be welded together and the other process parameters. The coating that could be find in every kind of electrodes gives specific benefits to the weld bead. The general composition of the electrode coating is made by powdered cellulose mixed with carbonates, oxides and other elements that are held together by a silicate binder [13]. It gives protection to the weld pool from the external atmosphere, in particular from dangerous gases such as oxygen and nitrogen. It works in this case as the shielding gas in the other welding processes, with the production of, for example, normal carbon dioxide gas from the decomposition of coating elements [13], avoiding the reaction of the melting materials with the atmosphere without the generation of dangerous chemical compounds. Moreover, if during the welding process there is the generation of impurities on the weld bead surface, the fluxes that are deposited from the coating of the electrode make them to float to the top and be immediately removed as glassy slag after the weld metal is obtained [13]. However, the presence of the flux coating increases the probability of slag imprisonment and generation of slag inclusions. These ones are principally caused by cavities and crevices which entraps the slag particles that are more difficult to be removed in the successive brushing operation, so the particles turn into inclusions. To reduce this phenomenon a thinner electrode could be used if the weld joint is restricted [12]. Another important function of the coating is the improvement of the stability of the arc, without the coating the arc would be difficult to control and would produce large quantity of metal sputter that decrease the final weld bead quality. The coating of the consumable electrode also works as a source of alloying elements and anti-oxidizing compounds, which are transferred to the weld pool during the process. Another important purpose of electrode coating is the improvement of the penetration, this allows to use less current and maintain the arc more stable during the welding process [12].

One of the main disadvantages of the MMA welding process is the removing of the slag layer that is formed on the metallic weld bead surface, this must be done at every welding passes. This reduces the efficiency of the process and the control of the interpass temperature. Another drawback is the need of electrode backing and storing procedures, in order to reduce the moisture present on the coating and so avoiding the possibility of hydrogen embrittlement of the welded steel.

The efficiency of the electrode is defined as the percentage of the weight of all weld metal from the electrode in proportion to the weight of the core wire. A normal value of efficiency for a consumable electrode is 120-130%, in the case of high-efficient electrodes it could be up to 180-250% [12].
The consumable electrodes are classified in function of the coating chemical composition. These are divided principally in three groups: acid, rutile and basic electrodes [12]. The acid electrodes are composed by a coating with high presence of manganese and iron oxides. The presence of manganese gives high deoxidizing capacity, the iron oxides increase the efficiency of the consumable electrode. The principal advantages are the production of a smooth welded surface, with a porous slag that is easy to remove. The drawback is that a lower yield strength and ultimate tensile strength are obtained, in comparison with the other kind of electrodes. This electrode composition is often employed for welding of low alloyed and low carbon steels [12].
The rutile electrode coating is composed by a high content (up to 25-45%) of titanium bi-oxide, TiO_2. With this kind of electrode, a very stable arc is generated, with the obtaining of a high striking power. The final weld bead got good mechanical properties such as high fatigue strength. The principal disadvantage of this is the generation of hydrogen in the weld bead, so a higher probability of hydrogen embrittlement of the material is obtained with formation of cold cracks.
The other kind of electrode coating composition is the basic one. This contains calcium fluoride, CaF_2. The slag that is generated during the welding process reacts as a base, which lead to a very low sulfur and oxygen content into the weld bead. For this reason, a higher tensile strength and toughness of the weld metal is obtained with this kind of electrode in comparison with the others. The production of this kind of electrode is taken at very high temperatures (up to 500°C), this led to a low moisture content into that. For this reason, the hydrogen content into basic electrodes is very low, which takes to a lower probability of generation of cold cracking phenomena on the weld bead. The principal drawbacks of the basic electrode are the less stable arc, the low striking power of the arc, the slag layer formed on the weld metal is not so easy to be removed as the other electrodes composition [12].
The metallic core composition of the consumable electrode must be chosen adequately in order to be compatible with the chemical composition of the base metal. The electrode size must be chosen in function of the electrode type, the base metal thickness and the welding current.
Another important parameter to control is the arc length: if the arc is too long it will result in a wide and irregular weld bead, with the presence of sputter and porosity, resulting in a bad quality of the joined area. If the arc is too short the energy transferred to the base metal wouldn’t be enough to melt it, this result in the electrode that would be sticked to the workpiece surface [13].

In most of the Manual Metal Arc welding processes that involves the junction of metal parts with a certain thickness (above 5-6 mm), a multiple number of passes is employed in order to obtain the full penetration of the base metal that is welded. If a great number of passes are made for welding the metals, another important welding parameter must be considered: the interpass temperature T_{ip}.

The T_{ip} is the temperature that characterize the weld bead between two successive passes, it could be detected with a thermocouple during the welding procedure. The control of the interpass temperature is important for many reasons: it influences the final mechanical properties of the welded metal, this because in function of the temperature at which the metal got welded it will have different microstructure that are determined by the cooling rate. This last factor is strongly controlled by the interpass temperature, in fact higher is this maintained and lower will be the cooling rate of the material. With the welding of bainitic steel, due to its marked self-hardenability, is important to have a controlled cooling stage, avoiding the generation of brittle phases at the end of solidification. The interpass temperature also influences the hydrogen embrittlement of the welded metal: if a certain temperature is maintained and controlled, the hydrogen has more time to diffuse away from the metal surface and so not get trapped for generate cold cracking.

Another important parameter that must be considered during welding processes is the pre-heating of the metal. This consists in the heating procedure of the whole part to a certain temperature before the welding procedure is take out. The utilization of pre-heating is fundamental for different reasons: it reduces the cooling rate of the welded steels, already explained with the interpass temperature, where the control of the metal microstructure solidification is important for avoiding the generation of brittle phases. Another motivation is to reduce distortions due to thermal stresses, which are present when the weld pool cools to the ambient temperature. The pre-heating of the part reduces the thermal difference between the weld bead and the surrounding material, so the thermal stresses and strains are also strongly decreased. Pre-heating benefits welding procedures also for reducing the hydrogen embrittlement of the metal. In fact, it helps to remove moisture from the metal surface and so reduce porosity caused by the diffusion of hydrogen into the weld bead. Moreover, if hydrogen is diffused into the weld surface, the lower cooling rate caused by the pre-heating allows more time to hydrogen for get removed from the metal, with a reducing in cold cracking phenomena [14].

2.4 TIG welding process and parameters

The Tungsten Inert Gas welding process, also known as Gas Tungsten Arc Welding (GTAW), is one of the most diffused welding procedures. This method could be used to weld practically all ferrous and non-ferrous alloys, with the possibility of welding also dissimilar metals such as carbon steels and stainless steels [15]. This process permits to obtain high quality weld beads, thanks to the high control of the heat supplied to the base metal. With this method there is also a low production of spatters and sparks during the welding of the metal, thanks to the pointed heat spot obtained during the welding procedure.

The TIG welding process is composed by a power source, made by a torch, connected to a non-consumable tungsten electrode. In addition, a consumable handled metal rod is used as filler material to obtain the desired weld bead. A current, supplied by an electrical generator, pass through the electrode and the base metal with the generation of an electric arc between the two. This permits to obtain the melting of the base metal and the filler material, with the generation of the weld bead. The welding spot, so the melted zone, the heat affected zone and the electrode tip, are shielded during all procedure by an inert atmosphere. This is given by the continues flow of an inert gas, usually He or Ar or a mixture of this two, supplied by a nozzle on the torch.

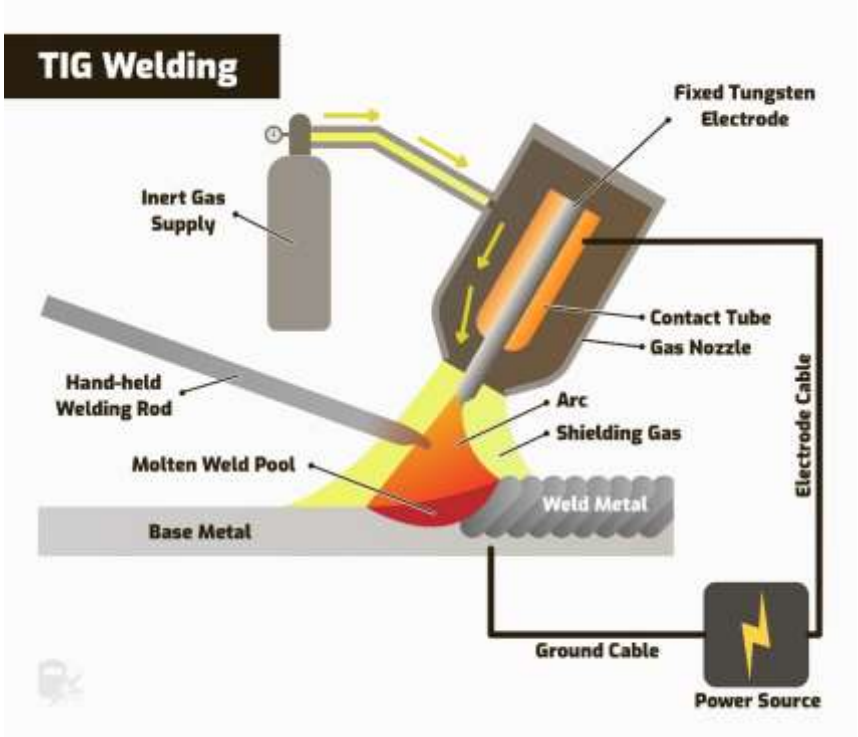

Figure 11 Representation of TIG welding process components

As in the MIG welding process, the utilization of an inert atmosphere is fundamental for avoid dangerous reactions that could occur at high temperatures when the metals are melting. These are principally the oxidation of the steel or the generation of dangerous chemical compounds, which reduce the metallurgical and mechanical properties of the weld bead. The composition of the shielded gas must be chosen adequately in function of the chemical composition of the metals that are welded together. Other important parameters related to the shielding gas are base metal thickness, gas nozzle diameter and the gas flow rate.

Another important parameter is the choice of the tungsten electrode composition and diameter. The tungsten W is a rare metallic element, which got the highest melting temperature in comparison to all other metals (3410 °C). There are lot of electrode types in terms of dimensions and composition. The most diffused ones are composed by pure tungsten or tungsten alloys with other rare elements oxides. The choice of the non-consumable electrode depends on the chemical composition of the metal that must be welded, on the dimension of the part, and on the process parameters that will be adopted (current and others). Some of possible tungsten electrode compositions for TIG-DC and AC are: pure tungsten (EWP), 2% cerium-tungsten (EWCe), 1% zirconium-tungsten (EWZr), 1 % thorium-tungsten (EWTh-1), 2% thorium-tungsten (EWTh-2), 2% lanthanum-tungsten [16] [15]. The pure tungsten electrode has the lowest purchase cost of all the kind of electrodes. It is often employed for alternate current welding of light alloys where it maintains a high stability of the arc. Is not advisable to use it for welding in direct current because it could take to breakdown of the tip and very low stability of the arc. Another issue of this electrode is that it could generate tungsten inclusions on the weld surface, so high probability of contamination of the bead. The cerium-tungsten electrode, composed by tungsten and cerium oxide, is a good solution if a direct current welding process is conducted. In fact, it would generate stable arc as the pure tungsten electrode when is under alternate current. This kind of electrode could be used in direct or alternate current procedure. The zirconium-tungsten electrode, composed by tungsten and zirconium oxide, is the most common for welding aluminum alloys with AC. Its principal advantage is the avoiding of tungsten inclusions generation. The thorium-tungsten electrode, with presence of 1,7-2,2% of thorium oxide, has a great ability for sustaining high values of direct current, for this it is often employed for manual TIG welding processes. In comparison with other electrodes, during welding procedure it deposits less tungsten compounds on the metal surface, resulting in a very low contamination by tungsten inclusions. One issue of this kind of electrode is that thorium is radioactive, so during the welding process the operator must be adequately protected [17]. The lanthanum-tungsten electrode, usually composed by 1,8-2,2% of lanthanum oxide, can be used with a wide variety of metals and process parameters. With this kind of electrode, a very stable arc is generated, with less spitting and low erosion rates [16].

The size of the electrode is chosen in function of the type and magnitude of the current that is employed in the welding process. The most common diameters that are used in industry are 1,6 mm for 30-100 A in DC current or 30-80 A in AC current, 2,4 mm for 60-180 A DC current or 60-150 A in AC current [18].

Once the ideal diameter of the tungsten electrode is chosen, an important stage that must be carry out is the shaping of the electrode tip. This procedure is conducted with the utilization of fine grit abrasive wheels before the welding procedure [15]. The shape of the electrode tip is determined principally by the magnitude of the current which is employed. Considering L as the length of the shaped electrode tip and D the diameter of the electrode, the ratio L/D must be reduced as the current value increases. This because a sharper tip permits to have a more precise pointed location of the arc on the base metal surface, on the other hand the smaller is the tip radius and the higher will be the sensibility to rupture when it undergoes to high temperatures due to high current values.

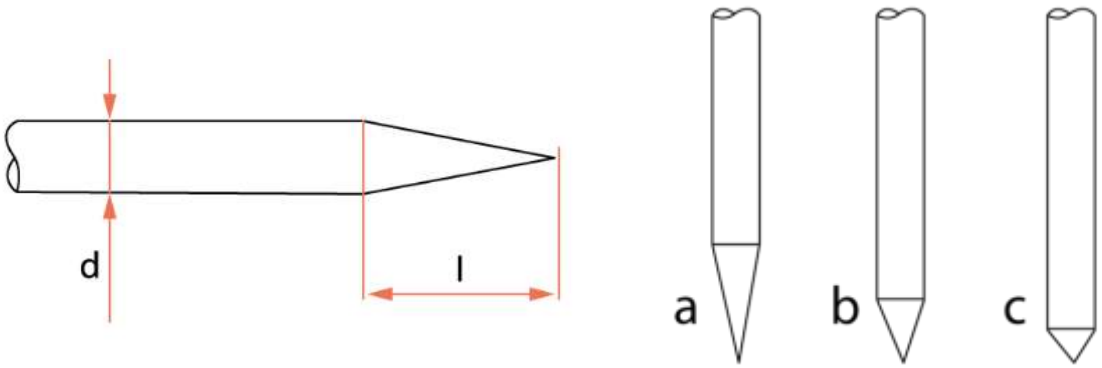

Figure 12 Shaping of the tungsten electrode tip in function of a) low current b) mid current c) high current applied [26]

With TIG welding process the principal advantage is to obtain a weld bead free from impurities, with high mechanical and physical properties. On the other hand, the main issue of GTAW is the lower penetration of the weld pool in comparison with, for example, MIG welding process (see Chapter 2.2). This, from an industrial point of view, is a disadvantage: for welding thicker parts (above 7-8 mm) a certain number of passes must be conducted. This is translated into a higher time spending and so higher costs for one welding operation.

Nowadays, several techniques are implemented to obtain a deeper penetration of the weld bead. These are for example Activated Flux TIG (ATIG), where a layer of flux based on different chemical compounds (metal oxides, chlorides…) covers the surface of the base metal and increase the final weld bead by two or three times [19]. Another method for increase weld penetration is the Pulsed Current TIG (PCTIG) process, where a pulsed current is employed instead of the continue one. A peak current and a lower base current are varied in time with a certain frequency. The effect is to have

the base current which maintains the arc burning and alternately the peak current melts with higher energy the base metal [19].

The control of welding process parameters allows to obtain the desired penetration on the welded material. The most influential parameters are the arc length, electrode condition, current polarity, welding speed, angle of the torch, shielding gas coverage [19]. The arc length is the distance between the base metal and the tip of the non-consumable tungsten electrode, higher is this and wider is the final weld bead. The current polarity could be DCSP or DCRP, by choosing the Direct Current Straight Polarity a deeper weld bead will be obtained due to the higher heat distribution on the base metal. The current amplitude also influences the height of the weld bead. The weld speed must be chosen adequately in function of the current amplitude (as in MIG welding), with high values of welding current and low values of welding speed the weld bead risks to burn-through.

The most widely used shielding gas for TIG welding processes is argon, this is due to its inert capacity and its low purchase cost. Anyway, mixtures of different gases are employed to compensate the argon low heat flux on the base metal. These are helium, as the most diffused, and sometimes hydrogen, nitrogen, carbon dioxide [20]. The features that distinguished He from Ar are the higher specific heat and lower electrical conductivity. These physical properties of the shielding gas greatly influence the welding arc: in the utilization of pure helium or mixtures of different gases lead to an increase in the maximum arc temperature and flow velocity of the arc [20], resulting in a higher penetration of the weld bead [15].

Other important factors are the chemical composition and physical properties of the filler metal rod, these must be chosen adequately to obtain a satisfactory mixture between the welded metals.

2.5 Welding microstructure alteration

The welding process causes a strong localized alteration of the macrostructure and the microstructure of the steel. In particular, due to the high temperatures that are reached thanks to the generation of the arc between the base material and the filler metal wire, there are several zones that could be distinguished, each of these is characterized by specific temperature ranges that are registered. The zone that undergoes to the highest temperatures is the fusion zone FZ, in this the filler metal and the based one are melted in order to further be joined together after the solidification. In this zone temperatures near or above 1000°C are reached. Successively to the FZ there is the high heat-affected zone HHAZ, temperatures between the fusion one and the phase-equilibrium curve Ac1 are reached. After the HHAZ there is the low heat-affected zone LHAZ, where there are temperatures below Ac1. The last zone is obviously the based material which is consider thermally unaltered from the welding process [21].

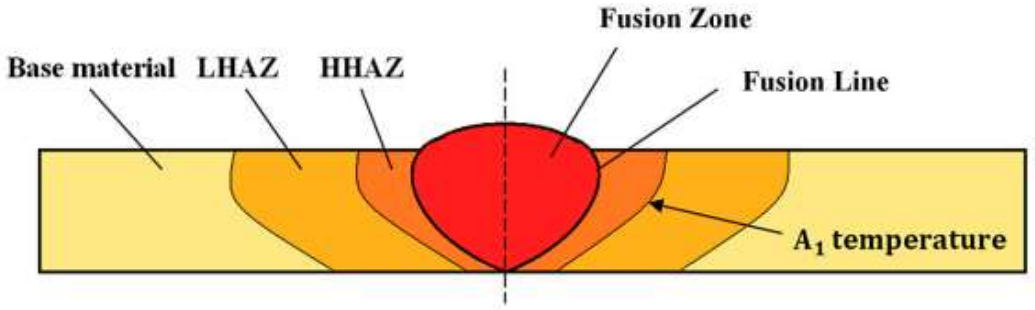

Figure 13 Welding heat altered zones [14]

Since in each zone different temperature ranges are reached, the corresponding different microstructure alteration in each of these could be evaluated.

In the LHAZ, going from the base material side to the weld, it could be detected the carbon depletion from the blocky grains of retained austenite, this causes the precipitation of carbides that could be metastable Ɛ-carbides that eventually turns into cementite. When high temperatures are reached the transformation that occur is the decomposition of the film-like austenite into alternated structure of α-ferrite and cementite. This is caused by holding the material at high temperatures as 450-500°C, for temperature below 400°C generally this kind of decomposition for low holding times is not detected [22]. When the material is further cooled to room temperature, the carbon depleted austenitic grains transform into brittle martensite which causes cold cracking problems to the material.

The principal welding parameter that influences the morphology of the LHAZ is the heat input. As previously explained in the *2.2* section, the heat input is correlated to the welding current, voltage and speed. It represents the quantity of energy that is apply to the material during the welding process. It can be stated that as the heat input value increases, the more pronounced will be the microstructure

transformation, and moreover the lower will be the hardness of weld material [22] [6]. From the pictures in *Figure 14* it could be noted the evolution of the microstructure due to different values of heat input applied during the welding process.

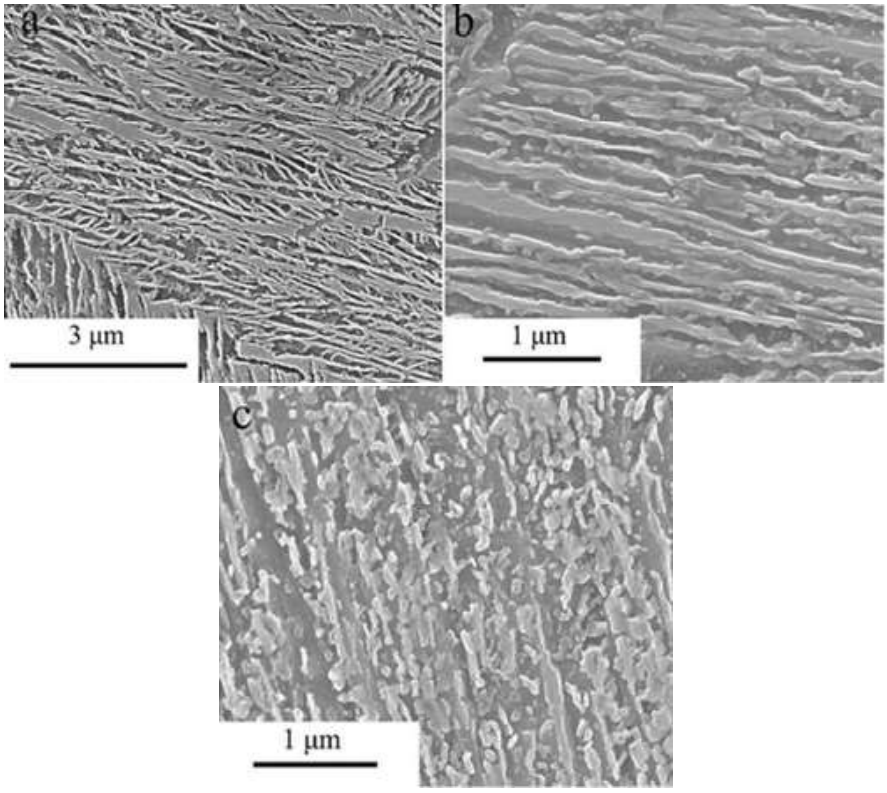

Figure 14, TEM pictures of general TRIP steel a) Base material microstructure b) Low welding heat input microstructure evolution c) High welding heat input microstructure evolution [18][14]

In the first picture it could be seen the base material microstructure, where film-like austenite is surrounded by bainitic ferrite matrix. In the picture b) the low welding heat input doesn't affect so much the structure: it can be seen that the long film austenite is not affected, the short ones are transformed into spherical particles that detach from the austenitic structure [22]. In the image c) high welding heat input destroys the material microstructure: both the long and short film-like austenite is decomposed into spherical particles [22]. These are carbides that precipitates due to the decomposition of carbon depleted austenite, it could be stated that the higher is the heat input and the lower is the retained austenite content in the final microstructure. This is caused by the redistribution of the carbon as the heat input increases that makes the austenite grains less stable and so more prone to degrade into cementite and ferrite [22].

Another important effect of the welding heat input is the coarsening of the microstructure: as the value of the welding heat input increases both the bainitic ferrite laths and the cementite precipitated becomes coarser [22]. This causes a strong depletion of ductility and in general of the mechanical properties of the metal, reducing the effect of the fine microstructure that is achieved with low isothermal heat treatment temperatures.

When in the LHAZ the temperatures reached values closer to Ac1, there is the complete decomposition of the retained austenite: the blocky austenite grains could transform into pearlite structure [6], the film-like austenite degrades into ferrite and globular cementite particles and doesn't form pearlite due to the too low space. In the zone strictly near to Ac1 there is the return to the thermodynamical equilibrium without any kind of bainitic transformation [6]. The bainitic ferrite laths morphology is no more recognizable with the formation of coarser polygonal grains with cementite precipitates [6].

In the HHAZ and in the fusion zone FS due to very high temperature reached (above Ac3) there is the recrystallization of austenite, which further due to cooling to room temperature will transform in brittle martensite [21].

3. Material

3.1 Alloy composition

The material which is studied in this work is a newly designed medium carbon, high silicon carbide-free bainitic steel. The chemical composition of the steel is reported in Table 1.

TRIP steel	C	Si	Al	Mn	Fe	Others
wt%	0,38	3,2	0,1	2,6	93,52	<0,5

Table 1 Chemical composition of bainitic steel

3.2 Microstructure and hardness of material “as received”

The material was produced in melting high quality raw material in an induction furnace and cast in form of an ingot. Then after the removal of the shrinkage cavity the material was reheated at 1200 °C and hot rolled in seven passes until final thickness of 20 mm.

The microstructural analysis was performed on sample prepared according to the standard metallographic preparation. To reveal the microstructure the specimen surface was etched with Vilella (100 ml ethanol, 5ml hydrochloridric acid and 1g picric acid).

The starting microstructure of the investigated steel consists in a mixture of martensite and bainite formed as consequence of the cooling process after the hot rolling. In addition, the initial hardness is $HV_{0.2}$=642±7.

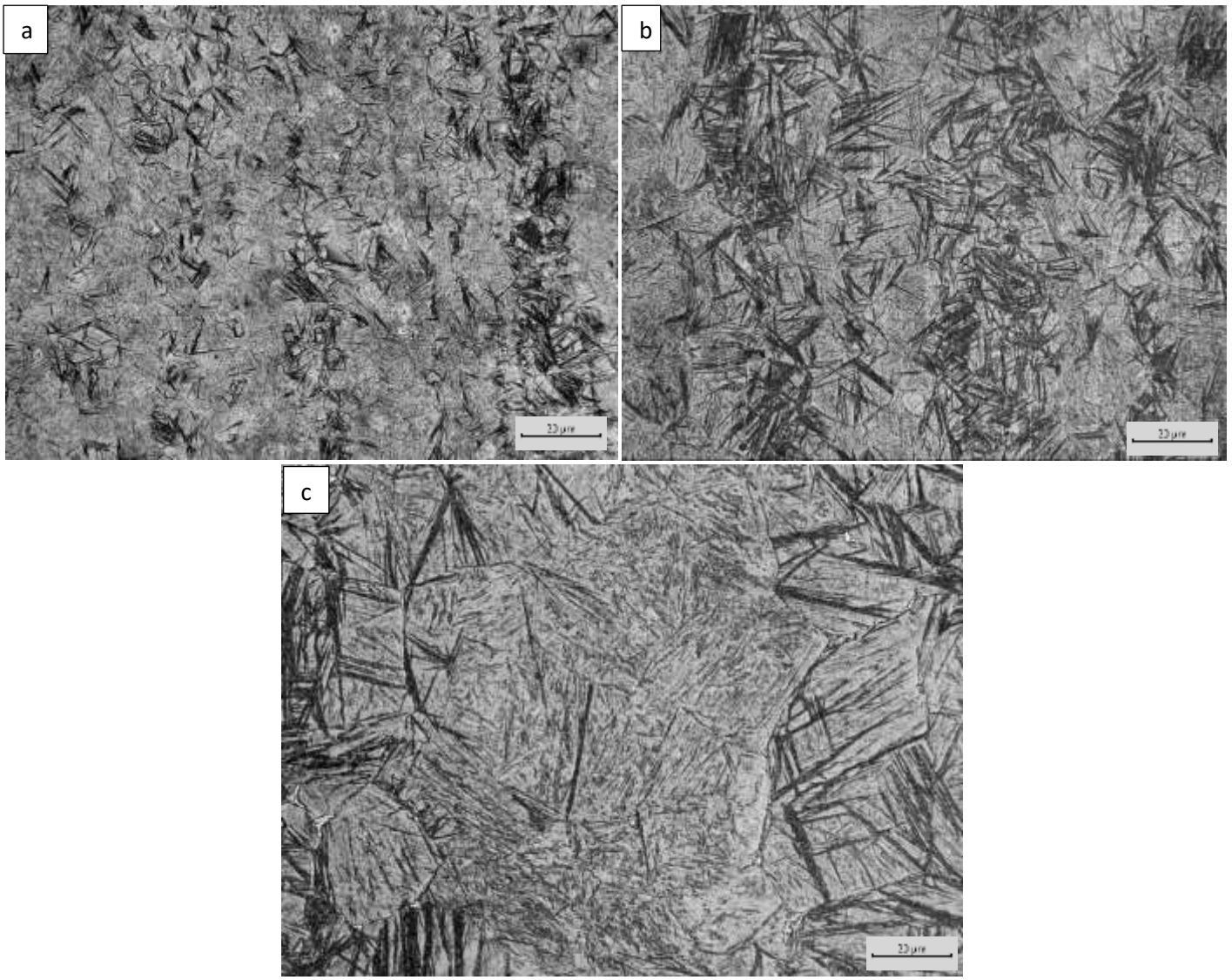

Figure 15 Optical microscope pictures of microstructure at a) 100x b) 200x c) 500x

4. Welding of the material

4.1 Welding process strategies

The TRIP steel is now welded. The welding procedures are conducted at INE s.p.a. laboratories, carried out by a professional welder. A sheet of TRIP steel has been cut for obtaining 8 smaller plates for being welded. These parts are 200x100x10 mm as sizes and have been chamfered from both the longer edges. All the cutting procedures are made by electro-erosion process, due to the high level of hardness of the material for the martensitic microstructure of the samples in the as given state.

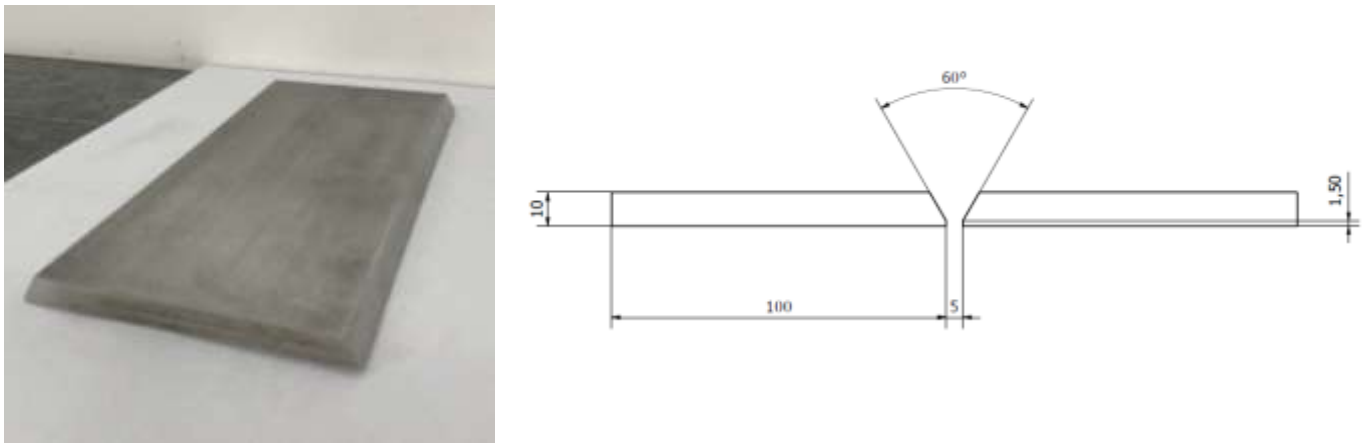

Figure 16 Single plate geometry representation

Experimental activity was done in collaboration with INE S.p.A, company leader in the production of welding consumables and machines. The experiments were carried out in the company laboratories, and the weld coupon were realized by a certified welding operator. Welding instrumentation and facilities were made available by INE S.p.A. Sample for realization welding coupons were machined by wire electrodischarge machining according to the scheme in *Figure 16* as received.

Three types of welding processes were considered in this research activity: Manual Metal Arc (MMA) Metal Inert Gas (MIG) and Tungsten Inert Gas (TIG). These three processes were selected for their high versatility in welding almost all the steel grades, and in order to have a complete overview of the response of the material to different welding processes, the critical aspects, etc.. For example, it could be seen how the material reacts at the two kinds of shielding methods: the gas shielding for the MIG and TIG processes and the flux coating for the MMA procedure.

The welding machine which is utilized for the welding procedures is the INE SKYLINE KME 4000, that allows to perform weld coupons with SMAW, GMAW and GTAW processes. This machine is characterized by an advanced technology, that lead to a adapts the welding parameters, including current and arc voltage, if the torch is not a constant distance from the weld bead.

All the welds were realised under constrains, spotwelding the specimens to two steel plates, in order to avoid distortion of the final weld coupon as shown in *Figure 17*.

Figure 17 Bainitic steel plates bounded with two plates through welding procedures

After the analysis of the three different welding procedures, that is completely explained in the successive *Chapters 5, 6, 7, 8,* another supplementary welding process is conducted. This consists in a MIG (GMAW) welding of TRIP steel plates that are already heat treated with the austempering heat treatment. This consists in the austenitization of the steel plates at 900 °C for 5 minutes. Successively, the plates are cooled in air 325 °C. and isothermally held at the same temperature in order to obtain a bainitic microstructure. The temperature of the plates was constantly monitored with a K-thermocouple.

4.2 Welding consumables

For the MIG process a INEFIL NIMOCR filler metal composition of the solid wire was used (EN ISO 16834-A: G 69 4 M21 Mn3Ni1CrMo), with chemical composition is reported in *Table 2.*
This is a high resistance steel, employed for welding of high strength steels with high elastic limit andultimate tensile strength above 770 MPa. In addition, the adopted filler is characterized by a yield strength value up to 690 MPa, according to the standard. It must be utilized with a shielding gas composition of 92% argon and 8% of carbon dioxide (M21 standardized composition). The diameter of the solid wire adopted in this work was ø 0.8 mm. The polarization of the wire adopted during the welding process was the "Direct Current Electrode Positive (DCEP)".

C %	Mn %	Si %	S %	P %	Cr %	Ni %	Mo %	Cu %	V %
0.08	1.60	0.50	0.007	0.007	0.30	1.50	0.25	<0.15	0.09

Table 2 Chemical composition INEFIL NIMOCR

For the MMA welding process, a INE 80 B steel for the consumable electrode composition was adopted (EN ISO 18275-A: E 62 4 2NiMo B 4 2 H5). It is a basic coated electrode, employed for the welding of high yield strength steels, with ultimate tensile strength up to 760 MPa. It has a yield resistance value up to 620 MPa, according to the standard. The polarization of the electrode during the welding process is positive (DCEP). The selected diameter of the consumable electrode was ø 2.5 mm. The chemical composition of the electrode coating and metal core is reported in *Table 3 and 4*.

C %	Mn %	Si %	S %	P %	Ni %	Mo %
0.07	1.30	0.20	0.005	0.010	2.10	0.50

Table 3 Chemical composition INE 80B

TiO_2 %	SiO_2 %	$CaCO_3$ %	CaF_2 %	FeSi %
0.1÷5	5÷15	25÷40	30÷40	5÷10

Table 4 Chemical composition electrode flux coating

Finally, a INETIG 120 S1 (EN ISO 16834-A: W 79 6 I1 Mn4Ni2Mo) was adopted for the TIG process. This is a low carbon steel with alloy Ni-Mo-Cr, with a high yield strength up to 800 MPa and an ultimate tensile strength higher than 900 MPa. The diameter of the TIG rod is ø 1.6 mm. The composition of the shielding gas is 100% Ar (I1 standardized composition). The polarization of the rod is Direct Current Electrode Positive (DCEN), otherwise from the other two welding processes.
The tungsten electrode composition adopted was a 2% ceriated one (color code: grey). The chemical composition of the filler metal is reported in *Table 5*.

C %	Mn %	Si %	S %	P %	Ni %	Cr %	Mo %	Cu %
0.08	1.7	0.5	0.007	0.007	2.3	0.1	0.5	0.15

Table 5 Chemical composition INETIG 120 S1

4.3 Welding parameters

In this study, considering the notable thickness of the plates a multi-pass welding process was necessary, and also pre-heating of the specimens, that, for all the process, was set as 200 °C

This corresponds to the interpass temperature of each layer deposited in the case of MMA, instead for the MIG and TIG welding processes the interpass temperature was set as 260°C. After each pass the temperature was monitored with a thermocouple pointed in the zone beside the weld bead.

The process parameters selected and obtained for the MIG, MMA and TIG welding processes are the following reported.

For the welding experiments without post welding heat treatments, realized on the austempered steel plates, the consumables and the parameter adopted were the same of the MIG welding procedure with the steel plates in the 'as received' state, thus INEFIL NIMOCR (chemical composition in *Table 2*). In addition, in order to have a direct comparison of the results, the welding parameters were kept constant.

Pass	Current [A]	Voltage [V]	Welding speed [cm/min]	Heat input [kJ/cm]	Interpass temperature [°C]
1	130	26	15	1,4	260
2	176	28	42	0,7	260
3	173	28	43	0,7	260
4	180	28	42	0,7	260
5	175	28	38	0,8	260
6	175	28	40	0,7	260

Table 6 MIG process parameters

Pass	Current [A]	Voltage [V]	Welding speed [cm/min]	Heat input [kJ/cm]	Interpass temperature [°C]
1	71	25	7	1,4	200
2	71	24	15	0,7	200
3	101	28	26	0,6	200
4	101	28	26	0,7	200
5	100	27	21	0,8	200
6	101	27	23	0,7	200
7	101	27	22	0,8	200
8	101	27	21	0,8	200
9	101	27	16	1,0	200
10	101	27	16	1,0	200

Table 7 MMA process parameters

Pass	Current [A]	Voltage [V]	Welding Speed [cm /min]	Heat Input [kJ/cm]	Interpass temperature [°C]
1	162	14	13	1,0	260
2	190	15	15	1,2	260
3	190	15	19	0,9	260
4	189	14	18	0,9	260
5	189	14	21	0,7	260
6	189	15	17	1,0	260
7	190	15	19	0,9	260
8	198	16	19	1,0	260
9	189	16	24	0,8	260
10	189	16	24	0,7	260
11	190	16	22	0,8	260
12	189	16	20	0,9	260
13	189	15	18	1,0	260
14	189	16	20	0,9	260

Table 8 TIG process parameters

The principal differences between the three process parameters could be recognized in: the lower welding speed of the MMA and TIG welding processes in comparison with MIG. This results in a higher heat input of the first two, where the TIG process reaches the highest values of it. The high heat input obtained with the TIG procedure is, moreover, justified by the higher value of current employed, and also from the negative polarization of the rod. This results in a lower consumption of the tungsten electrode and an higher heat transmitted to the base metal.

5. Instruments and methods

5.1 Penetrating liquids

The penetrating liquids analysis is employed for the examination of the metal surface condition for the detection of cracks, defects or cavities. The penetrating liquids procedure is conducted by following the Italian standard UNI EN 571-1. This consists in the utilization of a solvent, a red penetrating liquid and a white revealing. Initially the workpiece is cleaned from dirt and metallic sputters, to be efficiently cleaned by the solvent. Successively, the red penetrating liquid is applied on the whole surface of the two plates, in particular on the welded joint. After there is the removing of the excessive penetrating liquid and waiting for 5 minutes to permit the liquid to enter into the eventual cavities and porosities, that were formed during the welding process. The final step is to apply the white revealing spray to the surface of the plates. The surface condition is judged through visual inspection of the sample. This analysis is conducted after 3-4 days from the welding procedure, to permit the generation of eventual cold cracking phenomenon.

5.2 XRD diffractometer for residual stresses analysis

The evaluation of the stresses that are induced by the welding procedure have a paramount importance. In fact, it gives indications about the weld process influences the stresses state of the material, and how it reacts to the different thermal cycles with the generation of tensile or compressive loading situations.

The residual stresses are evaluated on the material using a portable x-ray diffractometer (XRD).

Figure 18 Representation of portable XRD diffractometer (a) XRD diffractometer sampling on MIG welded plates (b)

The XRD diffractometer works with an X-ray source, this impacts with the metal surface in the point where is desired to obtain the stress state. The light, which wavelength is comparable with the atomic spacing of the crystalline lattice, is scattered by the material and generates constructive interference when it interacts with the material in precise angular positions. In particular, the scattered waves interfere constructively when the difference between the path length of two waves is equal to an integer multiple of the wavelength [23]. The evaluation of the residual stresses is based on the Bragg's Law of diffractometry:

$$n * \lambda = 2 * d * sen\theta$$

Equation 6 Bragg's Law

Where n is an integer number, λ is the radiation wavelength, d is the interatomic spacing between two crystalline planes, θ is the Bragg's angle of diffraction.

The measurement of the residual stresses is obtained by the evaluation of the angle θ at which the radiation interfere constructively, by this the interatomic planes distance "d" is derived. The deformation of the crystalline lattice, which is proportional to the difference between the crystalline lattice planes distances of the stressed material and the "unstressed" one, gives the values of the residual stresses at the point that is measuring.

In particular, $(\varepsilon'_{33})_{\varphi\psi}$ is the normal strain component measured along the direction of the radiation beam. This is correlated to the lattice planes distances: d_0, the one of the material "unstressed", and $d_{\varphi\psi}$, the one of the material with residual stresses.

$$(\varepsilon'_{33})_{\varphi\psi} = \frac{d_{\varphi\psi} - d_0}{d_0}$$

Equation 7 Strain in function of the atomic interplanar distances

The deformation $(\varepsilon'_{33})_{\varphi\psi}$ could be correlated to the different strain and stress components by the following equation, in the case of triaxial stress state:

$$(\varepsilon'_{33})_{\varphi\psi} = \frac{1}{2}s_2\{\sigma_{11}\cdot(cos\varphi)^2 + \tau_{12}\cdot sin2\varphi + \sigma_{22}\cdot(sin\varphi)^2\}\cdot(sin\psi)^2 - s_1\{\sigma_{11}+\sigma_{22}\} + \frac{1}{2}s_2\{\tau_{13}\cdot cos\varphi + \tau_{23}\cdot sin\varphi\}\cdot sin2\psi$$

Equation 8 Correlation between deformation along radiation direction and different strain/stress components

It could be seen from *Equation 9* that the relation between $(\varepsilon'_{33})_{\varphi\psi}$ and $\sin\psi^2$ is not linear due to the presence of $\sin2\psi$, where ψ is the angle between the workpiece surface orthogonal axis and the direction of the radiation [23]. For this reason, the stress components are evaluated by the scanning in different ψ positions, in particular 11 from -30° to +30° with steps of 4-5° for each transition.

The output stresses given by the diffractometer consists in two components: σ_φ and $\tau_{\varphi3}$, where the angle φ is the one of the direction adjacent to the workpiece surface, which remains constant, where the stress is measured.

$$\sigma_\varphi = \sigma_{11}\cdot(cos\varphi)^2 + \tau_{12}\cdot sin2\varphi + \sigma_{22}\cdot(sin\varphi)^2$$

$$\tau_{\varphi3} = \tau_{13}\cdot cos\varphi + \tau_{23}\cdot sin\varphi$$

Equation 9 Definition of output stresses given by the diffractometry

The correlation between $d_{\varphi\psi}$ and $\text{sen}\psi^2$ is represented in the following chart. In particular, σ_φ is correlated to the slope of the curve in each point of the interpolating curve and $\tau_{\varphi 3}$ is correlated to the curvature of the curve in each point [23].

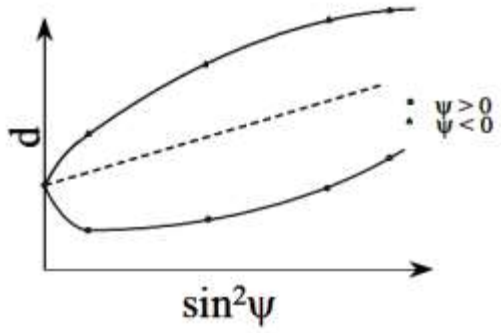

Figure 19 Correlation between $d_{\varphi\psi}$ vs $\text{sen}\psi^2$ with positive and negative values of ψ

5.3 Optical and SEM microscopy

The microstructural characterization of the welded samples was performed by optical and electron microscopy. The optical microscope is composed by an acquisition system, a camera, and an image analysis software. The pictures are acquired thanks to the reflection of light from the steel surface, where the microstructural zones appear different in color and intensity from each other for the differential corrosion operated by the chemical etching. Light from a source, properly collimated by diaphragms and capacitors, is directed through a mirror to the surface of the specimen after passing through the lens. The reflected light is concentrated back into the objective lens; the light signal is deflected by the prism toward the ocular lens, which allows magnified viewing of the preparation. Finally, the signal can be deflected by a mirror and sent to a photographic screen or camera. The magnifications that could be employed are 50x, 100x, 200x, 500x, 1000x.

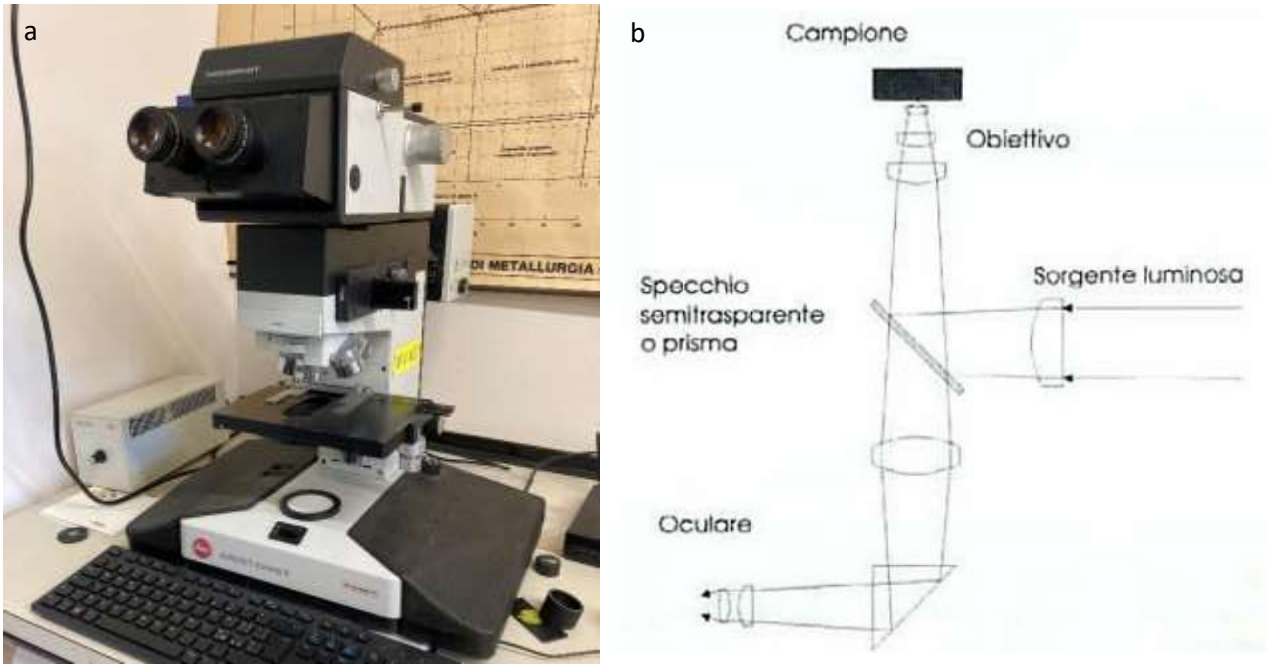

Figure 20 Leitz Aristomet (Beltrame group) optical microscope (a) and schematization of the operating principle (b)

For the analysis of the welded steels, the plates are cut longitudinally with the generation of a section that comprises the fusion zone, heat affected zone and base material. To be analyzed at the optical microscope the steel surface must be flat, in order to obtain a uniform focal plane, and bright, to guarantee the maximum reflection of the light. These requirements are achieved by the mounting of the sample in epoxy resin, and by the grinding and polishing procedures, according to the standard metallographic preparation.

The sample section, to be mounted into the epoxy resin, are reduced to a width of about 35 mm.

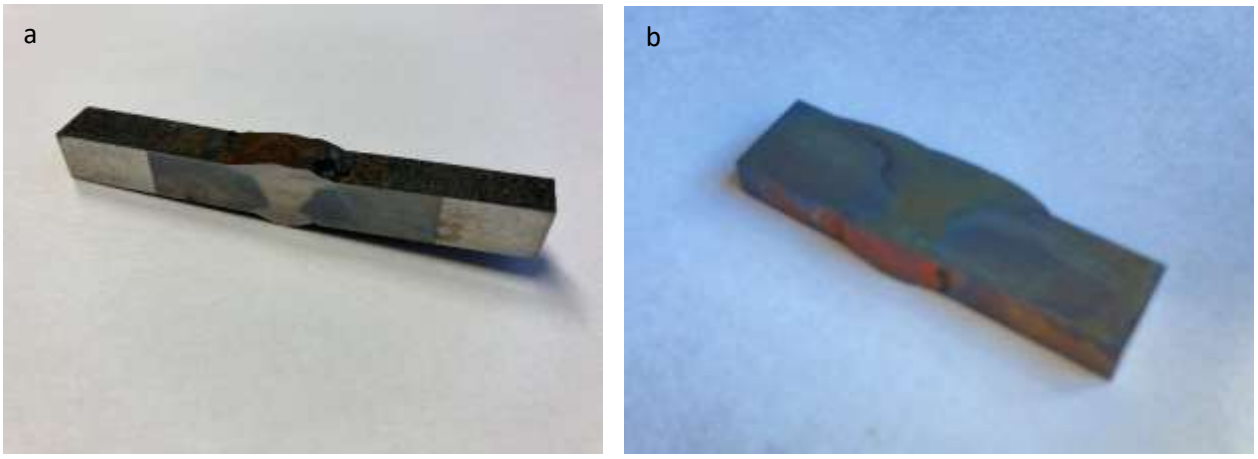

Figure 21 Initial welded sample slice (a), reduced welded sample slice before the epoxy resin embodiment (b)

The sample were mounted into epoxy resin thanks to a metallographic mounting machine, in which the epoxy resin filled with graphite powder to achieve electric conduction, is introduced as granules that surround the welded metals. Successively, the machine applies high pressure and temperature that cause the thermosetting of the epoxy resin.

The sample successively were grinded and polished. The grinding was performed using SiC papers, with 120, 320, 500, 800, 1200 grit. The polishing step was obtained using of clothes soaked with colloidal diamond polycrystalline suspensions of 3 and 1 µm dimensions.

In order to reveal the microstructural constituents, grain boundaries, defectes, etc. chemical etching was performed. The etchant employed were the Klemm's I and the Nital 2. The first is used for marking the microstructural evolution due to the welding process. The different heat affected zone sections are highlighted thanks to this etchant. It consists in a solution of 50 mL of water and 1 g potassium metabisulfite ($K_2S_2O_5$). The Nital 2 etchant is used when the bainitic microstructure obtained after austempering heat treatment, or martensitic microstructure after quenching heat treatment, must be highlighted. It is composed by 98% of ethanol and 2% of nitric acid.

The microstructure composition of the welded samples was evaluated with very high magnification through Scanning Electron Microscope (SEM) observation. The Scanning Electron Microscope exploits the generation of a high-energy electron beam in a vacuum. The beam is focused by a lens system and deflected to scan an area of the sample. The beam-sample interaction generates various signals that are acquired by appropriate detectors and then processed to form a 3-D gray-level image. A beam of electrons with kinetic energies between 1 and 30keV and called primary electrons is generated by an electron gun (cathode) located at the top of the column, the beam is attracted toward the anode, condensed by collimating lenses and focused through objective lenses onto the massive sample i.e., one of sufficient thickness enough not to be crossed completely by the incident electrons. The electron beam strikes the sample, producing, x-rays, auger electrons, absorbed electrons, secondary, backscattered electrons. The set of possible paths of electrons in the medium goes to define the volume of interaction which at the same energy is inversely proportional to Z and goes to define

the spatial resolution. These electrons are collected by a detector for secondary electrons and one for electrons backscattered, converted into electrical signals and amplified. These are converted into pixels and processed by a system equipped with a computer. X-rays sell collected by a Si detector. The principal advantages of SEM are the high resolution, high magnifications (up to 100000x), high depth of field, easy sample preparation.

Figure 22 Zeiss EVO Scanning Electron Microscope (SEM)

5.3 Hardness tests

The hardness, that characterizes the welded specimens in the different zones, was evaluated with Vickers micro-hardness tests. For this purpose, a Shimadzu Vickers testing machine was employed. All the experiments were conducted with a load of 300 g, therefore all the results are reported as $HV_{0,3}$. The indentation are examined at the optical microscope, since their size is in a range of 30-50 μm. The materials hardness is evaluated with the measuring of the two diagonals of the rhombic indentations, making an average of the values obtained. Profile measurements were performed, with indentation with distance of 300-500 μm.

Figure 23 Shimadzu hardness testing machine

5.4 XRD diffractometer for phase identification and quantification

The microstructure composition of the welded sample is evaluated through a fixed XRD diffractometer. The working principle is based on the interaction of an x-ray beam, generated from an x-ray source, with the metal surface in a chosen section. The atomic layers that characterize the crystalline lattice (FCC, CCC) produce the scattering of the radiation thanks to the interaction with the electrons (elastic scattering). The electron scattering produce radiations, which generates destructive interference between each other in most of the directions. There are particular directions in which a constructive interference is obtained. These are defined from the Bragg's law (see *Equation 7* of *Chapter 5.2*). Unlike the portable XRD diffractometer employed for residual stress analysis, in this case the ψ angle, so the one between the workpiece surface orthogonal axis and the direction of the radiation, is fixed. What is varied is the 2θ angle, so the Bragg's angle that characterize a particular crystalline lattice. The x-ray radiations that impact the metal surface are reflected and detected by a receiver, which evaluates the constructive interference peak if a particular phase is detected (α-ferrite, γ-austenite). Phase quantification was performed through conventional X-Ray diffraction, with a Siemens D500 diffractometer, with Cu-Kα radiation (λ=1.5405Å) and monochromator on the detector side, operating at 40 kV and 30 mA. The scanned range was 40-105°, with a step size of 0.025° and 3 s counting time. Rietveld analysis on XRD patterns was performed with the support of MAUD software. XRD sample preparation was performed using the standard metallographic procedure, with final cycles of etching and polishing to remove deformed layers and avoid the introduction of artifacts on the measurements and the martensite due to grinding (TRansformation Induced Plasticity effect).

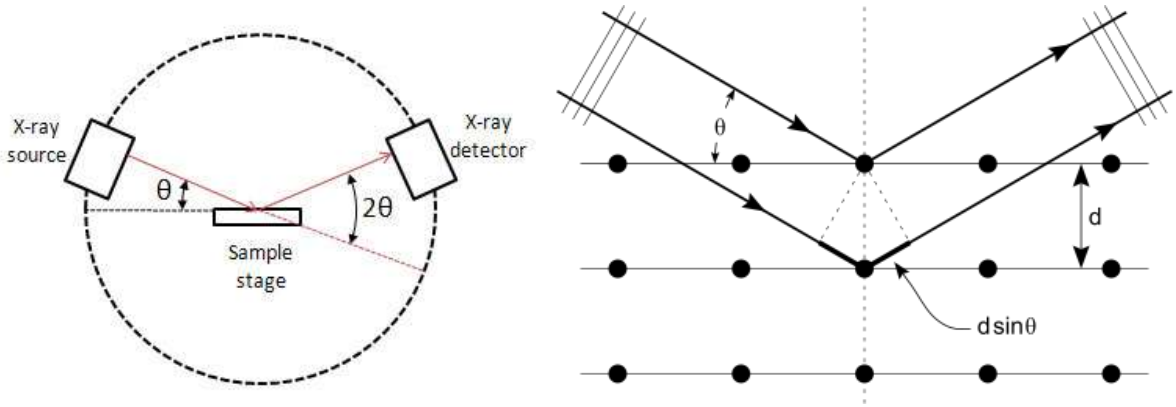

Figure 24 Schematization of XRD diffractometer and Bragg's angle of scattering

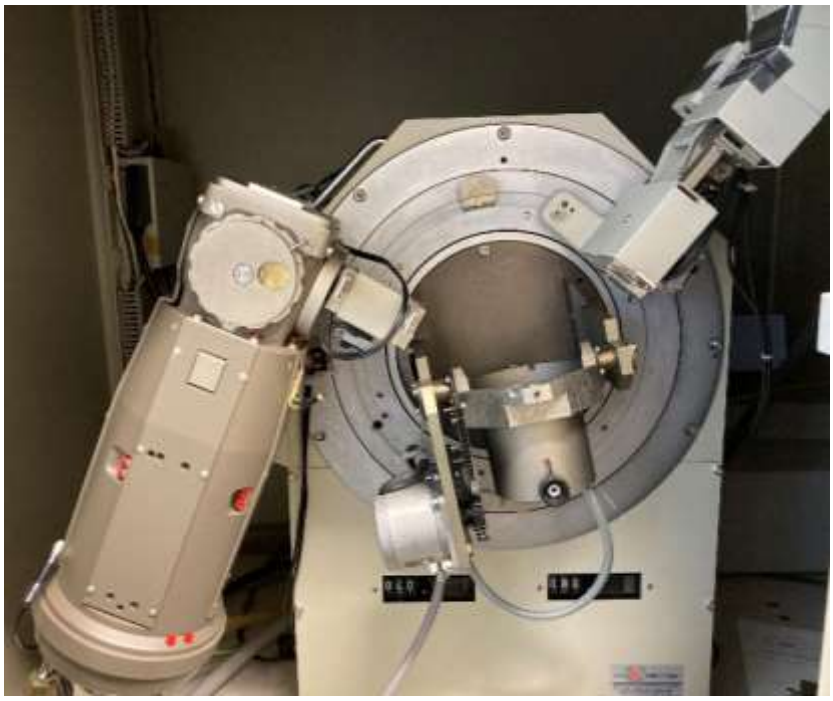

Figure 25 Picture of XRD diffractometer

5.5 Tensile tests

The mechanical properties of the welded sample are tested with a tensile machine. The steel plates are cut longitudinally with wire-electrodischarge process. This is done to achieve a homogeneous thickness on the tensile samples, which results in an equal distribution of stresses when the specimen is under loading.

The welded specimens are then grinded and polished to get a bright and clean surface, free from oxides and dusts. Before the tensile tests, the welded section is slightly etched with Nital 2 attack to highlight the fusion zone and the heat affected zone. Successively, the different zones are marked, in order also to define the clamping position of the machine jaws.

The tensile testing machine is composed by two clamps that fix the specimen, which are supported by a horizontal bar; these apply an incremental load which is registered during time. Since no strain gauge is employed during the tests, the deformation of the workpiece is evaluated only by the space travelled by the supporting horizontal bar.

The principal mechanical characteristic that is evaluated through the tensile tests is the Ultimate Tensile Strength (UTS), so the maximum stress reached by the welded steel specimen under loading.

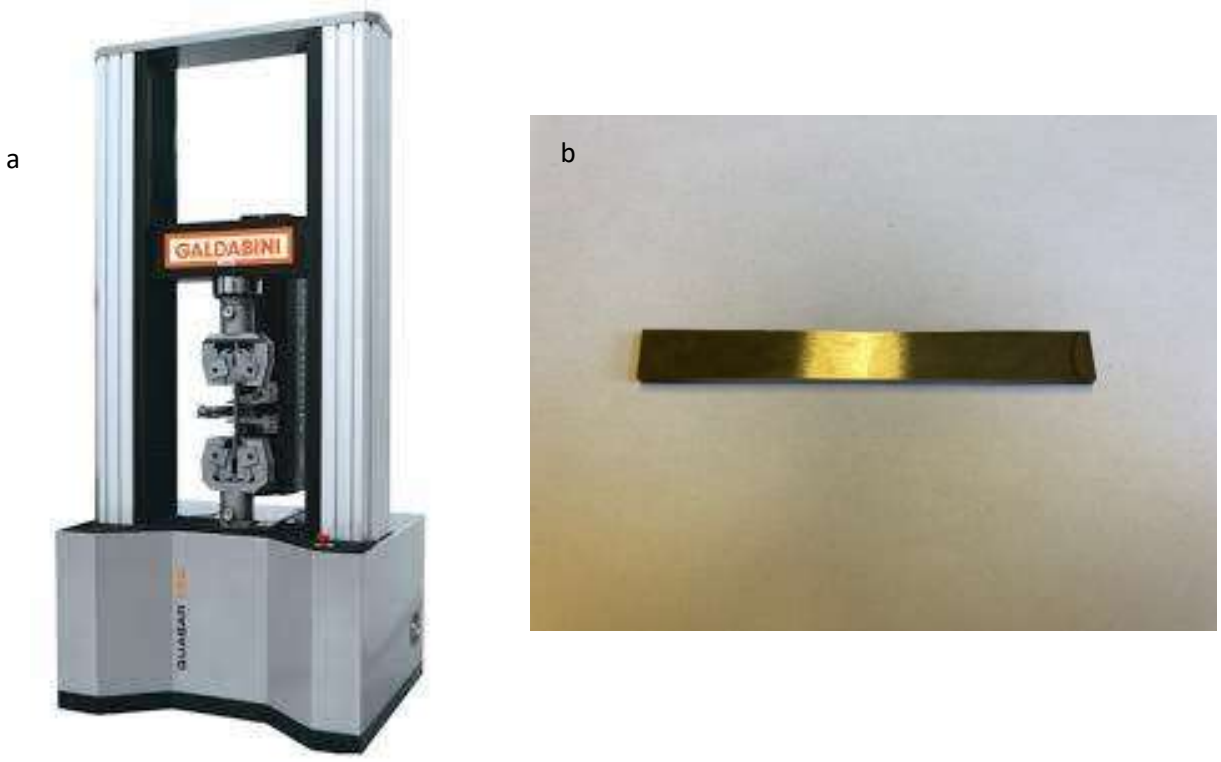

Figure 26 Representation of the Galdabini tensile test machine (a) and sample for the tensile tests (b)

6. MIG (GMAW) process results

6.1 Visualization and penetrating liquids

The resulted weld bead is promising. It could be seen that a homogenous welding structure, from a macro point of view, is obtained. From *Figure 27 a* it could be noted the heat affected zone on the surface of the two plates. During the welding process there was also the generation of sputters which deposits and solidified on the metal surface in form of semi-spheres.

Figure 27 Weld bead obtained with MIG process (a), glassy product on the weld bead (b)

From *Figure 27 b* it could be seen the presence of a vein of glassy product, which is formed along the whole weld bead in correspondence of the interface between the last two passes. This is due probably to the high content of silicon in the base material and in the filler metal wire composition, which generates silicates that are low melting compounds that stay at the liquid state on the surface for the whole welding process.

During the welding processs, macro-cracks or breakage of the metals weren't verified.

To better assess the generation of cracks and macro porosities, an investigation of the weld bead condition was carried out with the penetrating liquids.

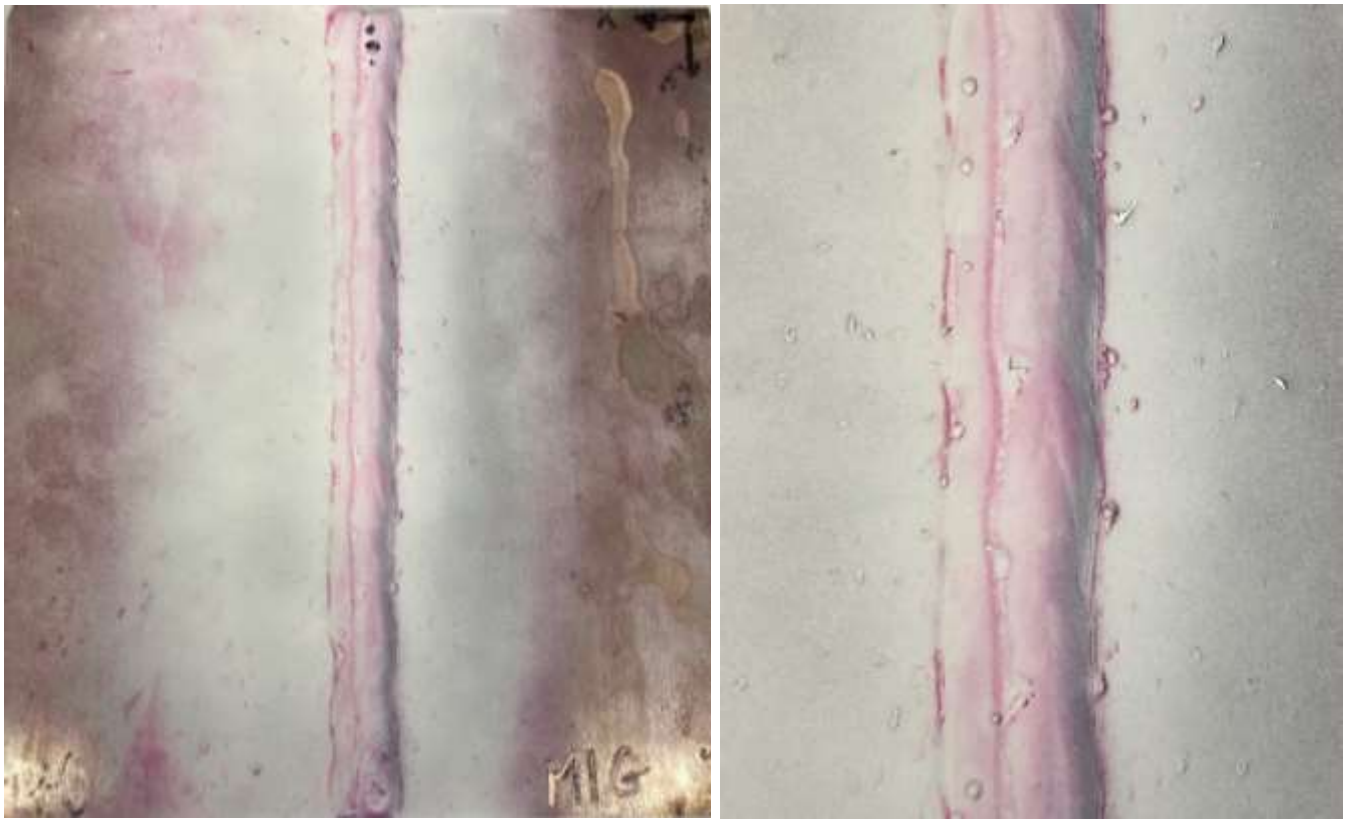

Figure 28 Results of penetrating liquids analysis on MIG weld bead

The results obtained from the application of the white revealing on the red penetrating liquid, are promising: no cracks or other macro defects are detected. In *Figure 28* it could be noted that the red liquid highlights the glassy product and some parts of the weld bead base, but these are not considerable as cracks or defect but as accumulation of the penetrant.

6.2 Residual stresses

The residual stresses are analyzed in different points on the weld bead and base material. The position of the points for the evaluation are chosen as represented in *Figure 29*.

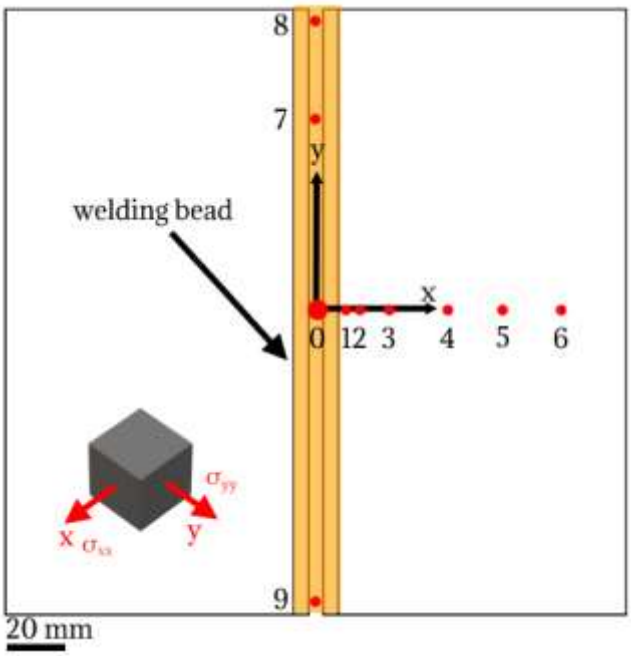

Figure 29 Distribution of points where the residual stresses are analyzed

The points are analyzed in two different scanning planes where ψ is varied: the X plane, so in the longitudinal direction respect to the welding one, and the y plane, the one parallel to the welding direction.

The residual stresses, on a single bainitic steel plate in the "as received" state, are evaluated. The XRD analysis gives as results in the X plane direction of scanning a compressive residual stress up to -861 MPa, in the Y plane the output value is -310 MPa. These results are justified from the hot rolling process that is employed as final step to produce the steel plates, moreover the material undergoes also to surface preparation treatments with electrodischarge machining.
The XRD diffractometry results for the plates welded by MIG process are reported in *Table 9*.

POINT	Stress σ_φ in X plane [MPa]	Stress σ_φ in Y plane [MPa]
0	204	472
1	48	422
2	-272	-180
3	-594	-493
4	-560	-409
5	-712	-500
6	-771	-550
7	377	426
8	199	235
9	136	170

Table 9 Results of residual stresses analysis of MIG welded plates

The results given by the XRD diffractometry stated that the welding process induce tensile stresses on the metallic plates. This is confirmed by the progressive reducing of the compressive stress state from the weld bead to the base metal side.

From the results achieved with the residual stress analysis in the points 0 and 1, the two different planes of scanning results with dissimilar stress states. In particular, the two points when analyzed in the longitudinal plane are slightly under tensile stress state, instead when are evaluated in the Y plane the material is under tensile stress state. This is probably due to the welding direction that takes the material under tension in the plane parallel to the process path. The other points analyzed with the two different scanning planes gives results which are comparable between each other.

6.3 Optical microscopy and SEM

The welded plates microstructure was analyzed at the optical microscope. In particular, to study the microstructure evolution due to the thermal cycles caused by the welding process, the plates were cut transversely with a cutter. The plates were initially cut at 2,5 cm from the starting point of the weld bead. This was done to separate the initial part of material, which was welded with slightly different parameters (as could be seen in *Table 8*) and has been influenced from the procedure of arc initiation, from the whole weld bead. The metal microstructure in the initial part of the weld bead could be influenced, for the reasons reported before, and couldn't represent well the real welding microstructure that was generated in the central part of the weld joint. The welded slices were mounted in epoxy resin, in order to be grinded and polished without difficulties to generate a flat metal surface. To reveal the different welding zones of the microstructure the sample was etched with Klemm's I (100 mL of water, 10 g of $Na_2S_2O_3$, 3 g $K_2S_2O_5$) and analyzed at polarized light with the optical microscope.

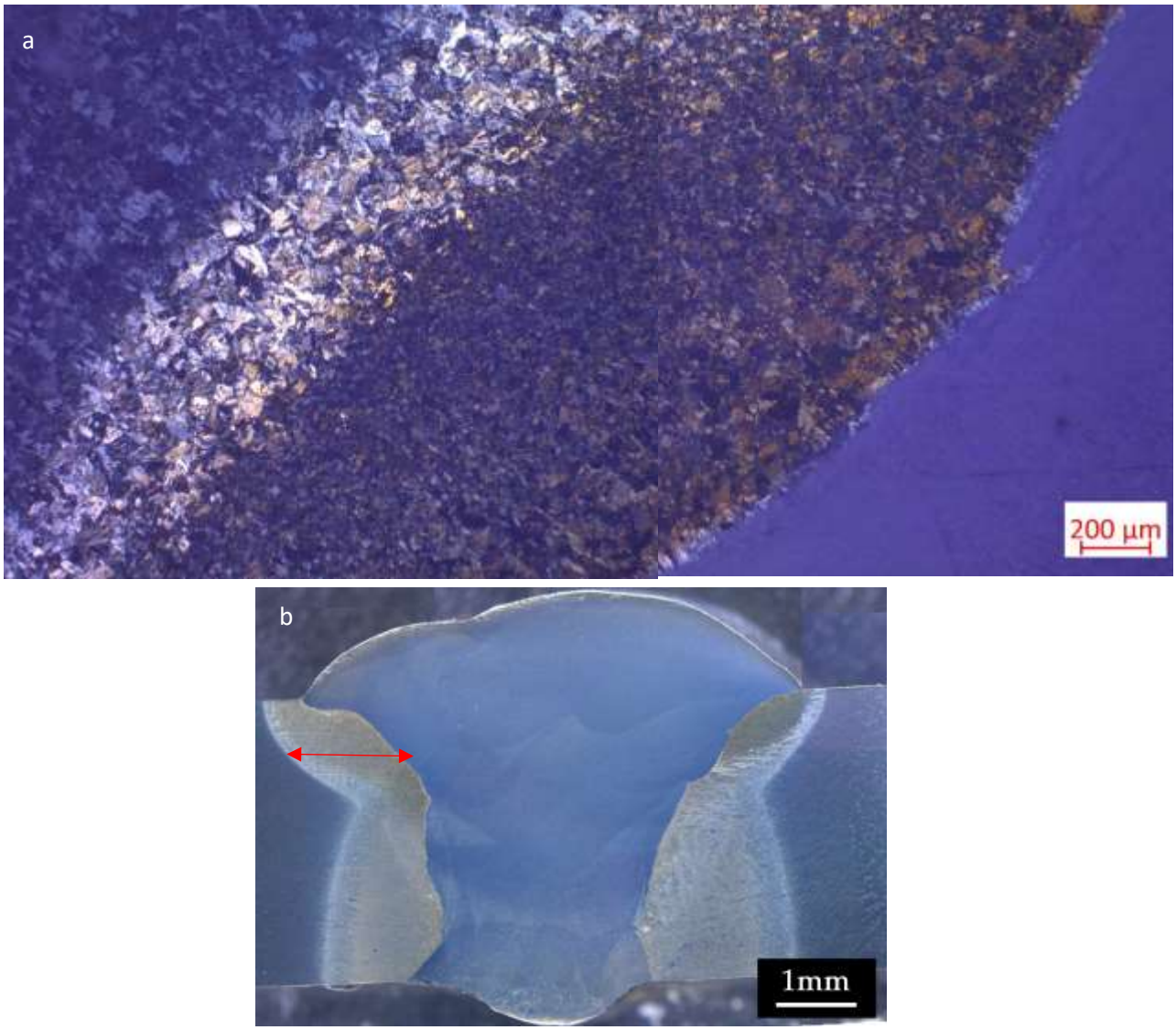

Figure 30 Optical microscope picture of welded sample heat affected zone (a), representation of the weld bead section (b)

In *Figure 30* are represented the different microstructural zones that were generated from the MIG welding process. It could be clearly distinguished the fusion zone (FZ) on the right, which is colored in light blue and presents a homogeneous structure. The first assumption that could be done for the metallurgical constitution of the FZ, mind the chemical composition of the filler metal INE NIMOCR, is that is composed in the majority by a α-ferrite.

Immediately after the FZ a mixing-coarsened zone could be individuated, this is generated by the joining of the base material and the filler metal during the deposition process. This zone presents huge grains for the high temperatures and thermal cycles that undergoes during the welding process. It represents the high heat affected zone (HHAZ). In the center of the HAZ it could be distinguished a refined microstructure of the metal, this is due to the different temperatures and cooling rate from the thermal cycles of the welding procedure. The end of this zone is recognized as the low heat affected zone (LHAZ). In the final part of the LHAZ there is a slight coarsening of the microstructure grains. These presents the same metallurgical composition of the base material (BM), which could be recognized as the blue microstructure on the left. In the base material and in the last slight coarsened zone of the HAZ a martensitic microstructure is recognized. The pictures in *Figure 30* represents the zone at the height where the Vickers micro-hardness indentations are taken.

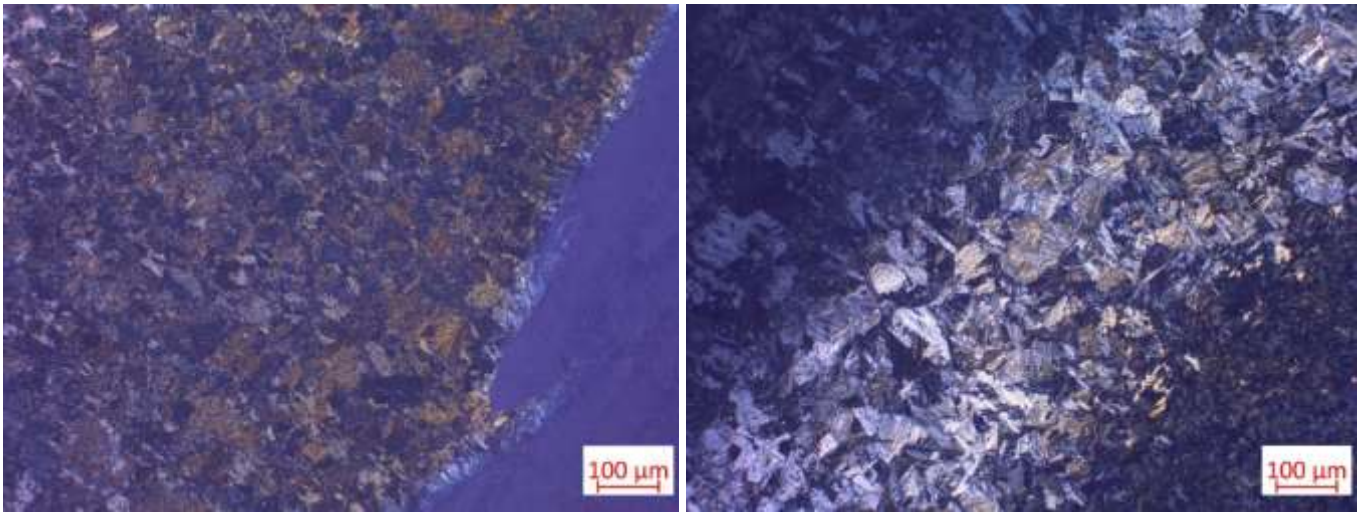

Figure 31 Higher magnification pictures of MIG heat affected zone

The welded metals microstructure has been analyzed at the SEM microscopy. There is a distinction between different zones of the welded metals with MIG process: the fusion zone is distinguished in

high-fusion zone (HFZ), so the one corresponded to the last passes of the process, and the low-fusion zone (LFZ), so the one of the first passes. A zone of mixing between the base material and the filler one is individuated, this is recognized as interface mixing zone (MZ). Successively there is the heat affected zone (HAZ) and the base material (BM).

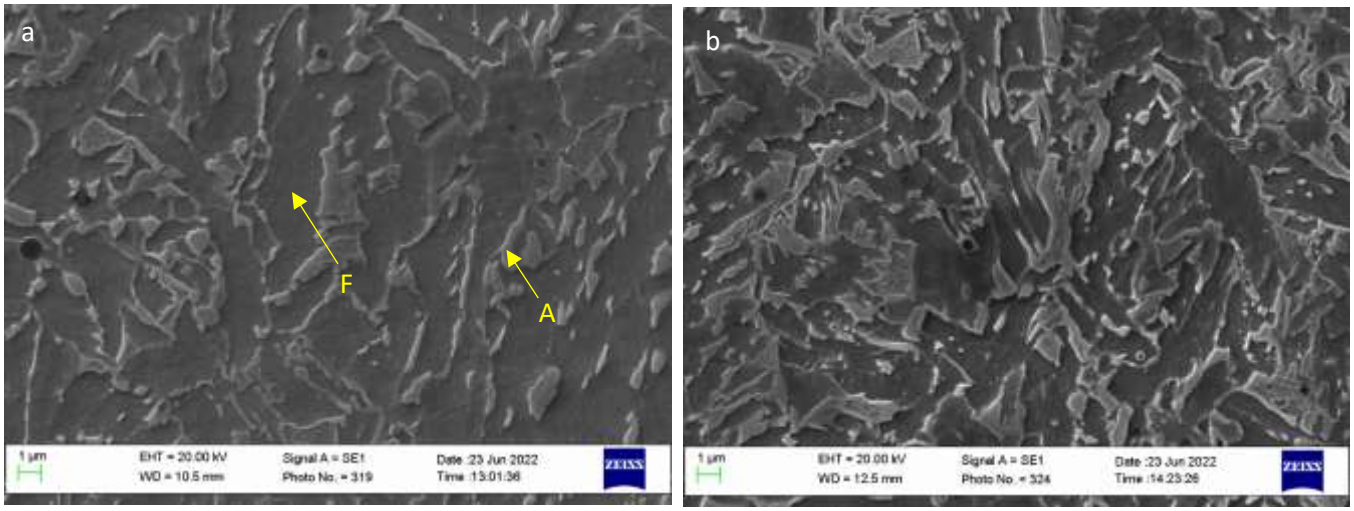

Figure 32 SEM pictures of high fusion zone HFZ (a), and low fusion zone LFZ (b). F ferrite, A austenite

From the images on *Figure 32* it could be noted that the fusion zone isn't characterize by a microstructural morphology such as needles with martensite or bainite so, knowing the very low carbon content that denotes the chemical composition of the filler metal INEFIL NIMOCR (up to 0,08% wt.), it could be said that the microstructure of the fusion zone is composed mainly by α-ferrite. This will be confirmed also by the hardness tests and XRD microstructural examinations. From the two pictures compared above it could be distinguished a more compact and dense structure in the LFZ in comparison with the HFZ. This could be explained by the greater number of thermal cycles that the material undergoes in the low fusion zone, due to the number of passes that are furtherly applied after its generation.

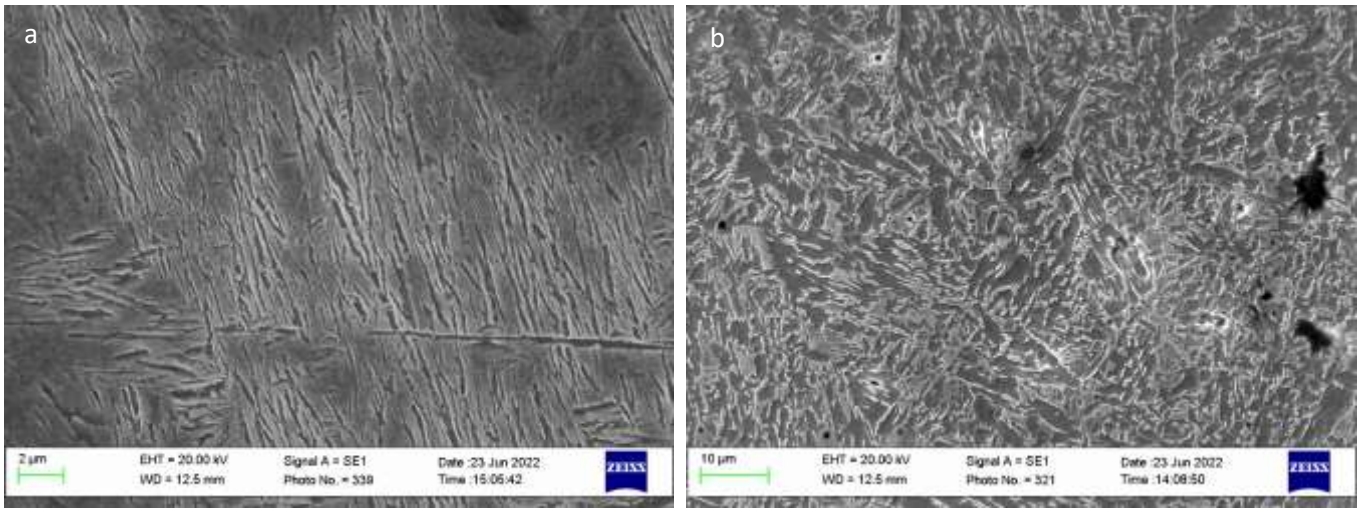

Figure 33 SEM images of heat affected zone HAZ (a), and interface mixing zone MZ (b)

From the pictures of *Figure 33* it could be stated that the microstructural morphology of the mixing zone (b) is between the one of the filler metal, so ferritic, and the base material, so martensitic. The central heat affected zone (HAZ) is composed by an acicular microstructure: the original martensitic microstructure of the base material is altered due to the thermal cycles incurred during the welding process. This could take to the tempering of the martensite in the HAZ far from the weld bead, resulting also in a porgressive reduction of the hardness.

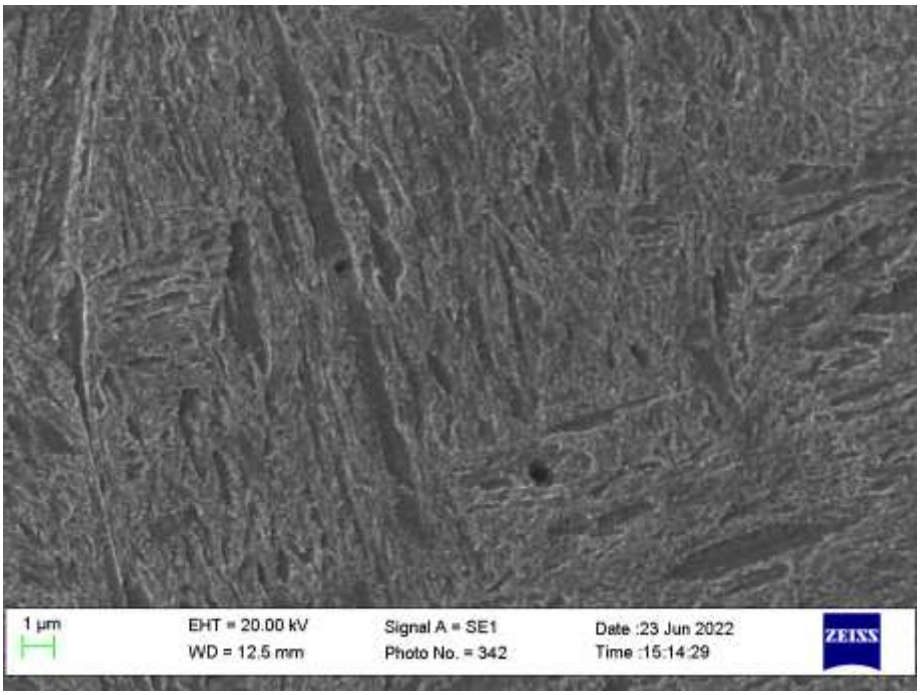

Figure 34 SEM picture of base material zone (BM)

In *Figure 34* the martensitic microstructure of the base material is represented, this zone isn't altered from the welding process, maintaining its original microstructure. This will be confirmed also in the Vickers micro-hardness tests.

6.4 Hardness

The hardness of the various zones developed due to the MIG welding process was evaluated with micro-Vickers hardness tests. The examinations were conducted with a Shimadzu hardness tester with a 300 g load (results are reported as $HV_{0,3}$). For the evaluation of the material hardness the two diagonals of each indentation are measured, deriving the average value from the two.

The indentations are applied at about 2 mm from the top height of the weld bead, with the generation of a "seam" along the longitudinal direction of the samples. This was done to achieve the hardness of all the different zones that characterize the welded plates. Moreover, the development of the hardness from the vertical top to the base of the weld bead is analyzed.

Figure 35 Representation of the micro-Vickers indentations

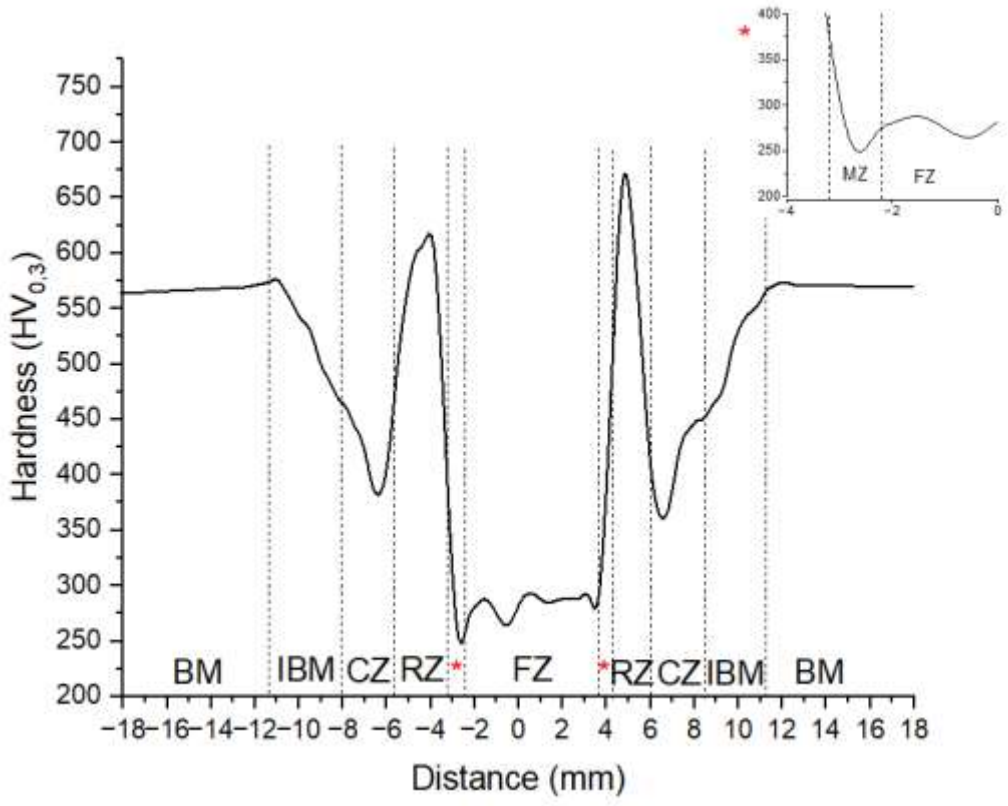

Figure 36 Material hardness in function of the distance from the center of the fusion zone (Path 1)

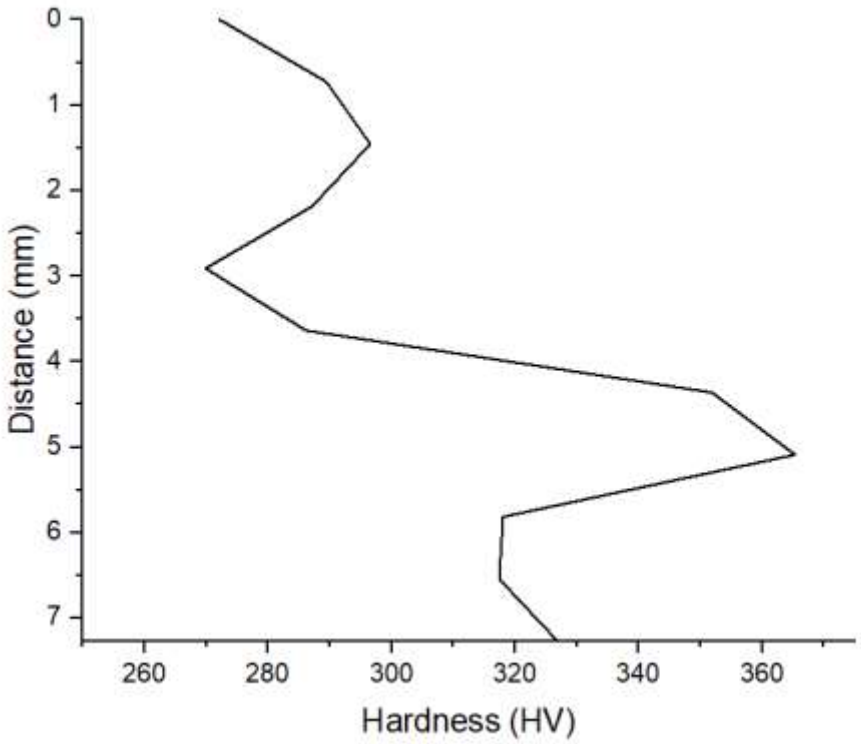

Figure 37 Material hardness in function of the distance from the top of the fusion zone (Path 2)

The *Figure 36 & 37* represents the obtained results of the Vickers micro-hardness tests for the two different paths, the horizontal and the vertical one. Concerning the hardness values development in the horizontal direction, it could be stated that the results are conforming to the microstructural composition that is examined at optical and SEM microscope. In fact, from *Figure 36* the different zones that characterize the welded metals are reported with their respectively values of hardness. The central valley of the curve corresponds to the fusion zone FZ. This cover a longitudinal space of about 6 mm, and is characterized by 290-300 $HV_{0,3}$ as hardness value. This is explained by the absence of hard phases in the fusion zone, due to the low content of alloying elements, in particular carbon, in the filler material. After the FZ, the zone where the base material and the filler metal are joined, is individuated as the mixing zone MZ. In this a slightly higher hardness value of 325-340 $HV_{0,3}$ is reached. Suddenly after, the material shows a marked hardness peak of 625-650 $HV_{0,3}$. This is reconducted to the refined zone RZ obtained in the heat affected zone, where the material reaches sufficient high temperatures (higher than Ac3) to be, after the cooling stage in air, refined. Successively to the refined zone peak, the material hardness values are reduced to 375-400 $HV_{0,3}$. These results are related to the coarsened zone CZ. In this section the base material microstructure, due to the thermal cycles during the welding process, is taken to high temperatures that causes the enlargement of grain size (between Ac1 and Ac3). As it goes far from the coarsened zone valley, in the influenced base material zone IBM, the metal results less altered from the welding heating cycles,

which is detected as an increase in the hardness values. It passes from 375 $HV_{0,3}$ to 570 $HV_{0,3}$ in a longitudinal distance of 4-5 mm. After the material hardness stabilizes at 575-580 $HV_{0,3}$, which is considered the one of the martensitic base material BM microstructure.

From *Figure 37* it could be seen that the material hardness remains in the interval between 270 and 320 $HV_{0,3}$, where the top of the weld bead results slightly softer than the base. This could be related to the higher number of thermal cycles at which the material at the base of the weld bead undergoes, causing the generation of harder phases.

The overall wideness that characterizes the heat affected zone in the MIG welded plates is of 10-11 mm.

The objective of the Vickers tests is not only the evaluation of the material punctual hardness in the different paths along the welded plates, but also to determine the microstructural evolution that is caused by the thermal cycles of the welding process.

6.5 XRD for phase identification and quantification

The MIG welded samples microstructure composition is examined with XRD diffractometer.

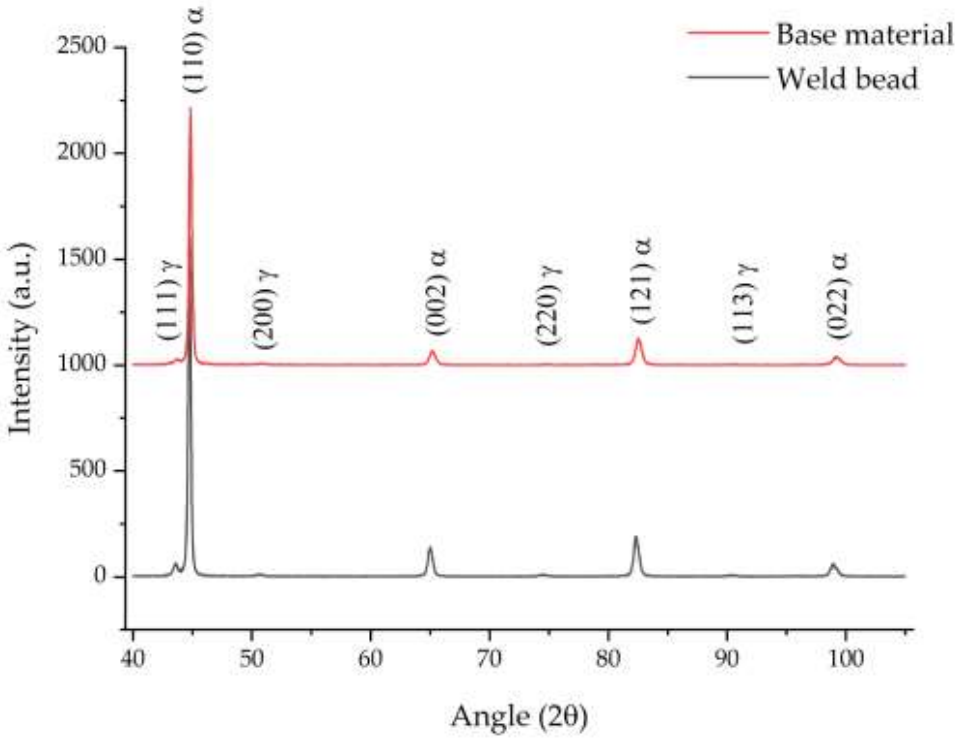

Figure 38 XRD pattern resulted for phase identification of MIG sample 'as weld'

Zone	V_γ	X_γ	V_α	X_α	$V_{\alpha'}$	$X_{\alpha'}$
Weld bead	4.37	1.21	91.09	0.03	4.52	0.17
Base material	5.50	0.58	-	-	94.5	0.24

Table 10 Results of XRD phase quantification of MIG sample 'as weld'. V_γ, volume fraction of retained austenite, X_γ, carbon content wt. % in retained austenite, V_α, volume fraction of α-ferrite, X_α, carbon content wt. % in retained austenite, $V_{\alpha'}$, volume fraction of martensite, $X_{\alpha'}$, carbon content wt. % in martensite.

The weld bead composition is characterized principally by α-ferrite. This agrees with the low carbon content of the filler metal employed. The austenite and martensite content are very low, this since the welded sample is not subjected to a post-welding heat treatment. This analysis confirms the fusion zone microstructure represented in SEM pictures (*Figure 32*) where the austenitic islands are surrounded by ferritic matrix.

In the base material it can be noted that the microstructure is mainly composed by martensite. This result is in concordance to what was expected, since the bainitic steel was welded in the 'as received' condition.

6.6 Annealing and quenching heat treatments

The welded sample was subjected to annealing heat treatment. This is done to analyze how the base metal and, in particular, the filler material react to the austenitize and slow cooling thermal cycle. The heat treatment was conducted with the utilization of a heat furnace. The welded metals are subjected to the austenitize stage for 5 minutes at 900°C. Successively the heat furnace was turned off and the metal slowly cools till reaching the room temperature 25°C.

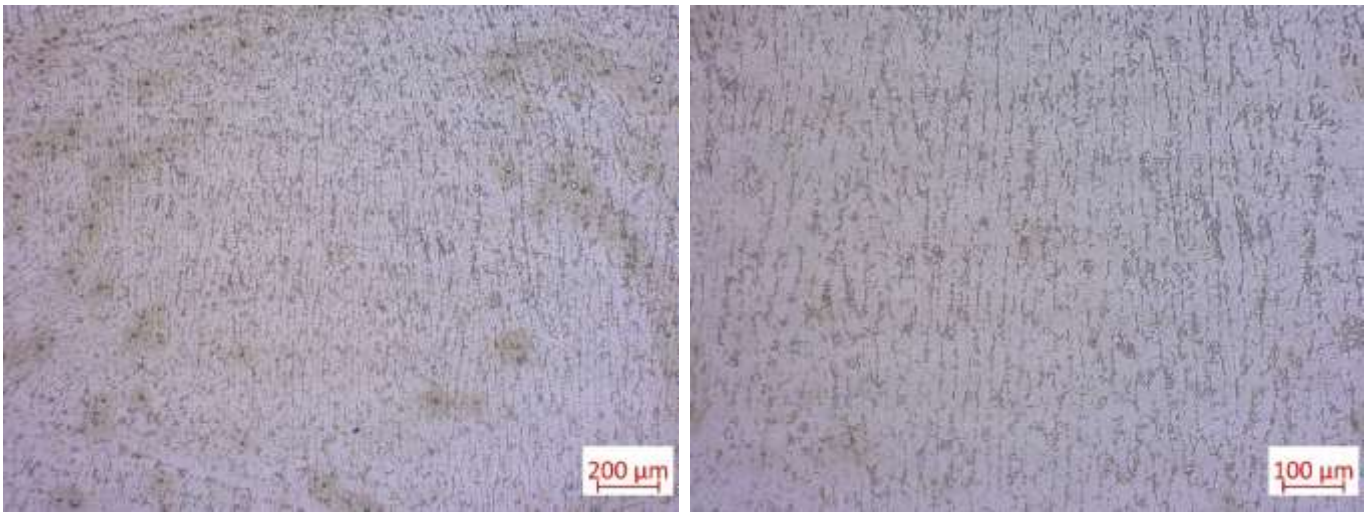

Figure 39 Optical microscope pictures of fusion zone FZ after annealing heat treatment

In *Figure 39,* the microstructure of the FZ after the annealing heat treatment is represented. It is characterized by the solidification columnar grains, composed mainly by α-ferrite and traces of austenite.

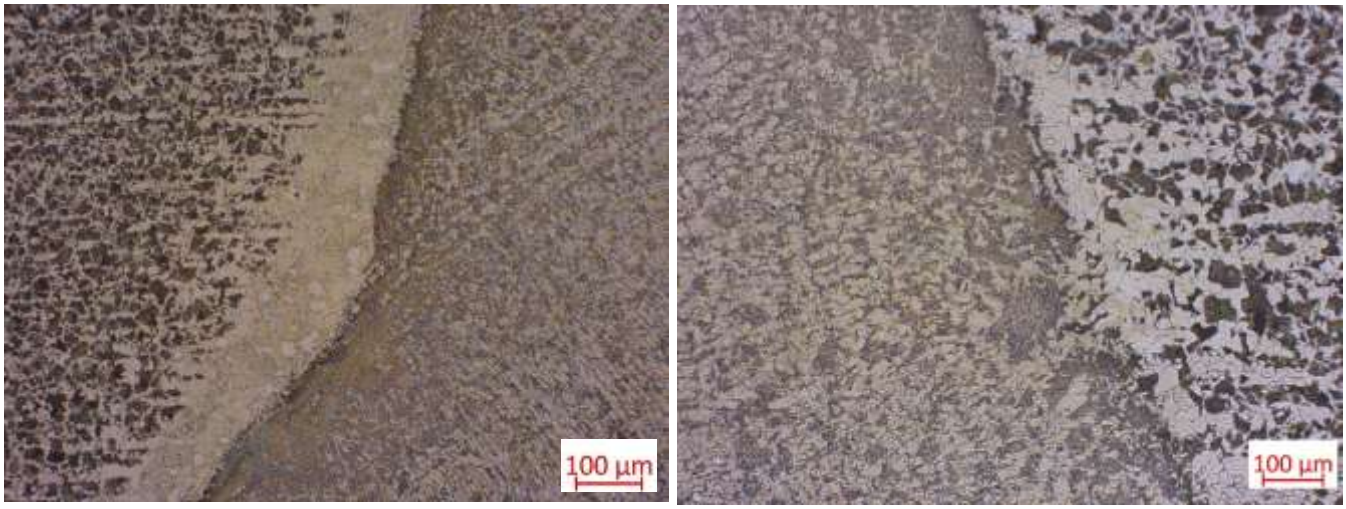

Figure 40 Optical microscope pictures of interface mixing zone MZ after annealing heat treatment

The microstructure evolution in the interface between the base metal and the fusion zone is represented in *Figure 40*. From the images it could be distinguished the base material microstructure, which is composed by proeutectoidic α-ferrite (white grains) and pearlite (dark grains). Successively, as the distance from the interface of the FZ and HAZ is reduced, the white α-ferrite grains quantity sensibly increases. Near the FZ-HAZ interface a white zone (carbon depleted zone) with 300 μm width is individuated. At the same time, a zone that is depleted from columnar solidification grains (carbon enriched zone), is detected in the fusion zone side. These zones were generated due to the carbon migration from the material with high C content, so the base metal (0,38 % C wt.), to the lower carbon content steel, the filler metal (0,08 % C wt.). This could be said because the number of white grains, so the one composed principally by α-ferrite, increases as the material is closer to the interface with the fusion zone. This happens despite to the pearlite grains, that are reduced since the carbon content is lower, so the generation of cementite lamellae was strongly prevented. The diffusion of alloying elements in the interface zone of dissimilar steels welding, is confirmed by the experimental studies of Yuh-Ying You et. al. [24],Peter Mayr et. al. [25], Wang et. al. [26].

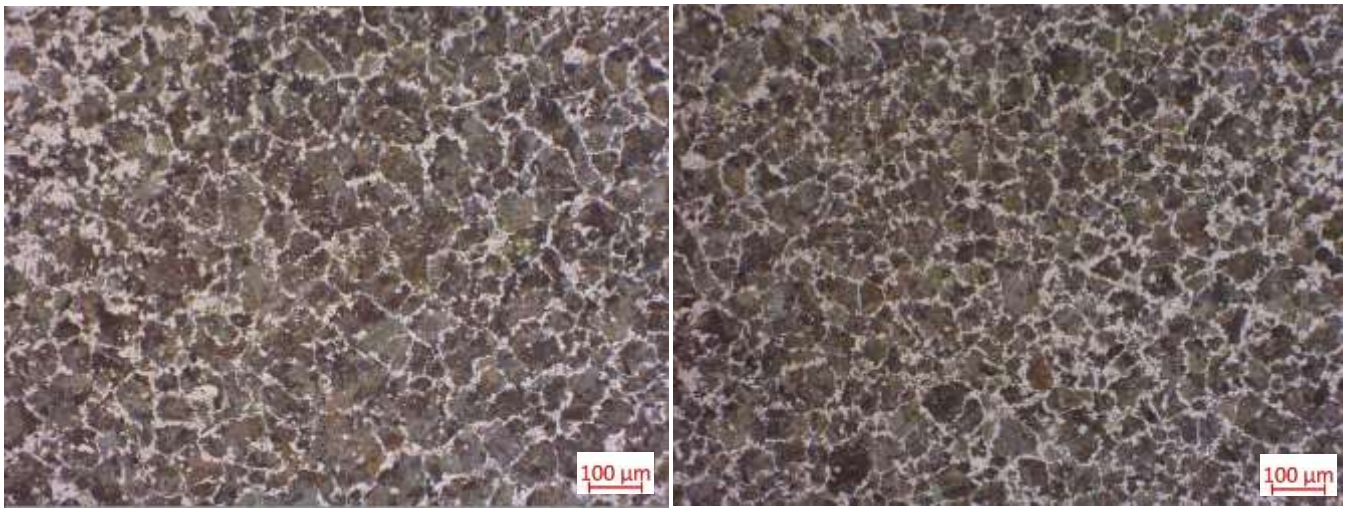

Figure 41 Optical microscope pictures of base material microstructure

In *Figure 41* the base material microstructure is represented. The annealing heat treatment generates the expected proeutectoidic α-ferrite and pearlitic microstructure.

Successively, the welded samples were subjected to quenching heat treatments. The specimens were first austenitized at 900°C for 5 minutes with the utilization of a heat furnace. Then, they were quenched in water at room temperature.

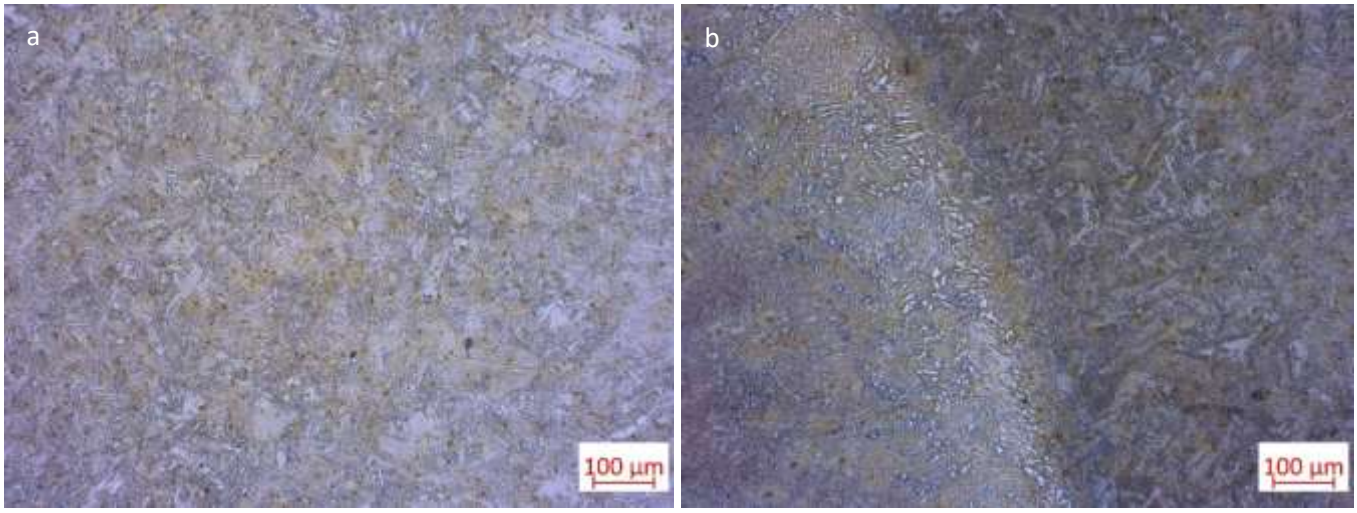

Figure 42 Optical microscope pictures of base material (a) and interface with fusion zone (b) of the quenched specimens

From *Figure 42* the microstructure of the base material obtained after the quenching heat treatment is represented in the image (a). This is composed by martensite, which forms easily thanks to the high cooling rate of the quenching in water and to the high hardenability of the bainitic steel. In the image (b) the interface mixing zone MZ is represented. In the fusion zone FZ side, acicular microstructure is individuated. Successively, the mixing zone is characterized by brighter grains that could be justified by the carbon depletion of the base metal.

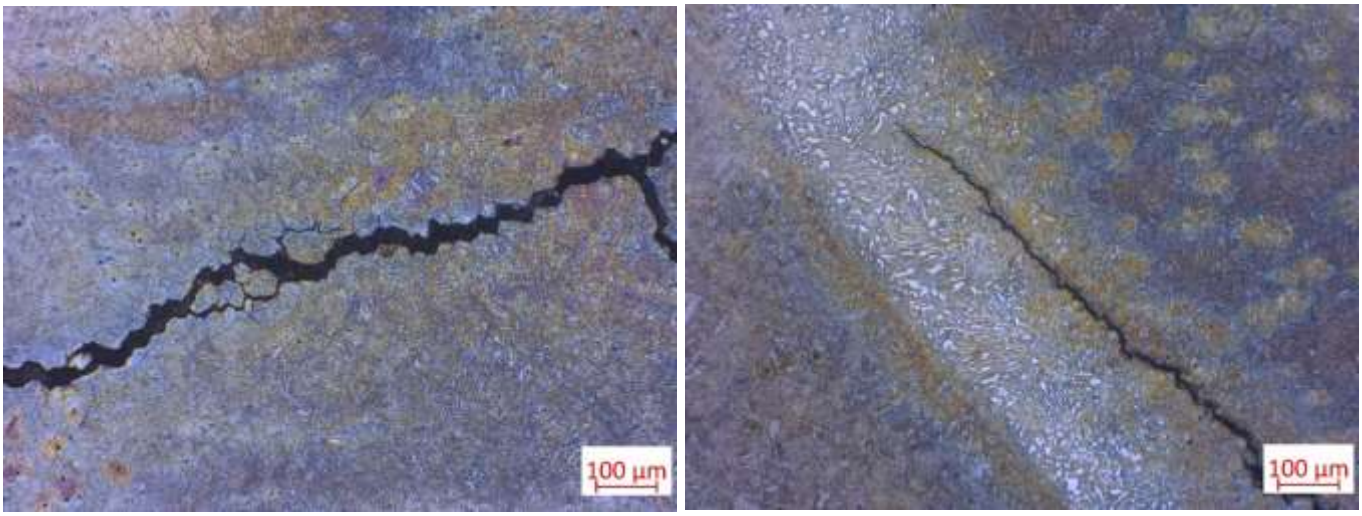

Figure 43 Optical microscope pictures of cracks generated in the quenched sample

As could be seen in *Figure 43* the quenching heat treatment caused the generation of cracks along the whole section of the sample. Hypotetically, the cracks starts from the carbon-depleted mixed zone MZ, as could be seen in the right picture, and extends in the base material of the specimen. The MZ is the weakest one in comparison with the whole heat affected zone, where defects and inclusions are present with higher probability.

6.7 Austempering heat treatment

The welded samples were treated with austempering heat treatment. This was conducted on specimens obtained from the longitudinal cut of the welded plates (as could be seen in *Figure 21*). In the first step of the heat treatment the welded steel was austenitized at 900°C for 5 minutes. Successively, it undergoes to an isothermal stage at 325°C for 3 hours, in order to obtain the complete bainitic transformation. The heat treatment was done with the utilization of two furnace: a tubular one, which was dedicated to the austenitization of the specimens, and another one that maintained the steel at the bainitic transformation temperature.

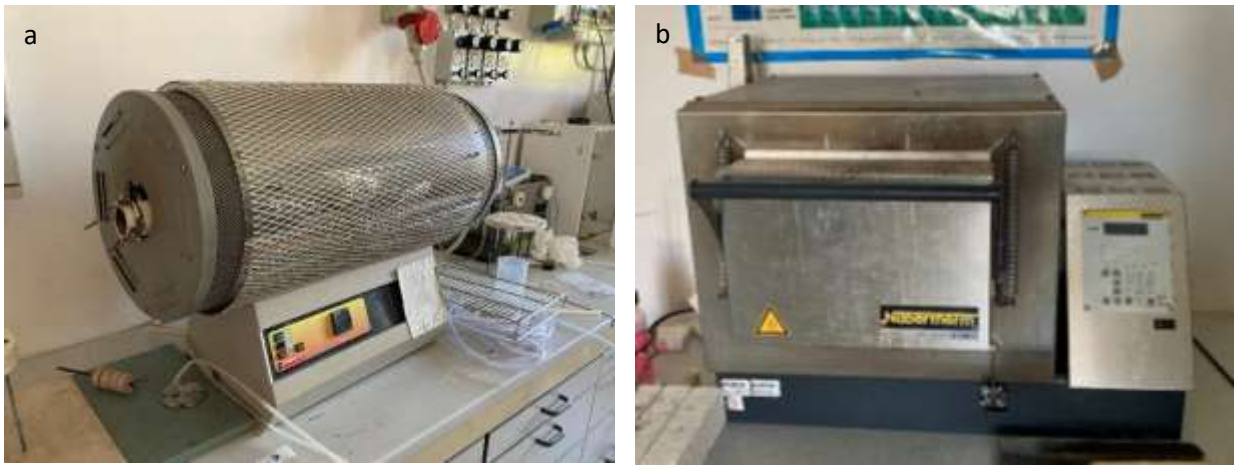

Figure 44 Tubular furnace (a) and isothermal stage heat treatment furnace (b)

The temperature during passage of the specimen between the austenitization and the isothermal furnace was controlled by a thermocouple. The samples were cooled in air at room temperature from 900°C to about 350°C since no microstructural transformation happens in this temperature range. This at least in the base material, where the presence of carbon and the other alloying elements shift the CCT transformation curves to higher time. Moreover, the martensite start M_s temperature for the bainitic steel is 242°C, so during the cooling stage of the heat treatment it will not be formed. On the other side, for the filler metal INEFIL NIMOCR the M_s obtained from the JMat Pro software calculations is 398°C. This means that in the fusion zone there could be the generation of martensite during the cooling stage between the two furnaces. The temperature of the isothermal stage was chosen as the one that corresponds to the bainitic transformation for the base metal.

The CCT and TTT curves are derived for the base material, bainitic TRIP steel, and the filler metal, INEFIL NIMOCR.

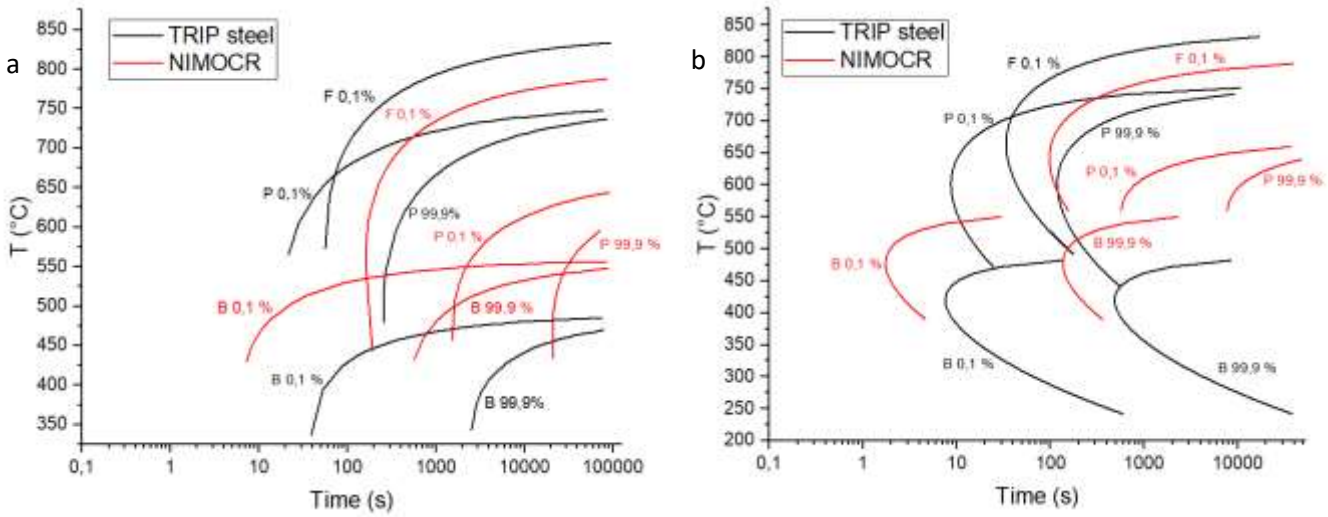

Figure 45 CCT (a) and TTT curves (b) of base material TRIP steel and INEFIL NIMOCR

The MIG welded specimens after being heat treated, were analyzed at the scanning electron microscope SEM. The metal surface was mounted in epoxy resin and prepared with grinding and polishing procedures. For highlight the nano-bainitic microstructure the Nital 2 etching attack was employed.

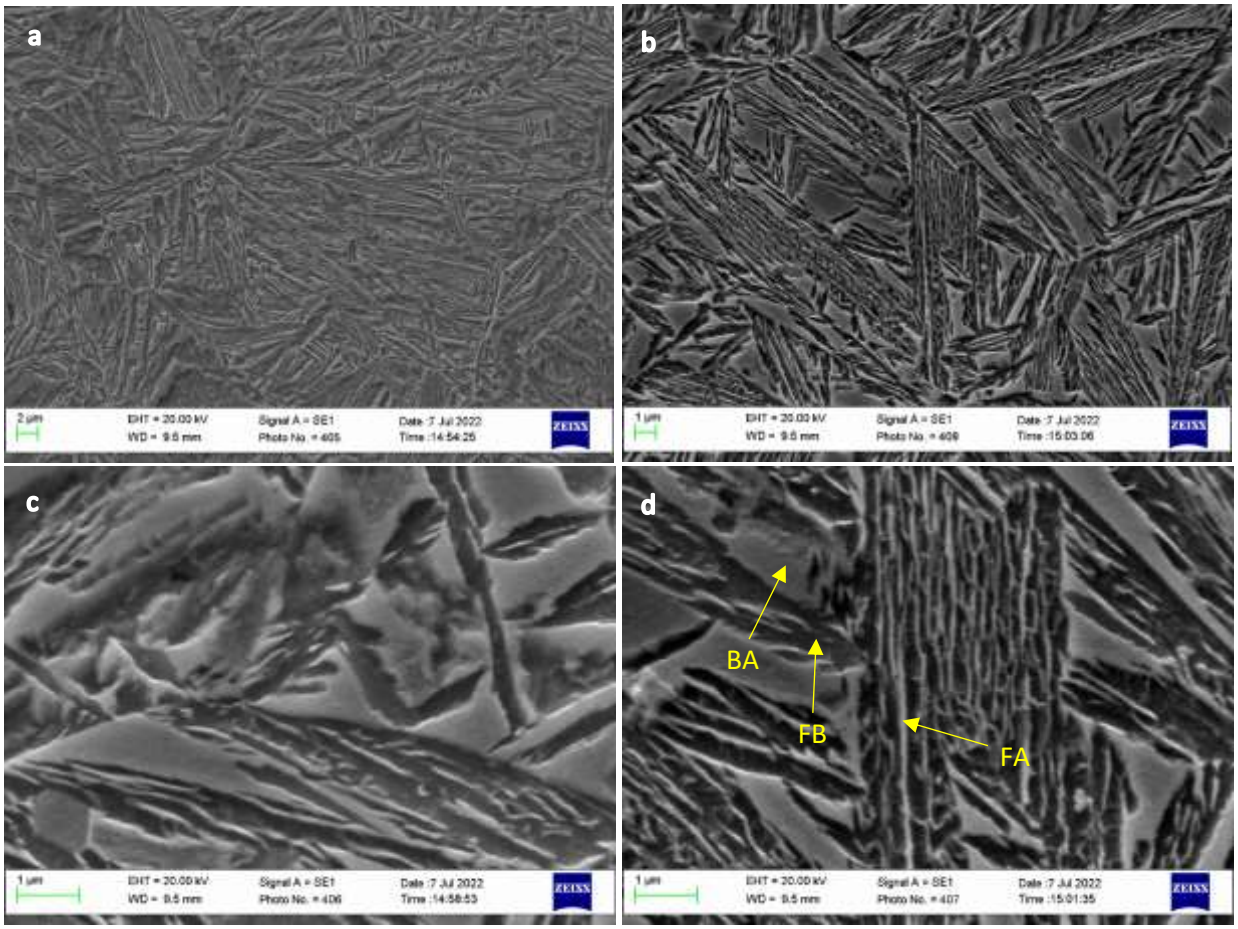

Figure 46 SEM pictures of base material after austempering heat treatment (BA blocky austenite, FB ferritic bainite, FA film austenite)

As could be seen from *Figure 46* the austempering heat treatment is considered satisfactory. In fact, the desired nano-bainitic microstructure was successfully obtained. In *Figure 46*, in particular in the higher magnification images (c) and (d), the blocky retained austenite grains, the film-like shape austenite, all surrounded by a free-carbide bainitic ferrite, could be recognized. The blocky austenite grains have a size of about 2-4 μm.

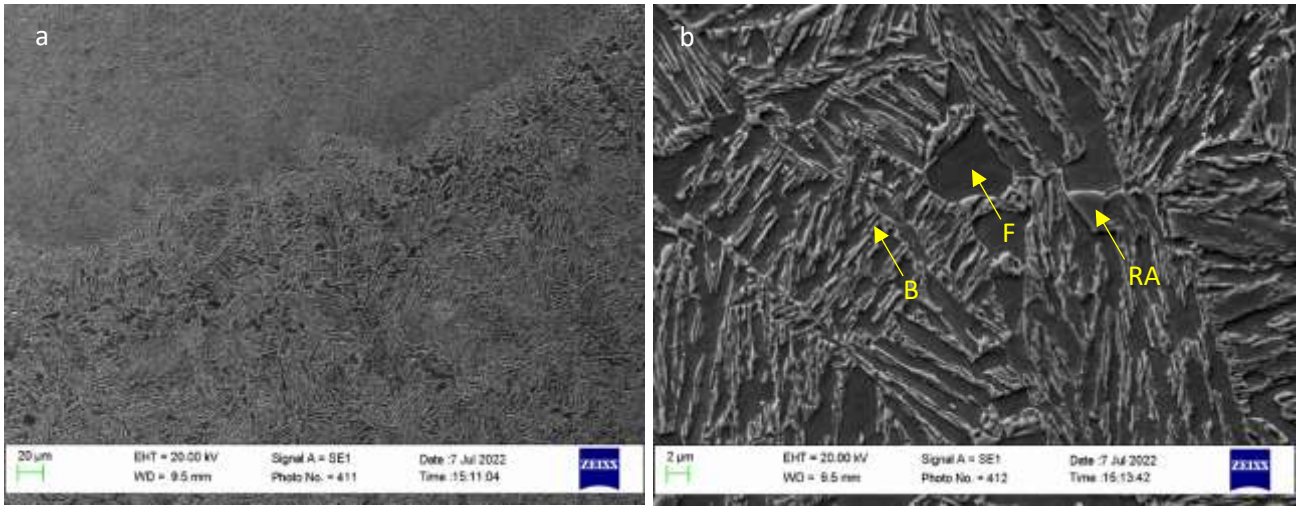

Figure 47 SEM pictures of interface zone at low magnification (a) and high magnification (b). F ferrite, B bainite, RA retained austenite

In *Figure 47* the microstructure of the mixing interface zone of the austempered welded specimens is represented. In picture (a) the IZ could be clearly seen, passing from the base material microstructure to the one of the fusion zone. From image (b) the difference from the base material bainitic microstructure could be clearly seen. In particular, due to the carbon depletion occurred during the welding procedure [24] [25], the nano-bainitic microstructure composed by distinguished blocky and film retained austenite, and ferritic bainite, is no more obtained. This is due to the very low stability of the retained austenite, caused by the reducing of the carbon content in this zone.

From *Figure 47*, if compared with the SEM picture of MIG specimen fusion zone as welded (*Figure 32*), it could be said that basically the microstructure of the filler metal doesn't change after the austempering heat treatment.

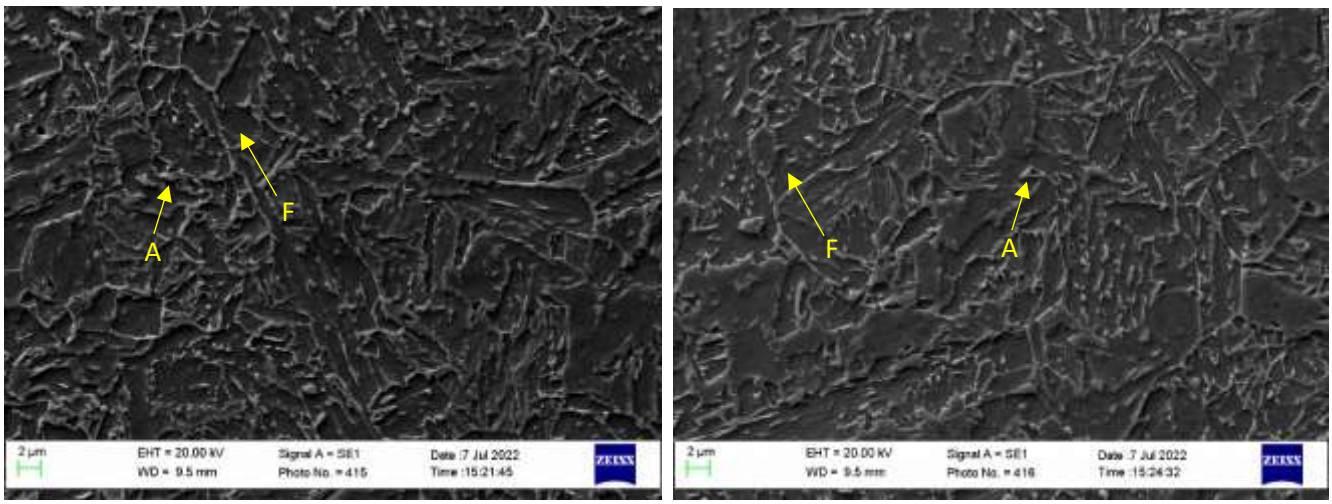

Figure 48 SEM pictures of austempered welded sample fusion zone. A austenite, F ferrite

Successively the hardness of the heat-treated samples was evaluated. The examination was conducted with Vickers micro-hardness test.

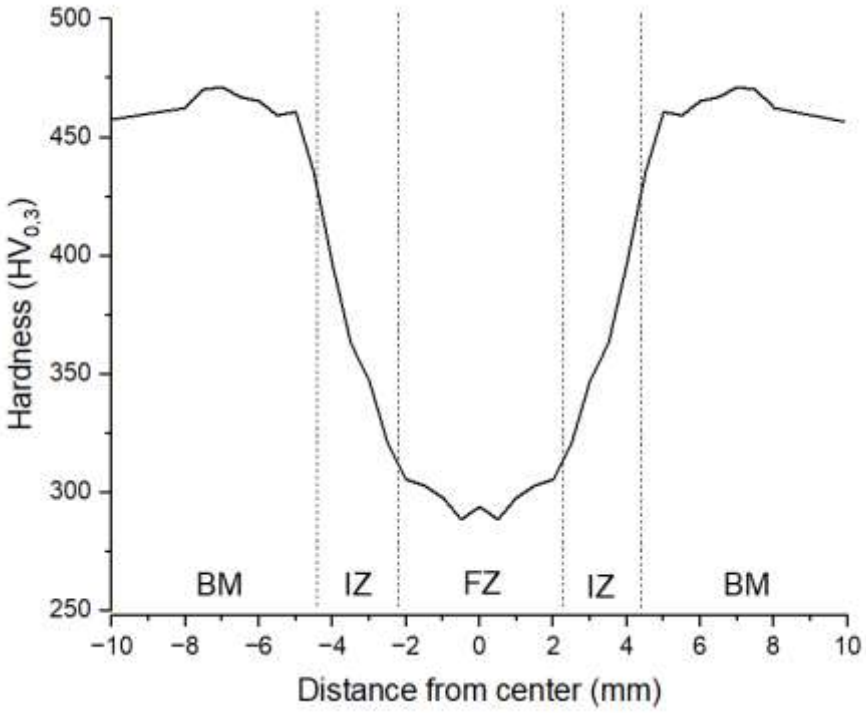

Figure 49 Results of Vickers micro-hardness tests on MIG welded sample austempered

The indentations were taken at the same height of the section as the MIG welded sample in the 'as weld' condition (see *Figure 35*). Three different zones could be recognized in the MIG welded sample austempered: the fusion zone FZ, the interface zone IZ, and the base material BM. The fusion zone hardness results, as expected, unaltered from the austempering heat treatment, maintaining a value of 290-300 $HV_{0,3}$. After the fusion zone, the hardness increases in the interface zone IZ. This for about

2 mm, till reaching the base material BM where the hardness stabilizes at 450-470 $HV_{0,3}$. This value is the one expected for the free-carbide nano-bainitic microstructure obtained after the austempering heat treatment, like the one discovered by Franceschi et. al. [27].

In *Figure 50*, the comparison between the hardness test values obtained for MIG welded samples in the 'as weld' and 'austempered' conditions are represented. From the chart it could be noted the difference between the hardness of the base material in the two conditions: in the 'as weld' sample it is higher due to the presence of a martensitic microstructure. The width of the hardness plot of the fusion zone is slightly decrease in the 'austempered' specimen. This is probably due to the homogenization of the microstructure in the heat affected zone which influence the hardness of the FZ near the interface with the base material.

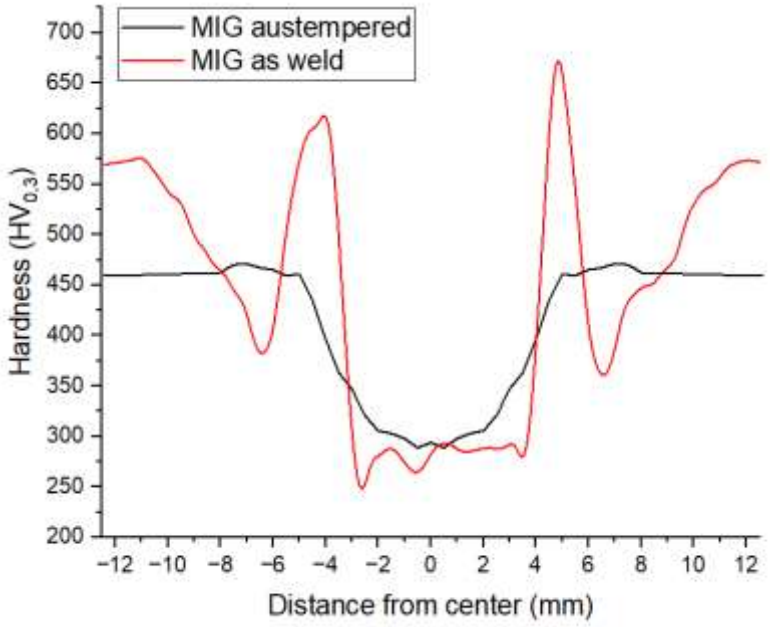

Figure 50 Hardness test results of MIG samples in 'as weld' and 'austempered' condition

The MIG welded sample austempered microstructure of the different zones was examined also with XRD for phase identification and quantification analysis. Two zones were evaluated: the fusion zone and the base material zone.

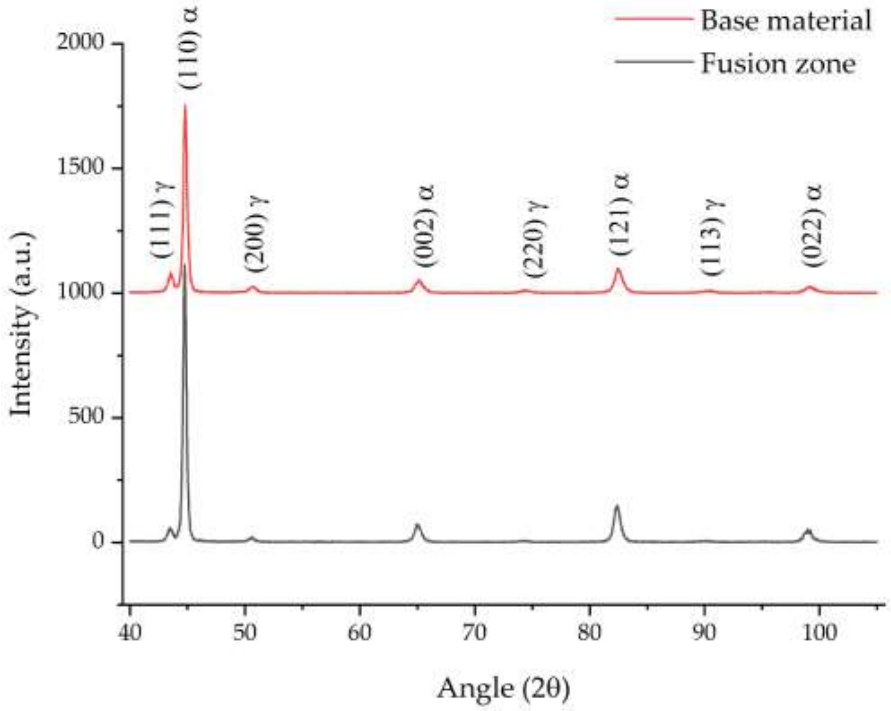

Figure 51 XRD pattern resulted for phase composition analysis of MIG sample 'austempered'

Zone	V_γ	X_γ	V_α	X_α	$V_{\alpha'}$	$X_{\alpha'}$	$V_{\alpha b}$	$X_{\alpha b}$
Fusion zone	6.38	1.20	86.70	0.03	6.90	0.54	-	-
Base material	24.98	1.02	-	-	-	-	75.02	0.17

Table 11 Results of XRD phase quantification analysis of MIG sample 'austempered'. V_γ, volume fraction of retained austenite, X_γ, carbon content wt. % in retained austenite, V_α, volume fraction of α-ferrite, X_α, carbon content wt. % in retained austenite, $V_{\alpha'}$, volume fraction of martensite, $X_{\alpha'}$, carbon content wt. % in martensite, $V_{\alpha b}$, volume fraction of bainitic α-ferrite, $X_{\alpha b}$, carbon content wt. % in bainitic α-ferrite.

The fusion zone composition results with a low quantity of austenite, the principal phase that characterize the filler metal after the austempering heat treatment is α-ferrite. This is in concordance with the very low carbon content of the filler metal. In particular, since the Ms is individuated at 398°C, the material when is subjected to the isothermal stage at 325°C generates the martensitic microstructure, which content is low.

The base material microstructure is characterized by a higher quantity of austenite, which is justified by the generation of blocky islands and films of retained austenite after austempering heat treatment. The principal phase that characterizes the microstructure of the base material is the bainitic ferrite. In particular, the bainitic ferrite is confirmed as carbon super-saturated with a carbon content equal to 0,17 in agreement with F.G. Caballero et. al. [28].

From these results, the generation of the nano-bainitic microstructure after the austempering heat treatment is confirmed.

The MIG sample ‘austempered’ mechanical properties have been tested with tensile testing machine. The goal of the test conducted was to determine the principal mechanical characteristics of the welded sample: yield strength, ultimate tensile strength.

Yield Strength σ_y [MPa]	UTS σ_{max} [MPa]
783±19	860±0.74

Table 12 Tensile test results of MIG sample ‘austempered’

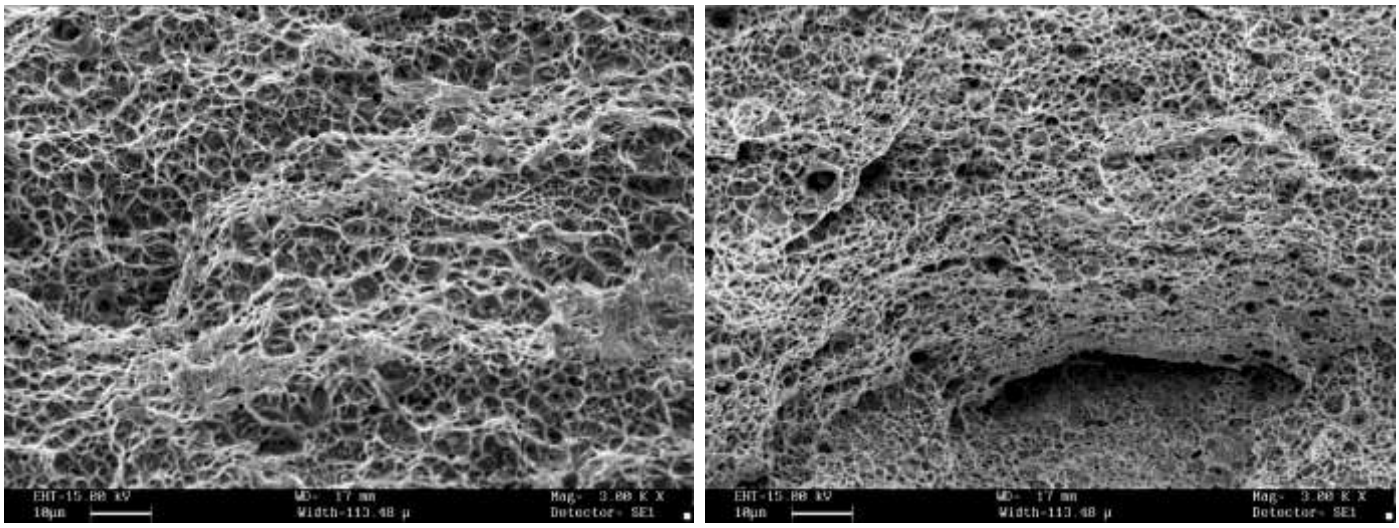

Figure 52 SEM picture of MIG welded sample ‘austempered’ fracture surface

The welded sample under tensile test failed in the fusion zone. The fracture, as could be seen from the surface in *Figure 52*, due to the presence of dimples, is ductile.

6.8 Tensile tests

The preliminary evaluation of the welded sample mechanical properties is important for the assessment of the weldability of the bainitic steel. The MIG welded sample in the ‘as weld’ condition was tested with tensile machine testing.

Yield Strength σ_y [MPa]	UTS σ_{max} [MPa]
884	992

Table 13 Tensile test results of MIG sample ‘as weld’

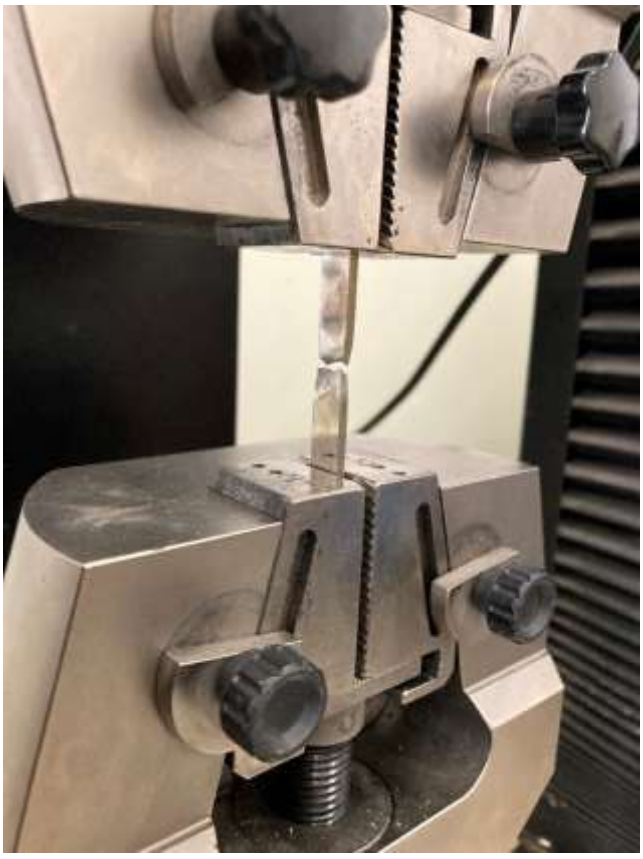

Figure 53 Welded sample fractured

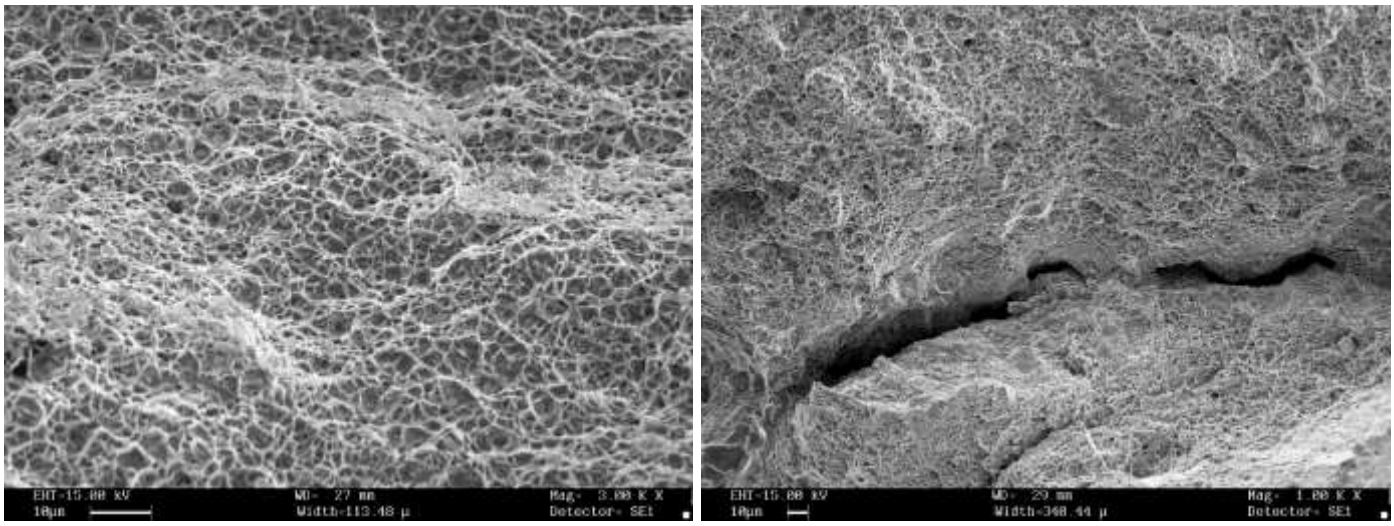

Figure 54 SEM picture of MIG welded sample 'as weld' fracture surface

The sample failure was verified in the fusion zone, so the one corresponding to the filler metal INEFIL NIMOCR. From *Figure 54* it could be stated that the fracture of the MIG welded sample 'as weld' is ductile. This is confirmed by the presence of dimples on the fracture surface.

7. MMA (SMAW) process results

7.1 Visualization and penetrating liquids

With the Manual Metal Arc welding process, where the consumable coated electrode is employed, promising results are obtained. The weld bead in this case was different from the one of the MIG process: the path of the electrode is much clearer, with the evidence of the different passes (the last two could be clearly distinguished between each other, as could be seen in *Figure 55*). The weld joint surface is rougher than the one with MIG procedure, this is due to the wavy path of the electrode, employed to achieve a better stability of the arc.

Figure 55 Weld bead obtained with MMA process

It could be stated that the quantity of sputter produced by the MMA is slighlty less than the MIG welding process. In the case of MMA, instead of the production of the glassy layer along the weld bead as in the MIG procedure, there is the evidence of a rust layer in the center of the weld bead in correspondance of the interface between the two last passes. Probably in this case the glassy vein along the weld bead hasn't been formed due to the remove of the slag at every pass, leaving very low quantities of external compounds on the metal surface. In this welding process, also a final "recovery" pass in the back of the welded plates is conducted. This is done to definetly join the two plates, in order to derive efficiently the samples for the experimental analysis.

The analysis of the porosities and macro defects on the weld bead surface is conducted with the penetrating liquids.

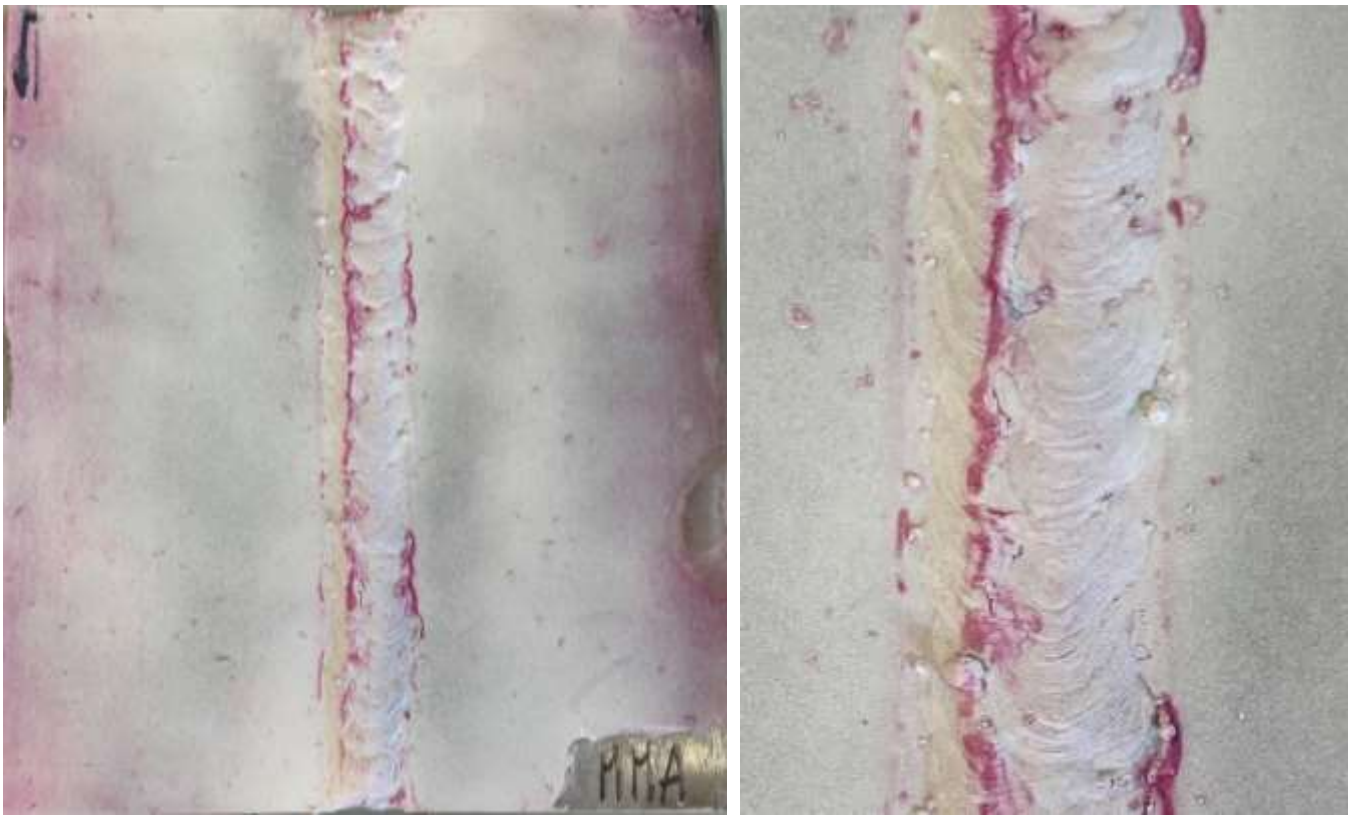

Figure 56 Results of penetrating liquids on MMA weld bead

From the evaluation of the reaction between the white revealing and the red penetrating liquid, it could be stated that also in the case of MMA there wasn't the generation of cracks or macro defects on the weld bead surface. In *Figure 56* the red areas highlighted are the one corresponding to the rust layer on the weld bead surface and base, which aren't considered to be defects.

So after this initial analysis, mind also that the welding process results with no cracking or ruptures while it is carried out, it could be said that also the Manual Metal Arc welding process is feasible.

7.2 Residual stresses

The analysis of the residual stresses on the two plates welded together with MMA process was conducted as the one for the MIG welding procedure. The points which were evaluated were in the same position as the other welding method, which could be seen in the *Figure 29*. The results of the XRD analysis of the MMA are reported in the following table.

POINT	Stress σ_φ in X plane [MPa]	Stress σ_φ in Y plane [MPa]
0	-3	489
1	67	502
2	-306	-200
3	-279	79
4	-309	-111
5	-446	-300
6	-581	-492
7	23	50
8	-73	-63
9	-251	-303

Table 14 Results of residual stresses analysis of MMA welded plates

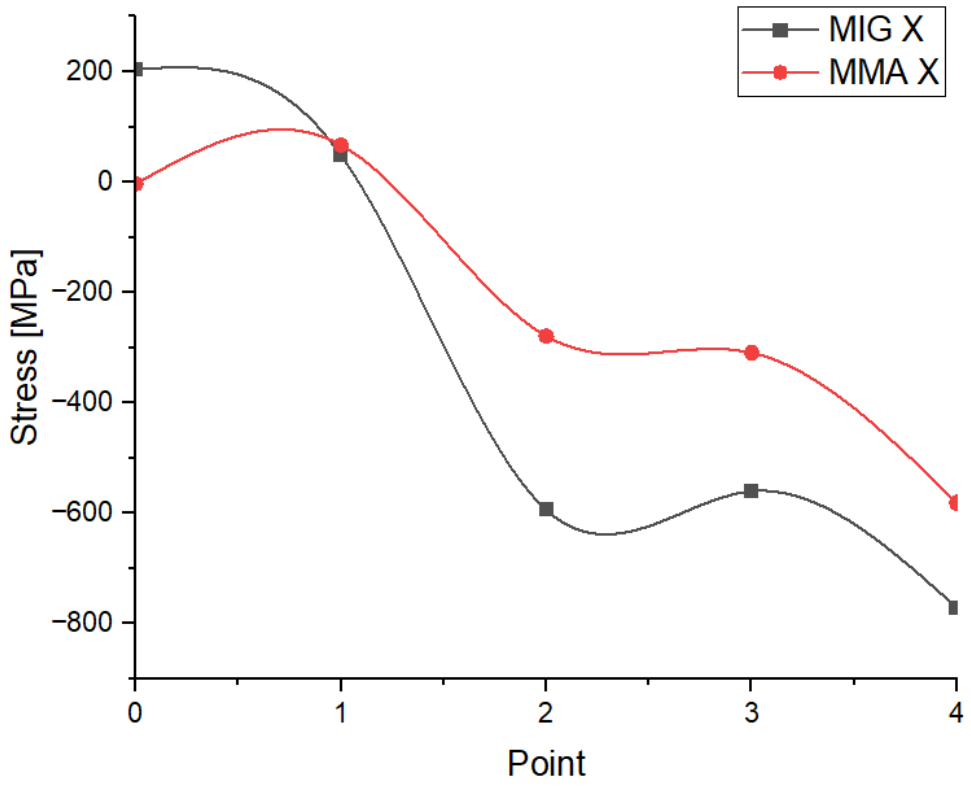

Figure 57 Representation of residual stresses distribution on MIG and MMA welded plates in X plane

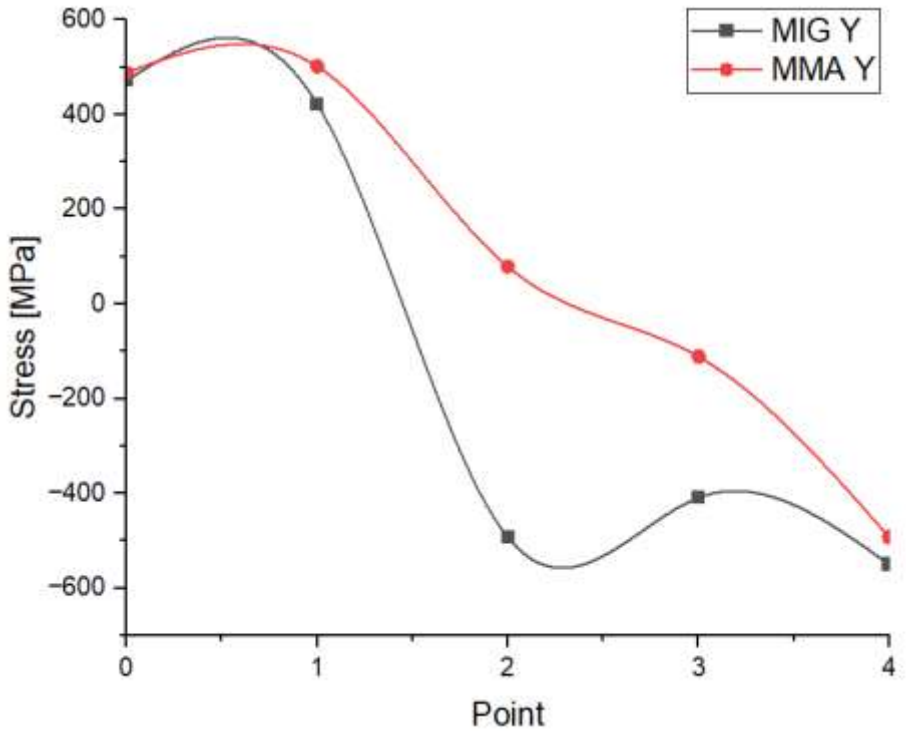

Figure 58 Representation of residual stresses distribution on MIG and MMA welded plates in Y plane

As could be noted in *Table 11* there is a distinction between the stresses analyzed in the X plane, longitudinal to the welding direction, and Y plane, parallel to the welding direction. The stresses in the X plane are distributed in the same way as the ones of the MIG welded plates, basically the weld bead is under slight tensile stress and the base material is progressively under compression as it moves away from the weld bead. The points evaluated on the top and on the base of the weld bead (0 and 1) are slightly under tensile stress state, which could be considered unstressed. The next points are under compressive stress, which increase from the weld bead to the base material side. This could be noticed also in the Y direction of XRD sampling. Also in the case of MMA, welded plates the points 0 and 1, when analyzed in the Y plane, show a marked tensile stress situation. This is due to the welding direction that influence the residual stresses present on these sections.

The residual stresses obtained in the case of MMA welding process are characterized by a lower compressive state than the MIG one (as could be noted from the *Figure 57 & 58*), this means an overall tensile stress induced by the welding process which is higher in comparison to the MIG welding procedure.

7.3 Optical microscopy and SEM

The same optical analysis was conducted also for the metallic plates welded with Manual Metal Arc process. Also in this case, the sample was etched with Klemm's I chemical attack, which permitted to reveal clearly all the different parts of the heat affected zone.

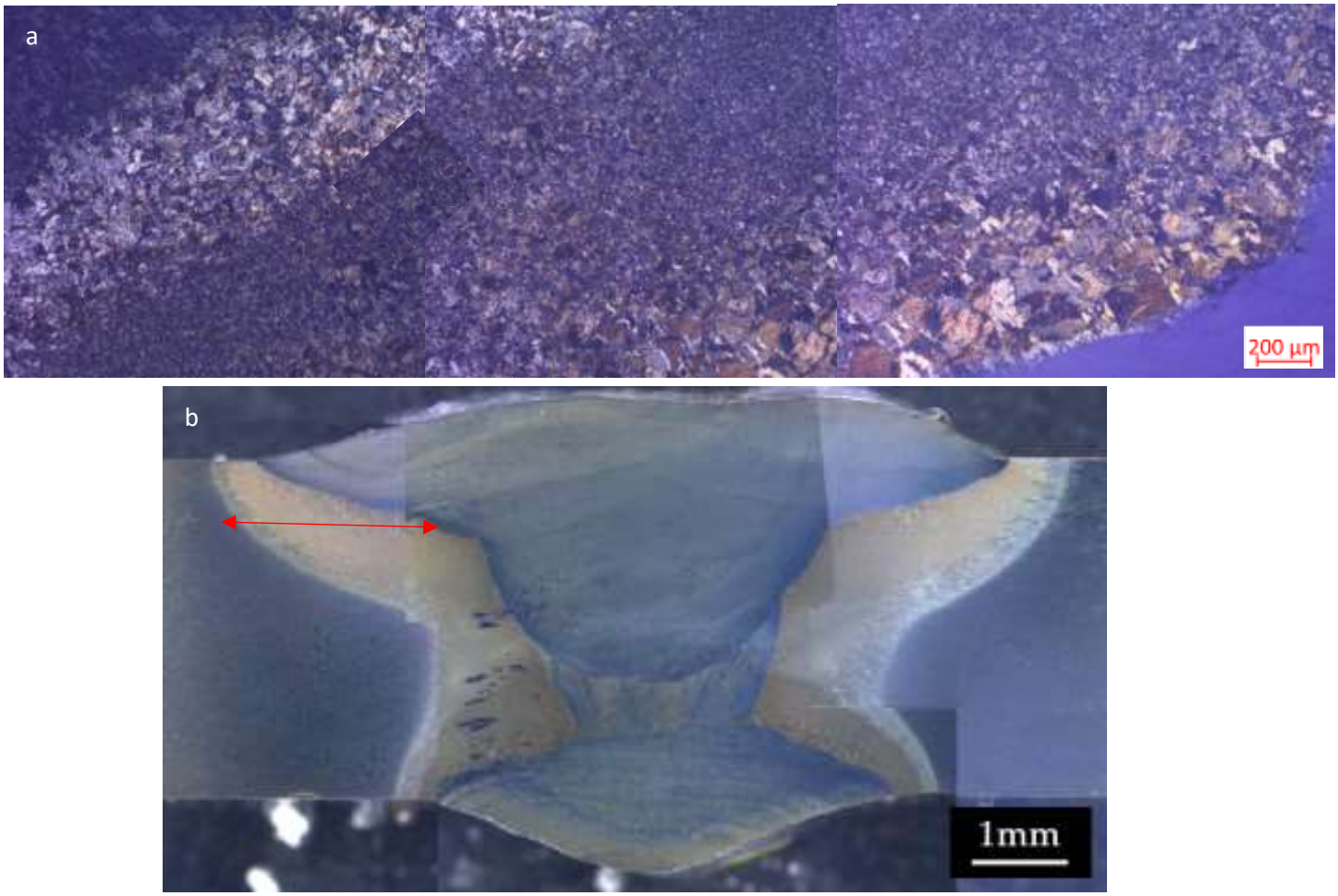

Figure 59 Optical microscope picture of welded sample heat affected zone (a) and weld bead section (b)

From *Figure 59* it could be seen that basically the same microstructure alteration of MIG is obtained with MMA welding process. It could be distinguished the fusion zone (in light blue on the right), the coarsened mixing zone of base material and filler metal, the refined zone in the center of the HAZ, the low heat affected zone that is slighted coarsened, and finally the base material microstructure. These optical microscope pictures were taken in the zone where the hardness tests were conducted, at the same height as in the MIG samples. It could be stated that in the case of MMA welding process the microstructural alteration is more horizontally extended in comparison with the MIG one.

The analysis of the MMA welded plates microstructure was conducted also at SEM microscopy.

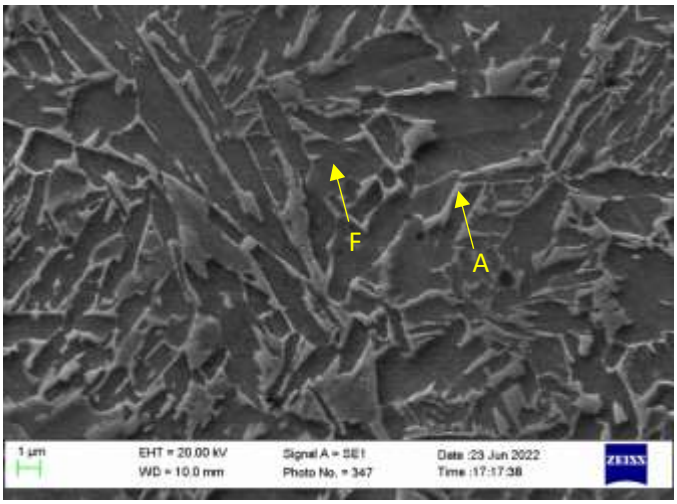

Figure 60 SEM pictures of fusion zone. F ferrite, A austenite

The microstructure obtained in the fusion zone of the MMA welded sample is composed mainly by a ferritic matrix with austenite islands.

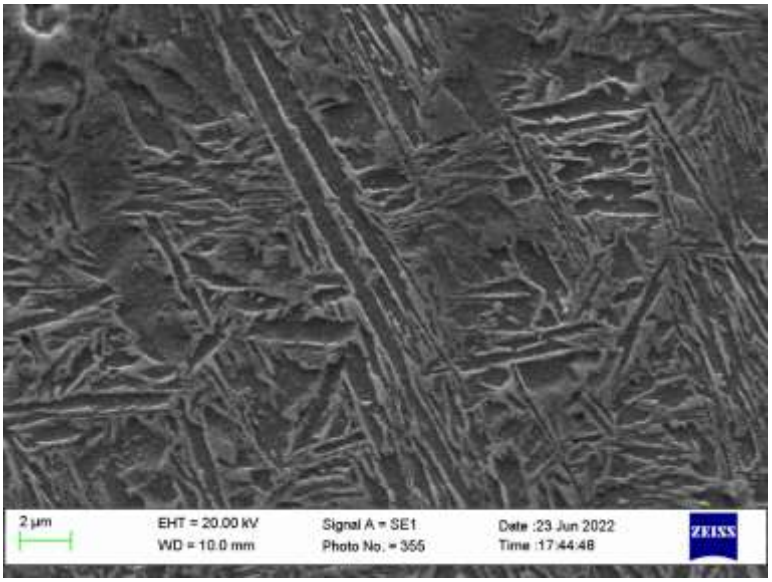

Figure 61 SEM picture of heat affected zone (HAZ) microstructure

From *Figure 61* it could be stated that also in the case of MMA welded sample an alteration of the martensitic microstructure is obtained. The SEM picture of base material obtained in the MMA is the same as the MIG one.

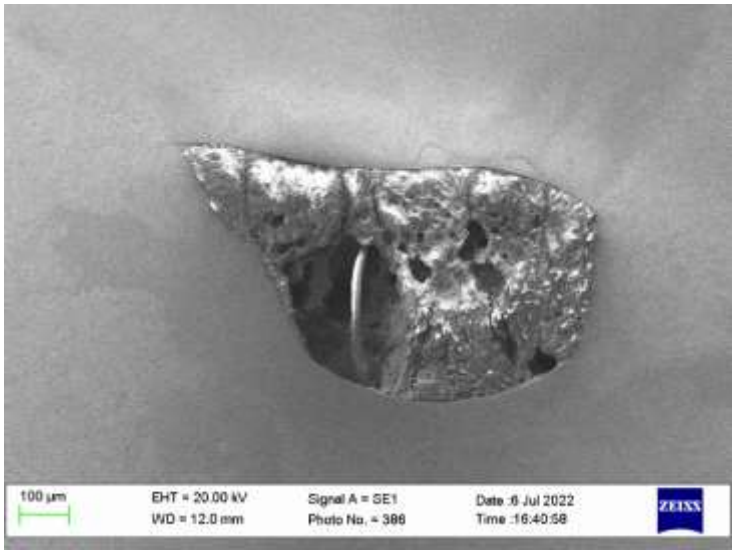

Figure 62 Welding defects of MMA sample in the fusion zone

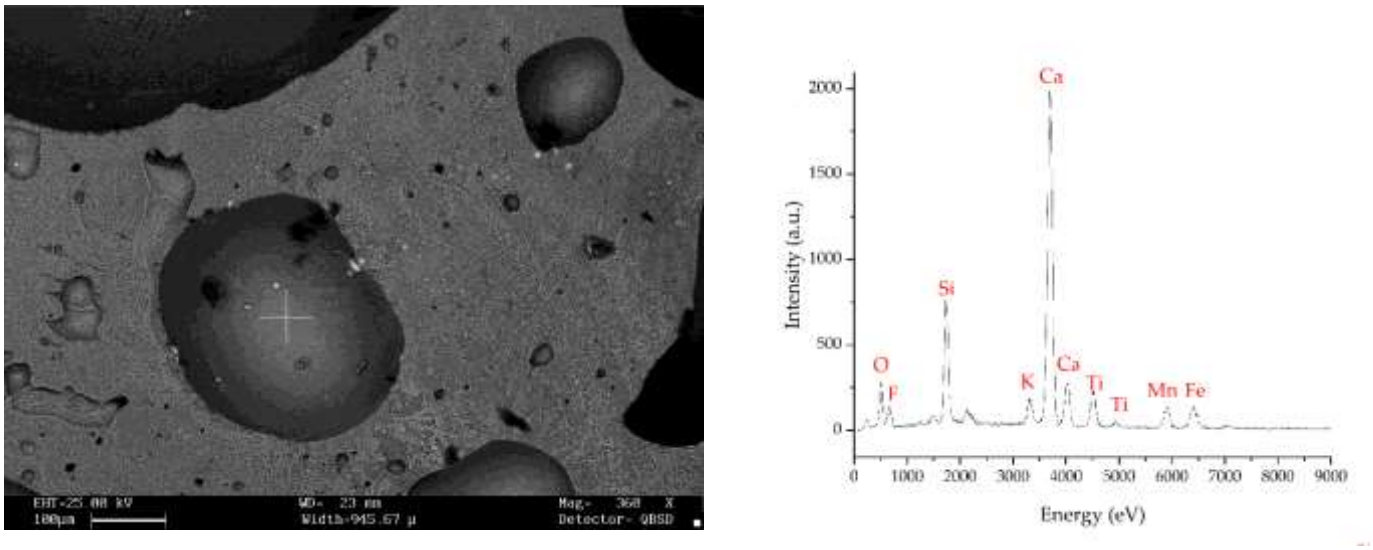

Figure 63 SEM picture of MMA slag (a) EDS analysis of slag general composition (b)

The slag generated from the MMA welding process is analyzed at SEM and EDS. The elements that characterize the slag composition are Ca, Si, F and O. These are in concordance with the chemical composition of the basic electrode employed.

7.4 Hardness

The material hardness examination was conducted with Vickers micro-hardness tests. In the case of MMA welded plates, the steels are tested both horizontally and in the vertical direction of the weld bead, as in the MIG sample. The two different paths could be seen in *Figure 64*. Also in the case of MMA, the longitudinal seam was taken at about 2 mm from the top of the weld bead, in order to be efficiently compared with the other welding processes.

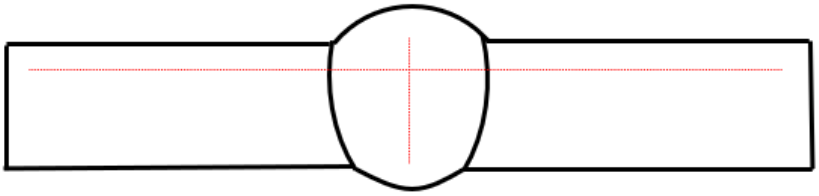

Figure 64 Hardness tests imprints horizontal path (Path 1), and vertical path (Path 2)

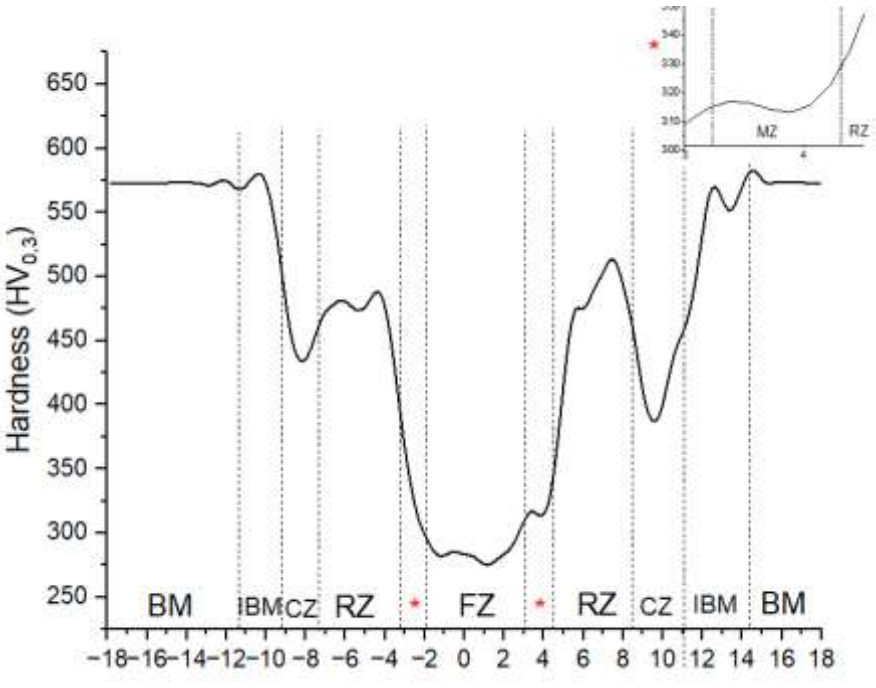

Figure 65 Material hardness in function of the distance from the center of the fusion zone (Path 1)

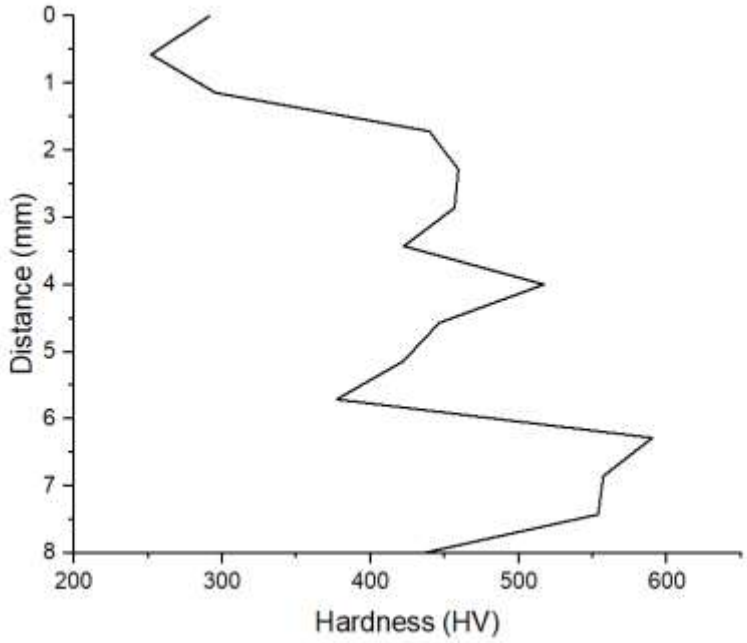

Figure 66 Material hardness in function of the distance from the top of the fusion zone (Path 2)

From *Figure 65* the hardness values resulted from the tests follow a similar development as the ones of the MIG welded sample. It could be seen that the material hardness in the fusion zone FZ, so the one of the INE 80B filler metal, corresponds to the values of 290-300 $HV_{0,3}$. This value confirms that also in this case no marked quantity of martensitic microstructure is generated in this zone. In the mixed zone MZ the materials hardness slightly increases up to 375 $HV_{0,3}$. The steel plates, due to the welding process, undergo to several heat cycles that cause the generation of the refined zone RZ. In this the hardness resulted in a wide peak of 480 $HV_{0,3}$. Successively, the hardness values are reduced to 420 $HV_{0,3}$ in the coarsened zone CZ. The influenced base material IBM zone denote an increase in the hardness resulted, till the stabilization to the value of 575-580 $HV_{0,3}$, which is conducible to the one of the unaltered martensitic base material BM microstructure.

In *Figure 66* the hardness examination results in the vertical direction from the top of the weld bead are represented. In this case, there is a strong increase in the hardness passing from the top to the bottom of the bead. This could be probably reconducted to the high number of passes that were employed in the MMA welding process, which markedly altered the microstructure of the filler metal when was deposited.

From the hardness tests results it could be stated that the wideness of the heat affected zone is about 13-14 mm in each side, from the end of the fusion zone.

7.5 XRD for phase identification and quantification

The MMA welded samples obtained microstructure was analyzed in two different zones, weld bead and base material.

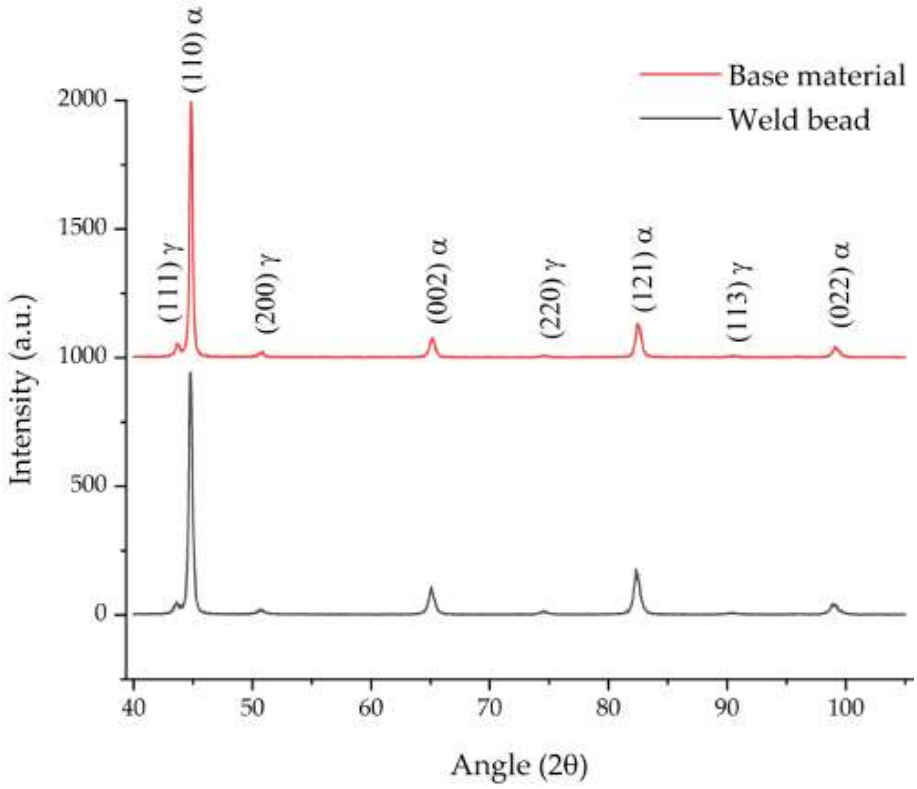

Figure 67 XRD pattern resulted for phase identification of MMA sample 'as weld'

Zone	V_γ	X_γ	V_α	X_α	$V_{\alpha'}$	$X_{\alpha'}$
Weld bead	5.3	1.21	87.07	0.03	7.61	0.17
Base material	5.50	0.58	-	-	94.5	0.24

Table 15 Results of XRD phase quantification of MMA sample 'as weld'. V_γ, volume fraction of retained austenite, X_γ, carbon content wt. % in retained austenite, V_α, volume fraction of α-ferrite, X_α, carbon content wt. % in retained austenite, $V_{\alpha'}$, volume fraction of martensite, $X_{\alpha'}$, carbon content wt. % in martensite

The weld bead microstructure composition results with low amount of austenite and martensite. The main phase is represented by α-ferrite.

The MMA welded sample ‘austempered’ mechanical properties, such as yield strength, ultimate tensile strength, were examined with tensile tests.

Yield Strength σ_y [MPa]	UTS σ_{max} [MPa]
922±35	1145±18

Table 16 Tensile test results of MMA welded sample ‘austempered’

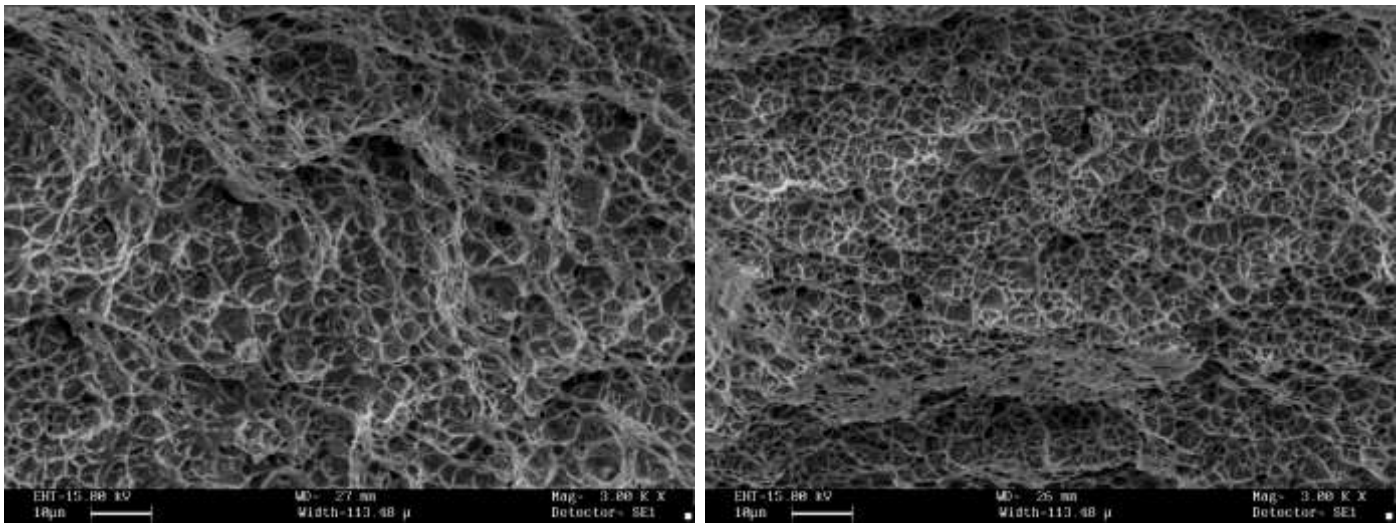

Figure 68 SEM picture of MMA welded sample ‘austempered’ fracture surface

The welded sample tested failed in the central fusion zone, so the one corresponding to the INE 80B filler metal. The fracture surface shows the presence of dimples, this confirms that the fracture is ductile.

7.8 Tensile tests

The mechanical properties of MMA welded sample in the ‘as weld’ condition have been evaluated with tensile tests.

Yield Strength σ_y [MPa]	UTS σ_{max} [MPa]
1074	1252

Table 127 Tensile test results of MMA ‘as weld’ sample

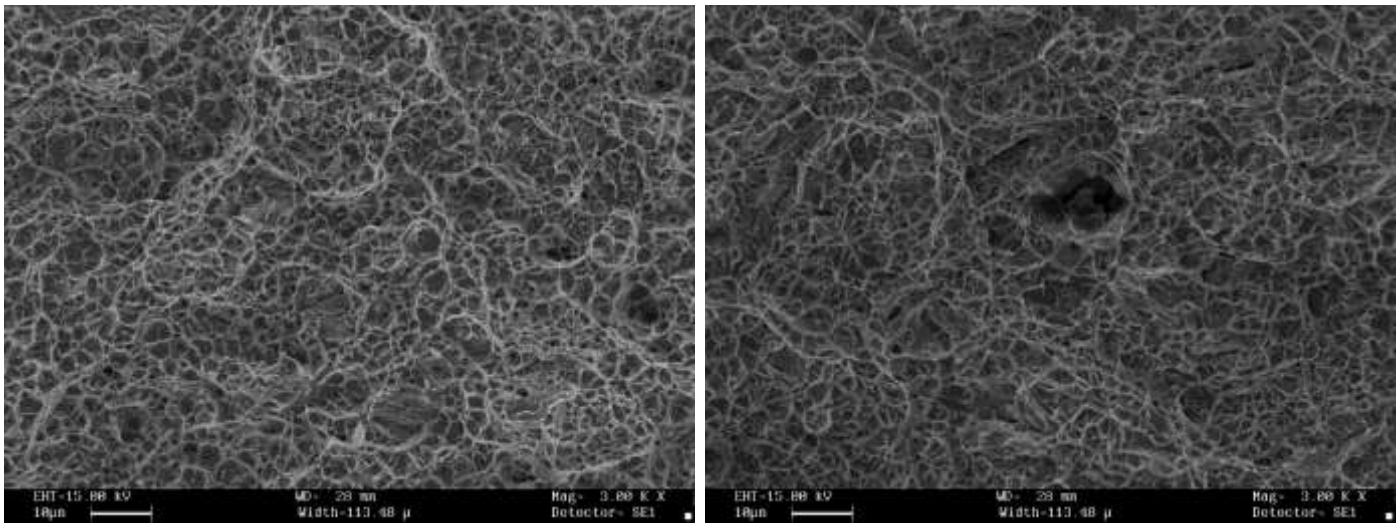

Figure 69 SEM picture of MMA ‘austempered’ sample fracture surface

The MMA ‘as weld’ sample failed in the central fusion zone. The fracture surface is ductile, this is confirmed by the presence of dimples, as could be seen in *Figure 69*.

Sample	Yield strength σ_y [MPa]	Ultimate tensile strength σ_{max} [MPa]
MIG-austempered	783	860
MIG-as weld	884	992
MMA-austempered	1074	1252
MMA-as weld	922	1145

Table 18 Resume of tensile tests results of MIG and MMA welded sample in 'as weld' and 'austempered' condition

The preliminary tensile tests results show that in general the MMA welded samples are characterized by the highest mechanical properties. The MMA 'austempered' sample reported higher yield strength and UTS in comparison with the 'as weld'sample. In the case of MIG samples, the 'as weld' shows better mechanical properties if compared with the 'austempered' one.

The better mechanical properties obtained in the MMA welded sample could be justified by the higher heat input that cause wider extension of the material alteration. In particular, the carbon migration in the fusion zone could be enhanced, which led to an increase in the strength of this zone [26] where all the welded samples are fractured. However, a deeper investigation must be conducted to better assess the mechanical behavior of the different welded samples.

7.6 Annealing and quenching heat treatments

The same annealing heat treatment of the MIG welded sample was conducted for the MMA welded plates. The specimen was austenitized at 900°C for 5 minutes and then quenched in water at room temperature 25°C.

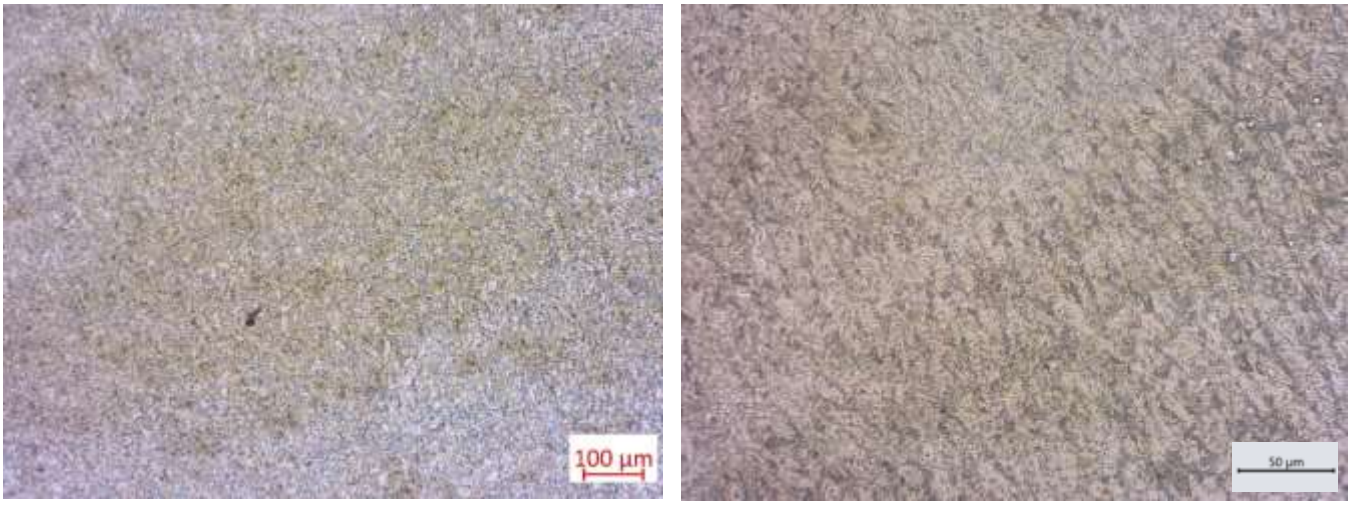

Figure 70 Optical pictures of annealed MMA welded sample fusion zone FZ

The microstructure obtained after the annealing heat treatment was analyzed at the optical microscope. In *Figure 70* the FZ microstructure is represented, with the α-ferrite as the predominant phase.

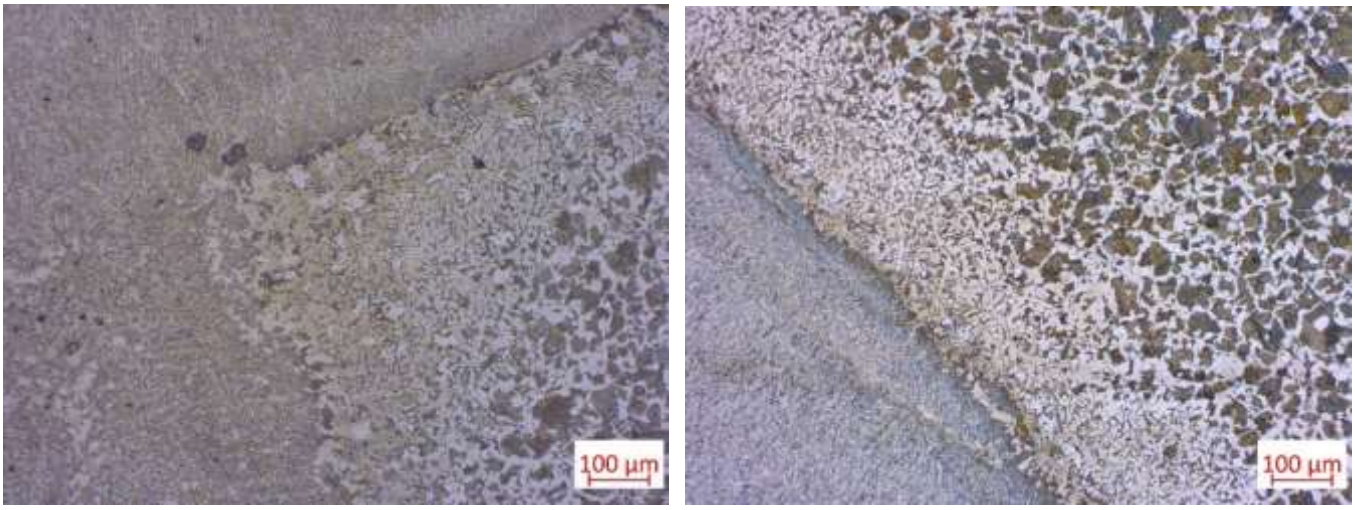

Figure 71 Optical pictures of the mixing zone MZ of annealed sample

The pictures in *Figure 71* represents the interface mixing zone. The carbon depletion could be clearly seen due to the prevailing of the ferritic grains in the interface area with the fusion zone [24] [25] [27].

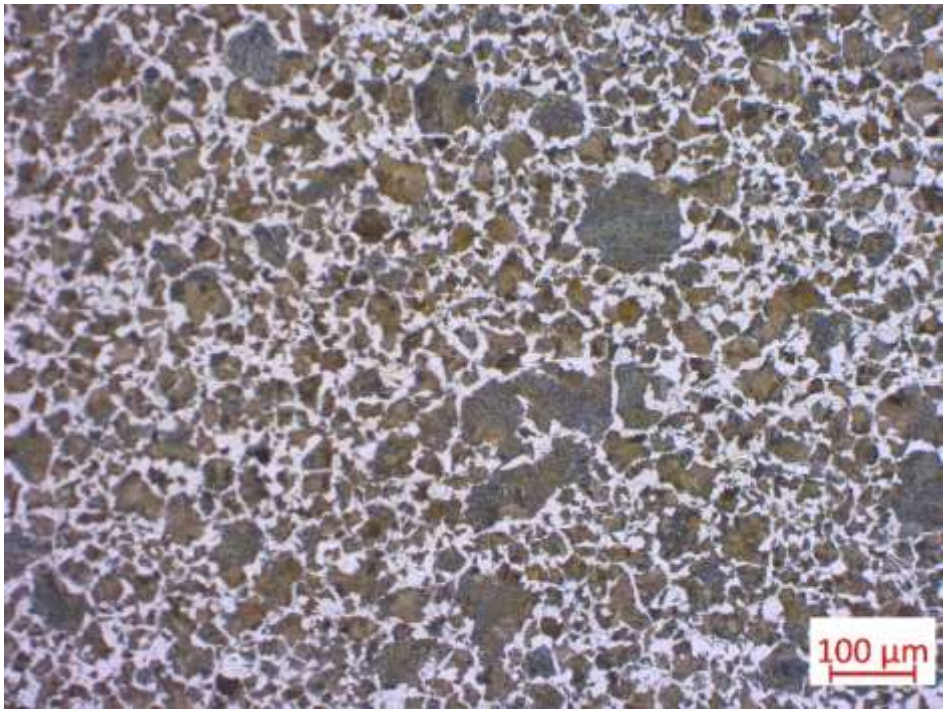

Figure 72 Optical pictures of annealed sample base material miscrostructure

The annealing heat treatment generates in the base material the as expected pearlitic and proeutectodic microstructure.

Figure 73 Pore defect detected in the fusion zone of annealed sample

The welded sample was subjected to quenching heat treatment. The material was austenitized to 900°C for 5 minutes, and then quenched in water at room temperature 25°C. The microstructure obtained, as could be seen in the pictures below, is mainly martensitic. This is expected in the base material: the self-hardenability lets the generation of martensite. In the filler metal fusion zone, there could be generation of martensite due to the very low content of carbon (that results in a Ms martensite start temperature well above the 0°C, at about 400°C).

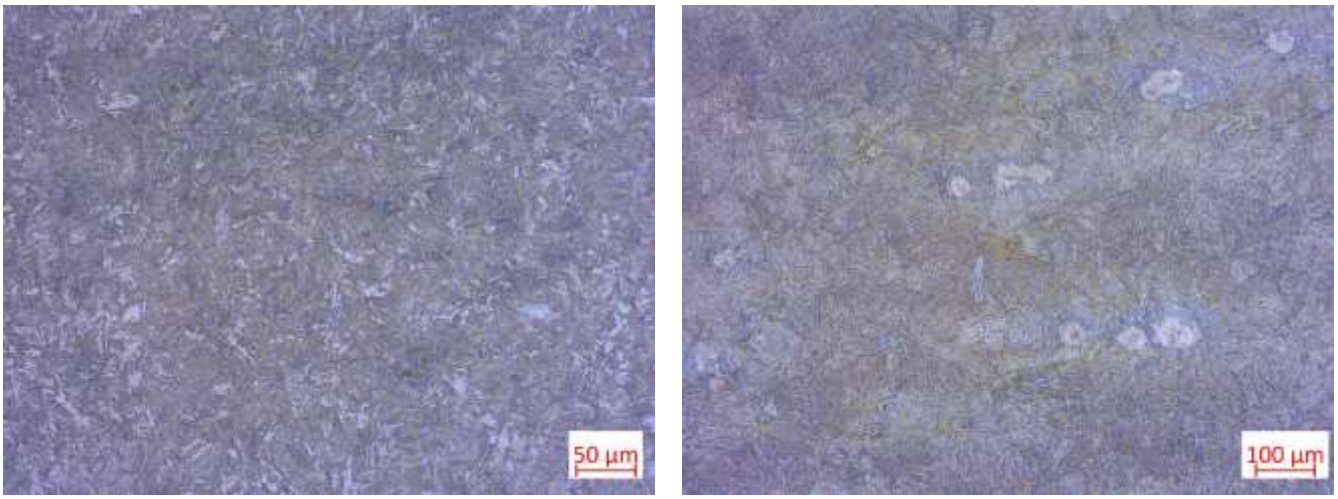

Figure 74 Martensitic microstructure of base material after quenching heat treatment

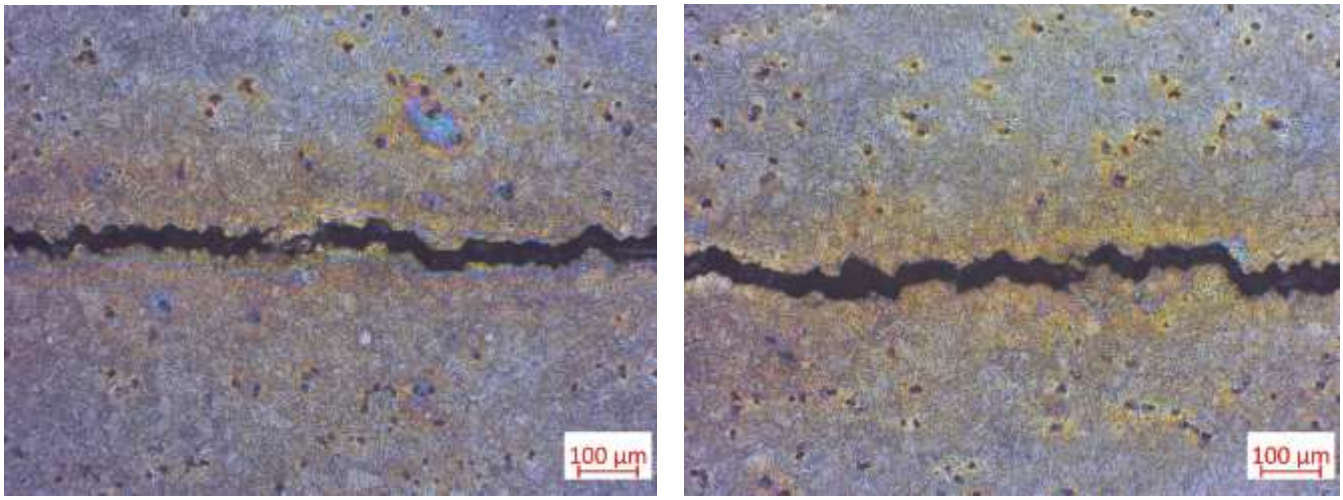

Figure 75 Cracks generated on the welded sample after quenching heat treatment

7.7 Austempering heat treatment

The bainitic steel plates joined with MMA welding process have been subjected to austempering heat treatment. The geometry of the sample that were treated into the furnaces is the same as the one of the MIG welded specimens (see *Chapter 6.7*). The heat treatment was composed by an initial austenitization stage at 900°C for 5 minutes. Successively, the welded sample was taken into another furnace for the isothermal stage of bainitic transformation at 325°C for 3 hours. The temperature of the workpiece in between the two furnace was controlled thanks to a thermocouple.

The CCT and TTT curves derived with JMat Pro software for the filler metal employed in the MMA welding procedure, INE 80B, are represented in *Figure 76*.

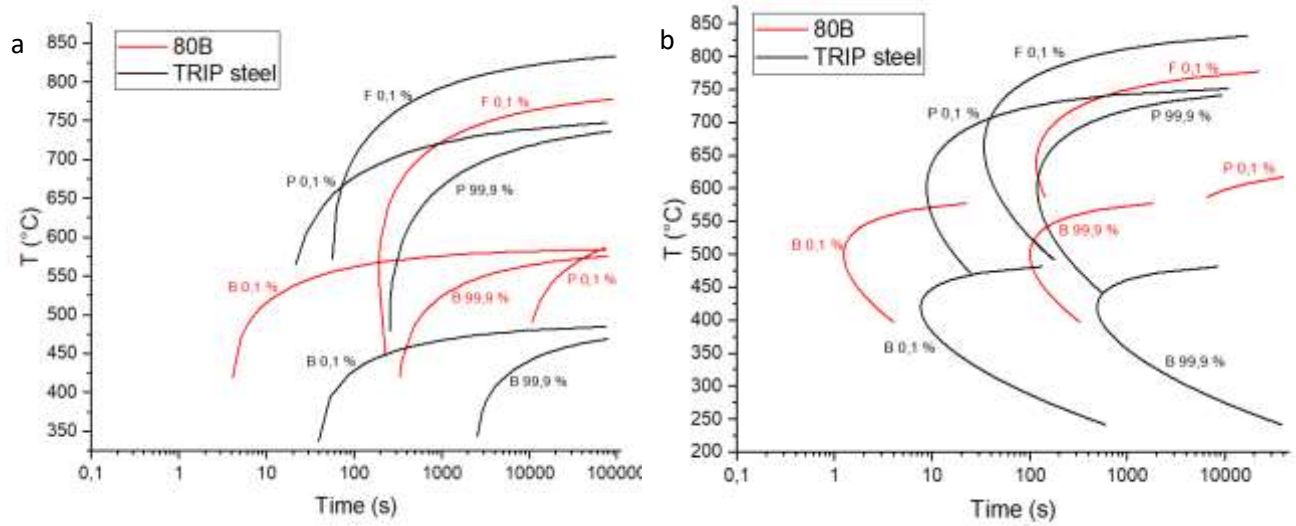

Figure 76 CCT (a) and TTT (b) curves of TRIP steel and MMA filler metal INE 80B

The welded specimen, successively to the heat treatment, was prepared for the SEM analysis. The steel surface, after being grinded and polished, was etched with Nital 2 chemical attack.

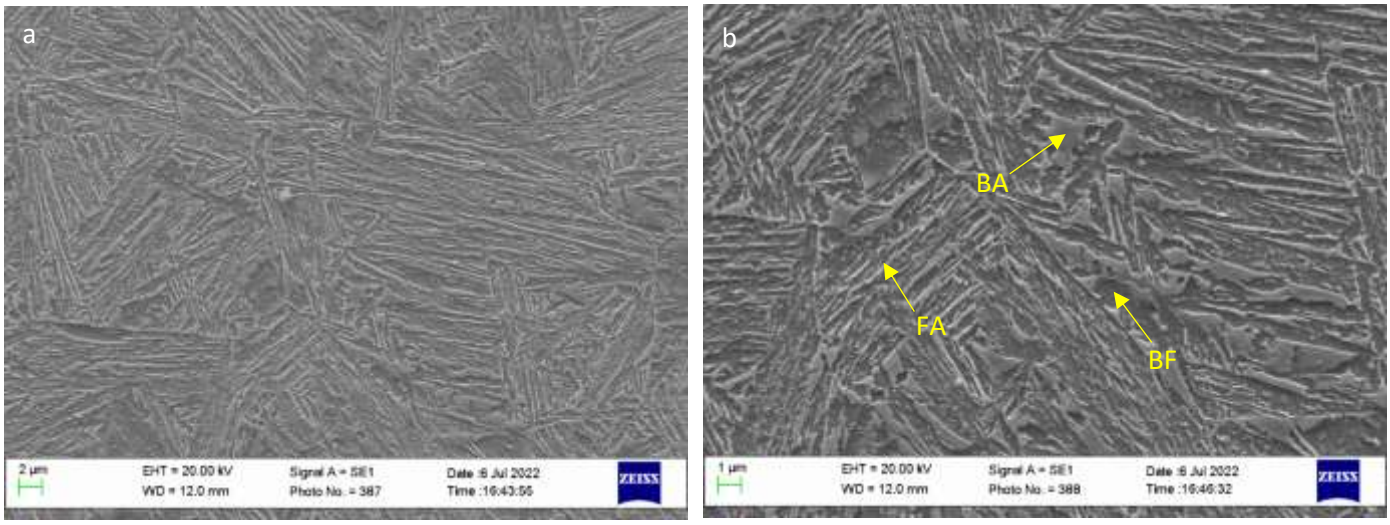

Figure 77 SEM pictures of base material after austempering heat treatment (FA film austenite, BA blocky austenite, BF bainitic ferrite)

In *Figure 77* the base material microstructure obtained after austempering heat treatment is represented. The heat treatment for the MMA welded sample could be considered satisfactory: also in this case, the nano-bainitic microstructure formed by blocky retained austenitic grains, film-like shape austenite, surrounded by carbide-free bainitic ferrite, is successfully obtained. As in the MIG treated specimen, the blocky austenite grains have a dimension of 2-4 μm.

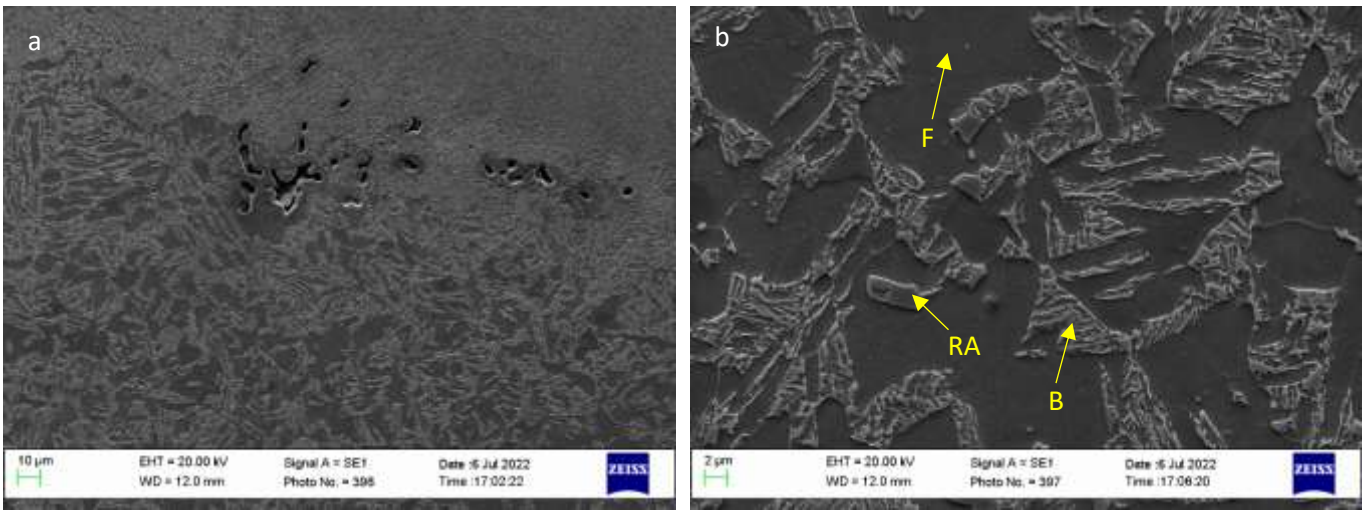

Figure 78 SEM pictures of interface zone of MMA welded sample austempered. F ferrite, RA retained austenite, B bainite

In *Figure 78 (a)* the interface between the base material and the fusion zone is represented. In this, the presence of porosities and defects is detected. These could come from the differential solidification during the welding process due to the presence of low-melting inclusions. In picture (a) the difference in the microstructure composition between the base material and the fusion zone is highlighted. In picture (b), the interface zone microstructure is represented with higher magnification. In this zone there is probably the generation of a ferritic matrix, with the presence of bainitic and austenitic isolated grains. The lack of formation of nano-bainitic microstructure as in the base material is due to the carbon depletion phenomena that occurred in the interface mixing zone [24] [25].

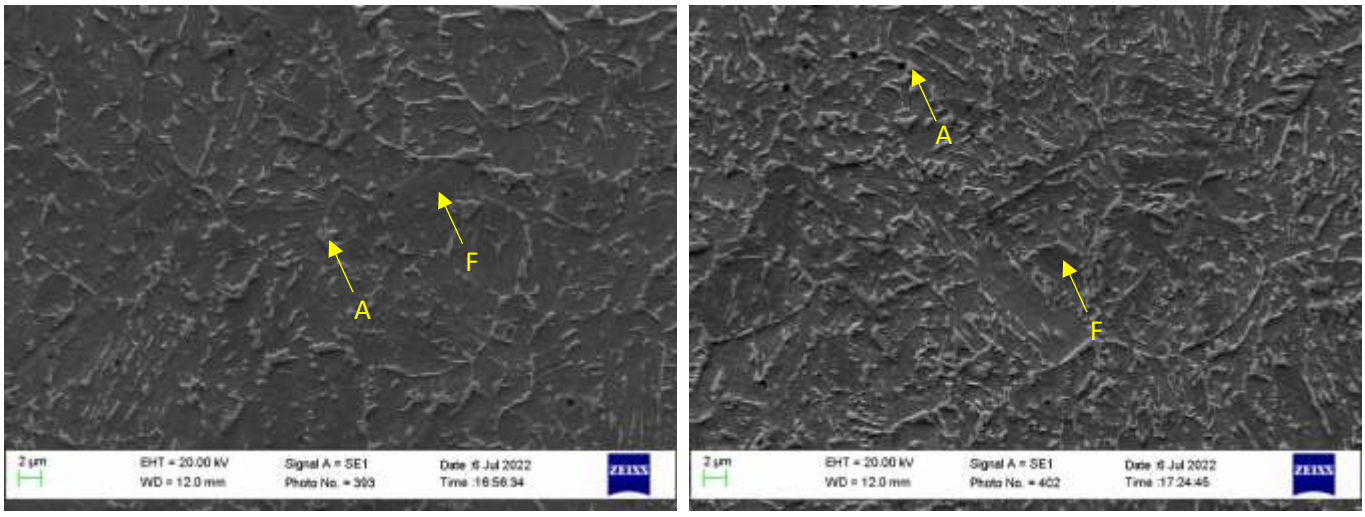

Figure 79 SEM pictures of fusion zone of MMA welded specimen austempered. F ferrite, A austenite

From *Figure 79*, if compared with *Figure 60,* that represents the fusion zone microstructure in the MMA 'as weld' condition, it could be said that the filler metal INE 80B microstructure results almost unaltered by the austempering heat treatment.

Successively to the austempering, the hardness test was conducted. The indentations are taken at the same height of the sample section as in the MMA welded specimen. The examination was carried out with Vickers micro-hardness tester with a load of 300 g.

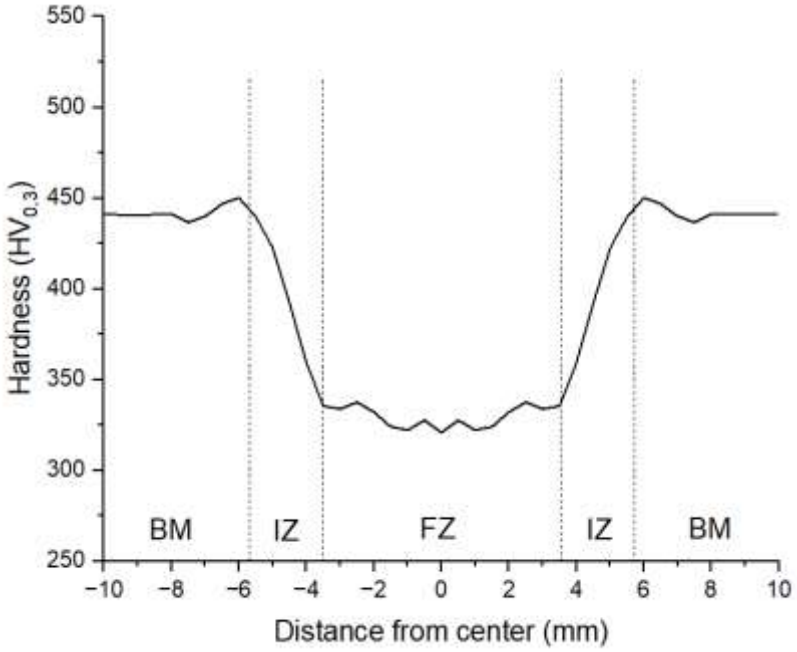

Figure 80 Hardness test results of MMA welded sample austempered

In the case of MMA welded sample austempered there could be find three different zones: the fusion zone FZ, which results with 325-330 $HV_{0,3}$, the interface zone IZ, where progressively the material hardness increases till reaching the base material zone BM where the hardness value stabilizes at 440-450 $HV_{0,3}$. This hardness value is the one which is expected for the nano-bainitic microstructure obtained after austempering heat treatment [27].

From *Figure 81* it could be seen the comparison between the hardness values of the MMA welded sample in the two different conditions: 'as weld' and 'austempered'. The difference in hardness values between the martensitic microstructure of the base material in the 'as weld' sample, and the nano-bainitic one of the 'austempered' specimen could be seen. The peak generated by the refined zone with the austempering heat treatment is no more detected, this is due to the homogenization of the microstructure in the heat affected zone. It could be distinguished a sensible increase in the hardness value of the fusion zone when the welded specimen undergoes to the austempering heat treatment.

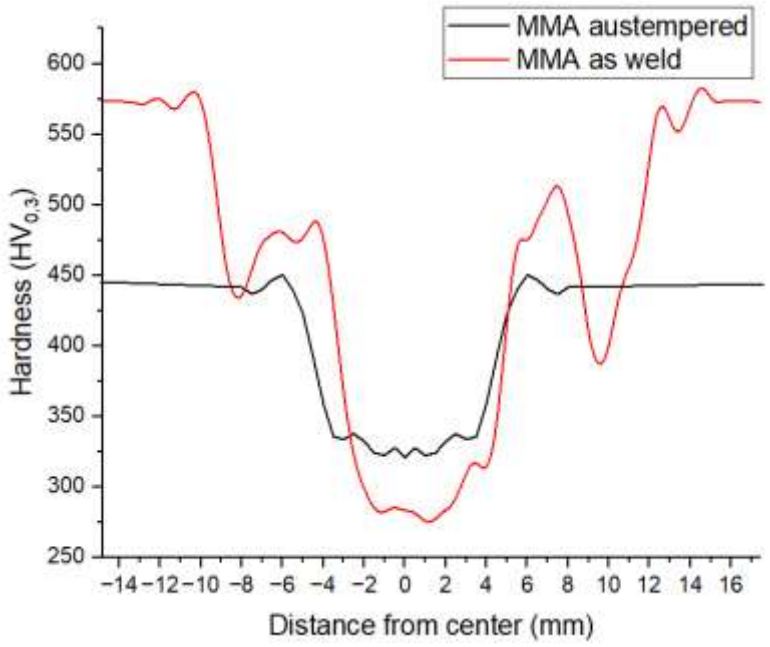

Figure 81 Hardness test results of MMA welded sample in 'as weld' and 'austempered' condition

The MMA welded sample austempered microstructure composition was examined with XRD diffractometer for phase identification and quantification.

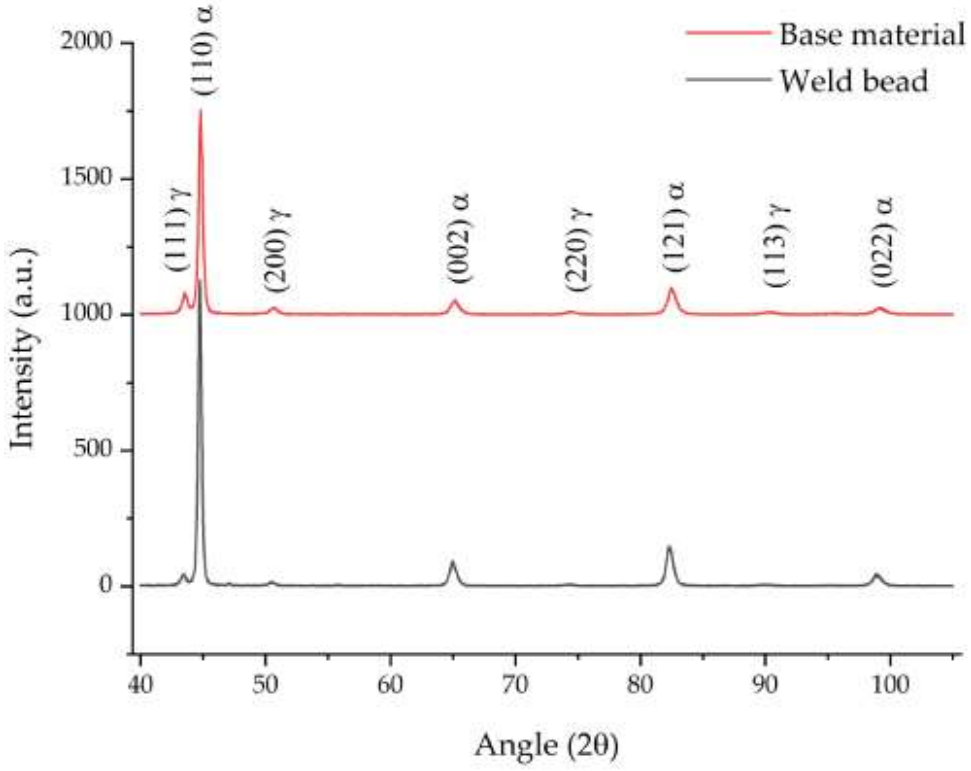

Figure 82 XRD pattern resulted for phase identification of MMA sample 'austempered'

Zone	V_γ	X_γ	V_α	X_α	$V_{\alpha'}$	$X_{\alpha'}$	$V_{\alpha b}$	$X_{\alpha b}$
Weld bead	6.22	1.26	47.63	0.03	46.15	0.24	-	-
Base material	24.98	1.02	-	-	-	-	75.01	0.17

Table 19 Results of XRD for phase quantification of MMA sample 'austempered'. V_γ, volume fraction of retained austenite, X_γ, carbon content wt. % in retained austenite, V_α, volume fraction of α-ferrite, X_α, carbon content wt. % in retained austenite, $V_{\alpha'}$, volume fraction of martensite, $X_{\alpha'}$, carbon content wt. % in martensite, $V_{\alpha b}$, volume fraction of bainitic α-ferrite, $X_{\alpha b}$, carbon content wt. % in bainitic α-ferrite.

The austempering heat treatment, at which the welded sample was subjected, produced the desired microstructure. This is confirmed by the base material XRD analysis results, where the microstructure is composed principally by ferritic bainite and retained austenite. The bainitic ferrite laths are carbon super-saturated [28]. The weld bead microstructure is composed by a marked content of martensite, which almost equals the one of α-ferrite. This volume fraction is huge in comparison with the one obtained for the MIG welded sample austempered, which is 6.90 %.

8. TIG (GTAW) process results

8.1 Visualization and penetrating liquids

The bainitic steel plates were successively welded together with the Tungsten Inert Gas process. The welding parameters employed are reported in *Table 11.* The welded surface, in comparison with the MIG and MMA, presented lower amount of sputter. This is due to the better control of the filler metal when is fused and deposited on the base material.

Figure 83 Pictures of welded plates with TIG process

In *Figure 83* (a) the weld bead front view is represented. In the picture (b) there is the representation of the weld bead with a higher magnification. In this, the last three passes of the welding process could be clearly distinguished. In the last pass, the smoothness of the process is appreciated: in comparison with MIG and, more markedly, with MMA, the TIG procedure generates a very clean weld bead, with the absence of bumps or deposits of matter. Obviously, also in this case the interface between the last passes is generated. From these first pictures, it could be already stated that this process comprises a greater extension of the base material alteration, in comparison with the other two welding procedures. In the image (c), the back view of the welded plates is showed. In this welding process, as in the MMA, a "recovery" welding pass is employed to guarantee the join between the two steel plates.

The presence of macro cracks or defects on the weld bead was evaluated through the penetrating liquids. The lower amount of sputtering produced in TIG welding procedure facilitates this kind of analysis, with a better diffusion of the red penetrating liquid into the eventual cavities.

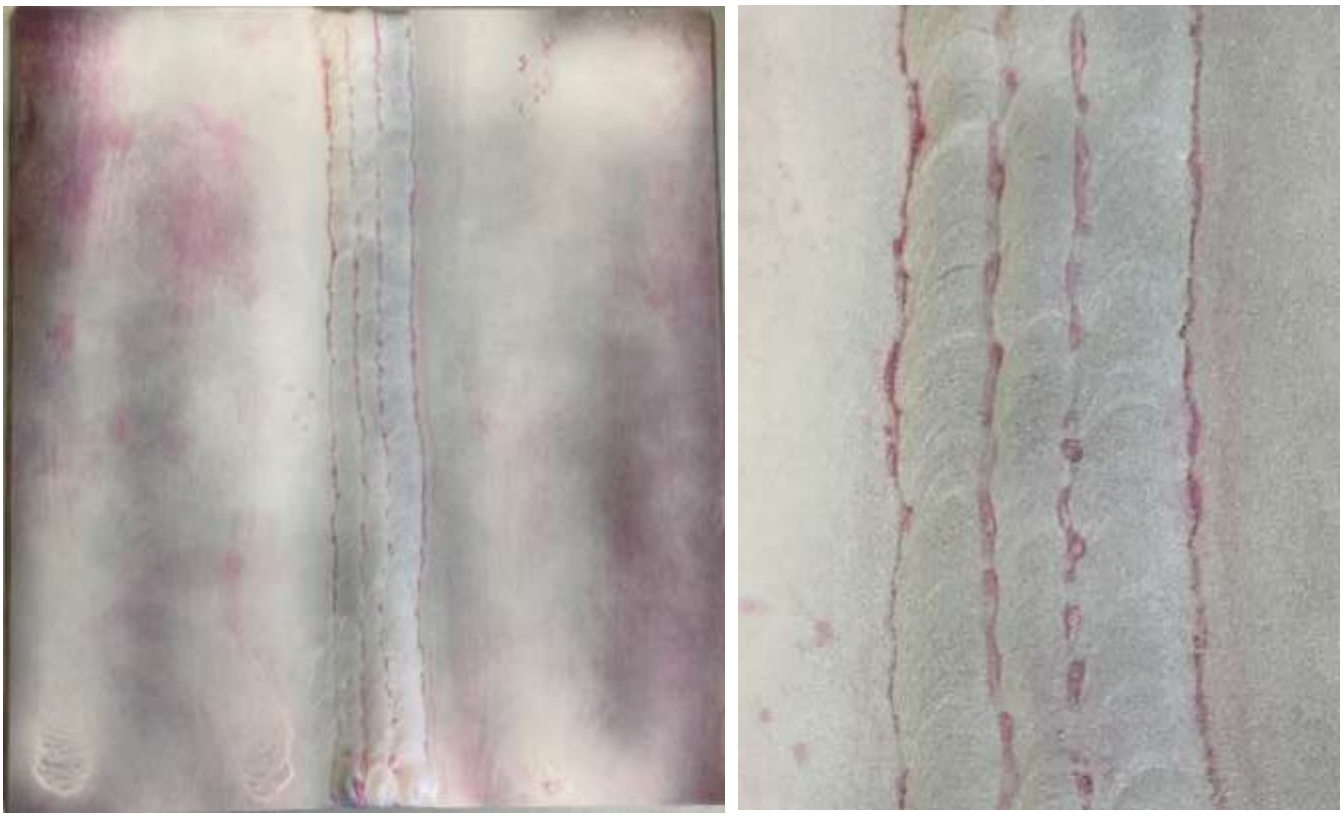

Figure 84 Penetrating liquids results on TIG welded plates

As could be seen from *Figure 84*, the white revealer didn't show cracks or defects on the weld bead surface or in the material near the welded zone. From this, the TIG welding procedure is considered acceptable from macroscopic point of view.

8.2 Residual stresses

The residual stresses induced by the TIG welding process have been tested with the utilization of the XRD diffractometer, as in the other two welding procedures. The analyzed points, on the weld bead and steel plates surface, were distributed in the same positions as in the MIG and MMA. However, in this case the test was conducted with a smaller number of points; after the other two analysis, a lower number of points, that comprises the crucial positions on the welded plates, is enough for determining the stress situation induced by the welding process. In particular, the points 7,8,9 on the weld bead surface are not considered in this test. This because the distribution of the residual stress on the weld bead doesn't change in function of the position, either at the beginning or end of the bead where it could be expected some deviations from the value at point 0.

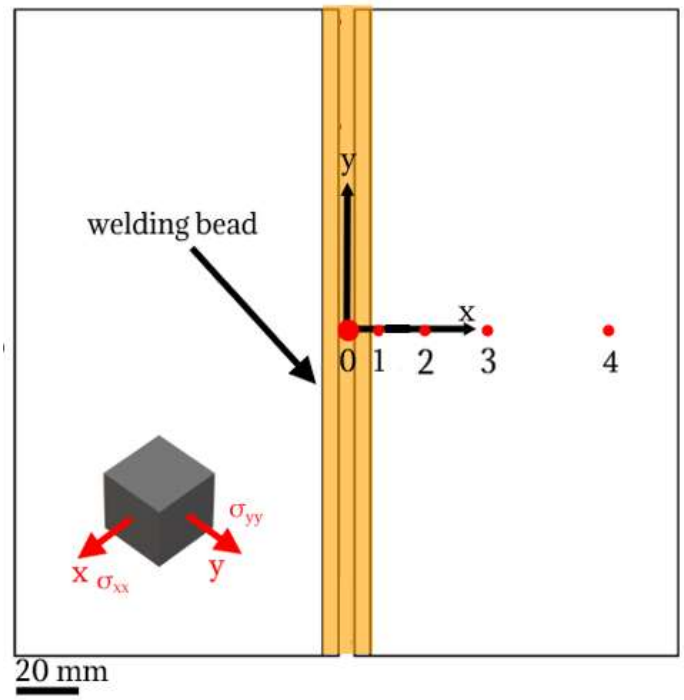

Figure 85 Optimized distribution of points for residual stress analysis

Point	Stress σ_φ in X plane [MPa]	Stress σ_φ in Y plane [MPa]
0	23	344
1	197	310
2	-363	-258
3	-310	-176
4	-434	-233

Table 20 Residual stress tests results of TIG welded plates

The results obtained for the TIG welding process are conform to what was expected. The join procedure, analyzed in the X plane direction, induced a tensile stress situation on the welded steels in correspondence of the weld bead. This could be stated from the strong reduction of the compressive stress situation that characterizes the original bainitic steel plates (-861 MPa in X plane, -310 in Y plane). As the distance from the weld bead increases, the induced tensile load decreases. This is confirmed by the progressive increase of the negative compressive stress state.
The evaluation of the residual stress situation in the Y plane direction gives the following results. The values obtained in the points 0 and 1 on the top of the weld bead, confirm the tensile stress state that is generated in the parallel direction of the welding procedure. The other points are characterized by a lower compressive state, so less negative, in comparison with the results in the longitudinal direction (X plane). This is justified by the lower compressive state that characterizes the steel plates in the original condition.

The results of the XRD diffractometer of the three different welding process employed, MIG, MMA and TIG, are now compared between each other.

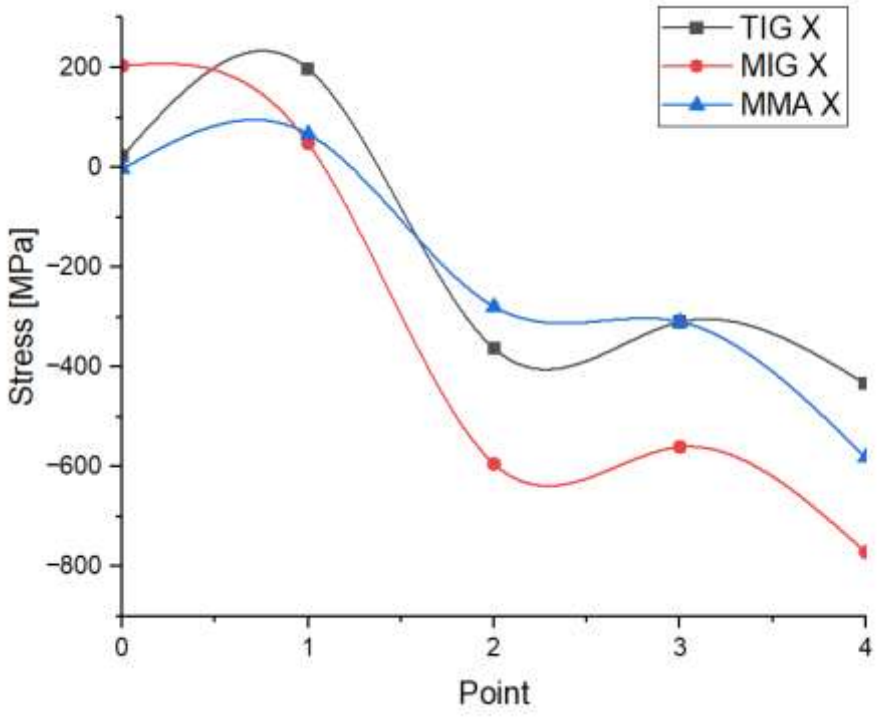

Figure 86 Residual stress development for different welding processes analyzed in longitudinal X plane

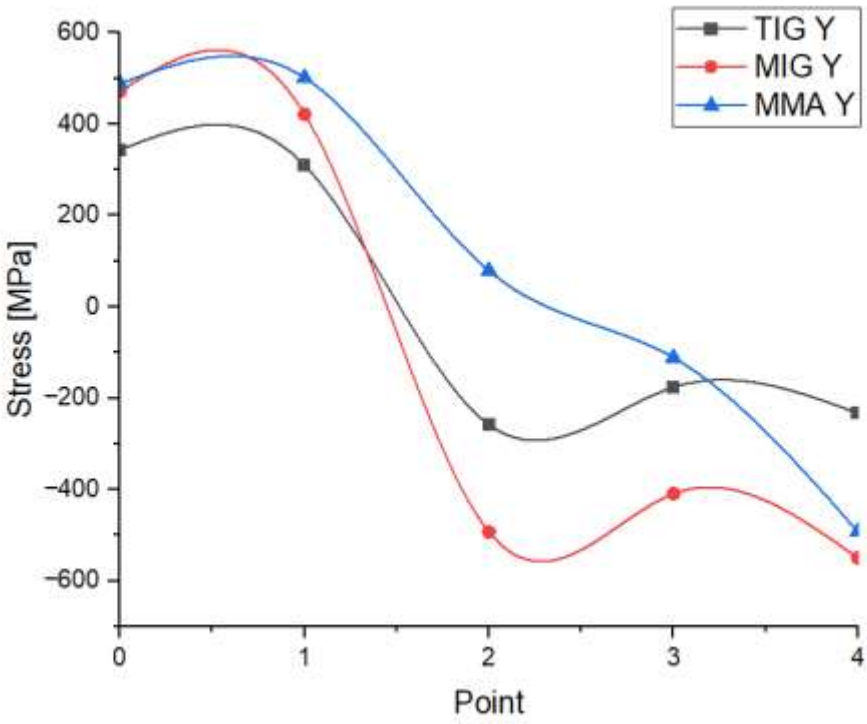

Figure 87 Residual stress development for different welding processes analyzed in parallel Y plane

In *Figure 86* the values obtained, from the analysis of the points in the X direction, plainly represent the influence of the welding processes on the stress state of the steel plates. In point 0 the material is unstressed from the TIG and MMA welded plates, instead a tensile stress state is detected in the case of MIG. In the point 1 all the three samples show a tensile stress state. In this position the highest stress influence of the welding processes is detected. From this point, the welded materials exhibit a progressive reduction in the tensile state, with an increase in the compressive stress state. It could be noted that the TIG sample shows the lowest, so less negative, compressive state from point 2 to point 4, followed respectively by the MMA and MIG welding procedures. In other words, on the TIG welded plates a higher tensile stress state is induced from the welding process, which is detected in the whole longitudinal spacing of the plates. In particular, in point 4 (where the stress situation is evaluated in the original steel plates), the difference in the induced tensile stress from the TIG, MMA and MIG is evident. This result is justified by the welding parameters that characterize the different procedures. In fact, an average higher heat input is obtained respectively in the TIG and MMA processes in comparison with the MIG one. The first two denote a lower welding speed and a higher number of passes (see *Table 9, 10, 11*). These generate a higher heat input, which is traduced in a wider altered section of the welded material. Moreover, the different polarization of the electrode and base material plays an important role in the heat gain of the three welding procedures. In fact, the TIG is characterized by a negative polarized electrode (DCEN), instead the MIG and MMA have a positive polarized electrode configuration (DCEP). In the case of TIG this layout is chosen for reducing the

consumption of the tungsten electrode. This is traduced in a higher amount of heat received by the base metal, which justify the higher influence of the welding process in TIG plates in comparison with MMA. The experimental procedures conducted by Jin Jang et. al. [29] confirms the influence of the welding heat input on the residual stresses results.

In *Figure 87* is represented the development of the residual stress results in the parallel Y plane direction. For all the three welding processes, the point 0 and 1 results in a strong tensile stress situation. This because of the welding direction parallel to the Y plane of detection. In the successive points there is the decrease of the tensile stress state, reaching the minimum in the point 4. In this position, the TIG welding process is confirmed as the one that induced the higher residual stress state, followed by the MMA and then by the MIG.

8.3 Optical microscopy and SEM

The TIG welded sample were analyzed at the optical microscope. To do the optical microscopy the welded plates have been cut longitudinally to the weld bead direction, in order to derive the section of the different thermally altered zone. The steel surface was chemically etched with Klemm's I and looked at the microscope with polarized light.

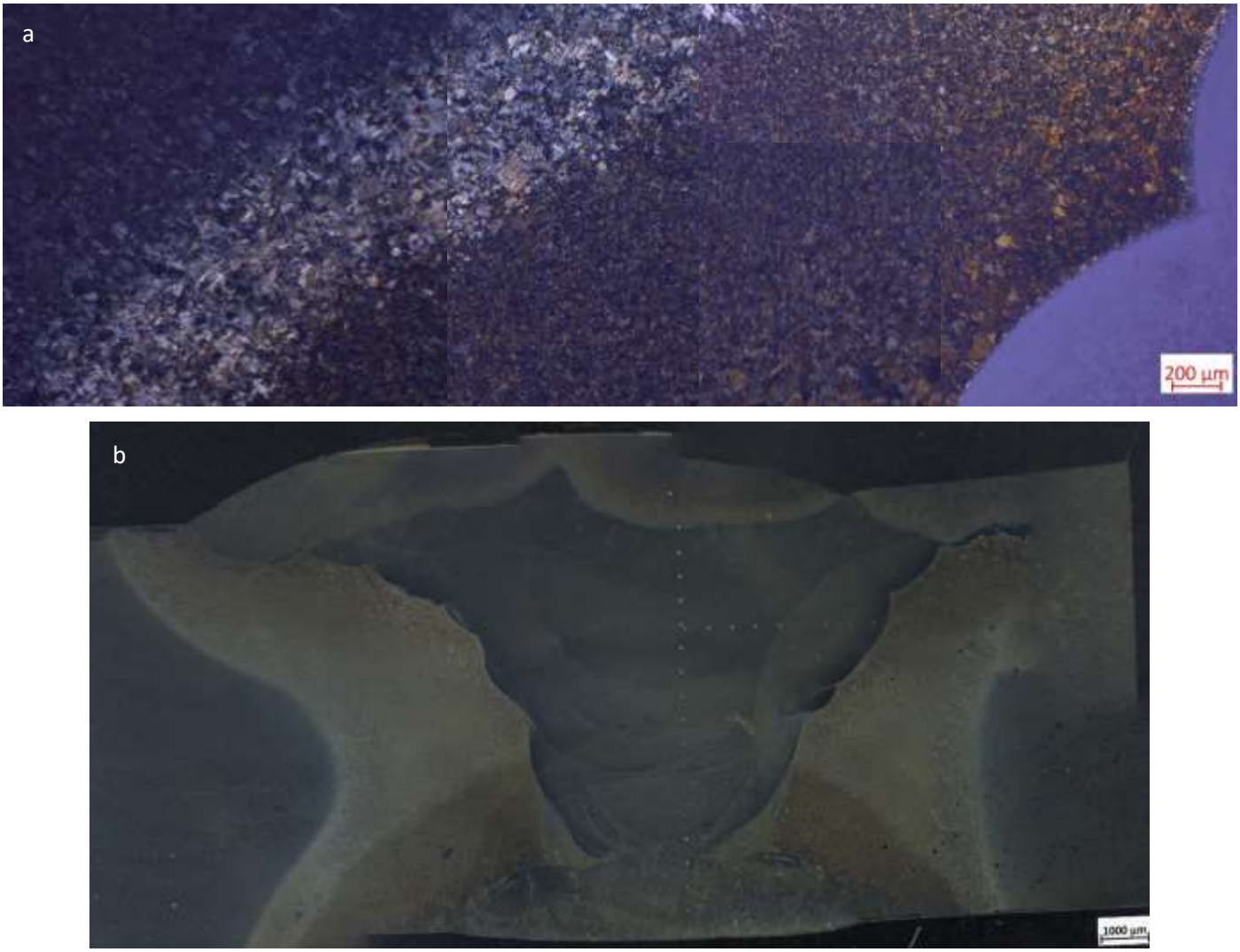

Figure 88 Optical microscope picture of welded sample heat affected zone (a) and weld bead section (b)

The microstructure that could be seen in *Figure 88* is characterized by the fusion zone FZ in light blue (on the right), a first mixing coarsened zone where the base material and the filler metal join, a refined zone in the middle of the heat affected zone, a second coarsened zone at the end of the HAZ and finally the base material.

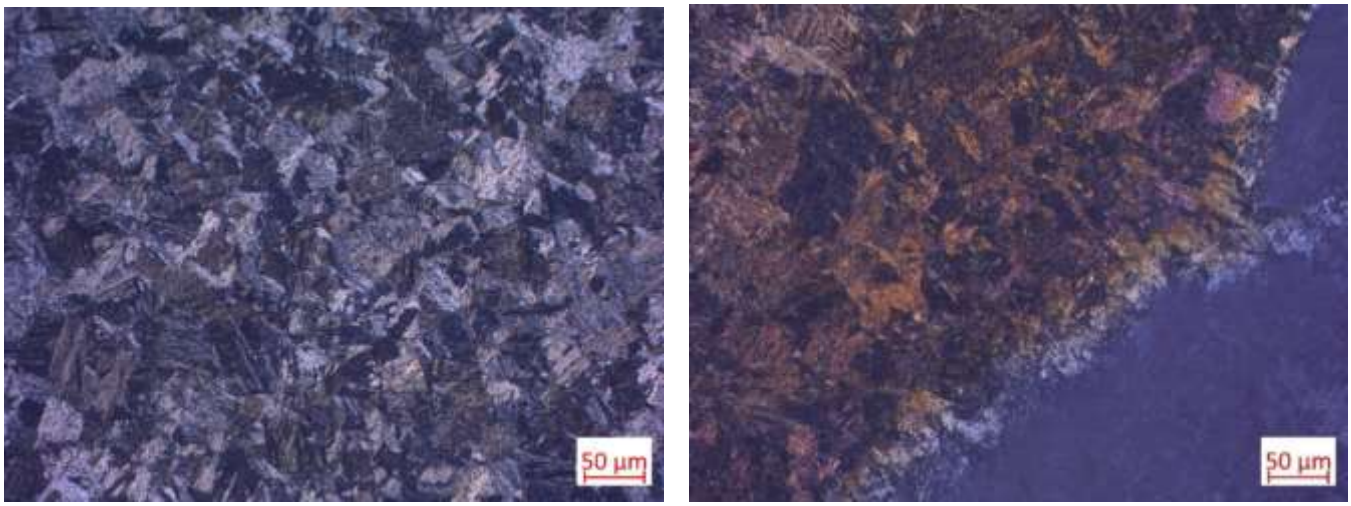

Figure 89 Higher magnification pictures of coarsened HAZ on the left, and mixing coarsened zone on the right

The picture represented above is obtained in the zone where the hardness test imprints are taken. If compared with the *Figure 30*, where the MIG heat affected zone microstructure is represented, it could be clearly seen that in the case of TIG the extension of the microstructural alteration is larger.

Successively, the fusion zone FZ was analyzed more in detail. In particular, the steel surface microstructure was inspected without the polarized light. Thanks to this, the columnar grains of solidification were highlighted. The same microstructure is shown with or without the utilization of polarized light in *Figure 90.*

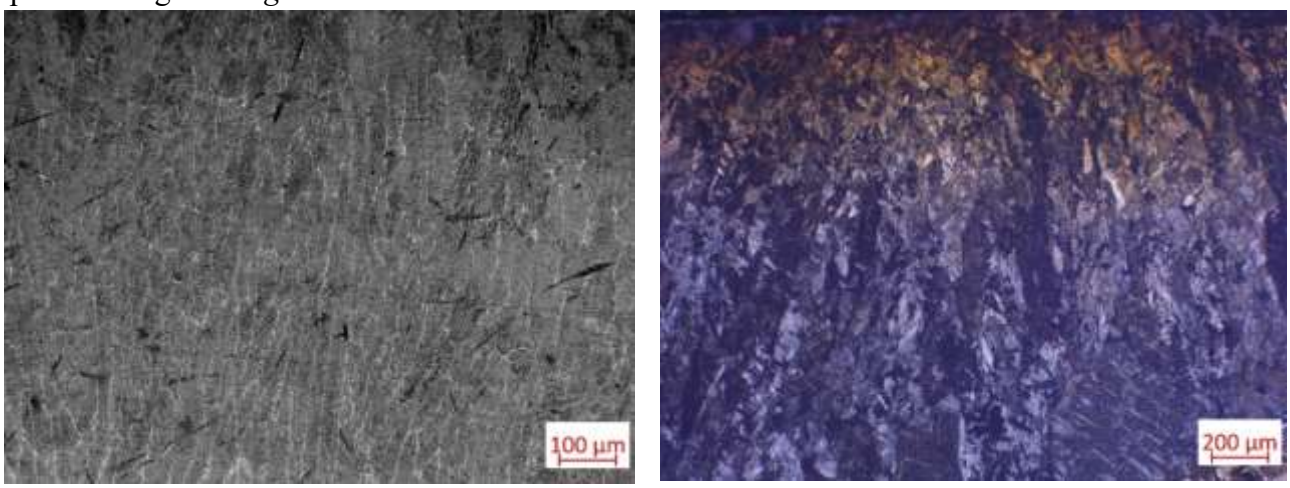

Figure 90 FZ microstructure without polarized light lens (on the left) and with polarized light lens (on the right)

The ‘as weld’ TIG samples microstructure of the thermally altered zones and fusion zone was analyzed at Scanning Electron Microscope (SEM).

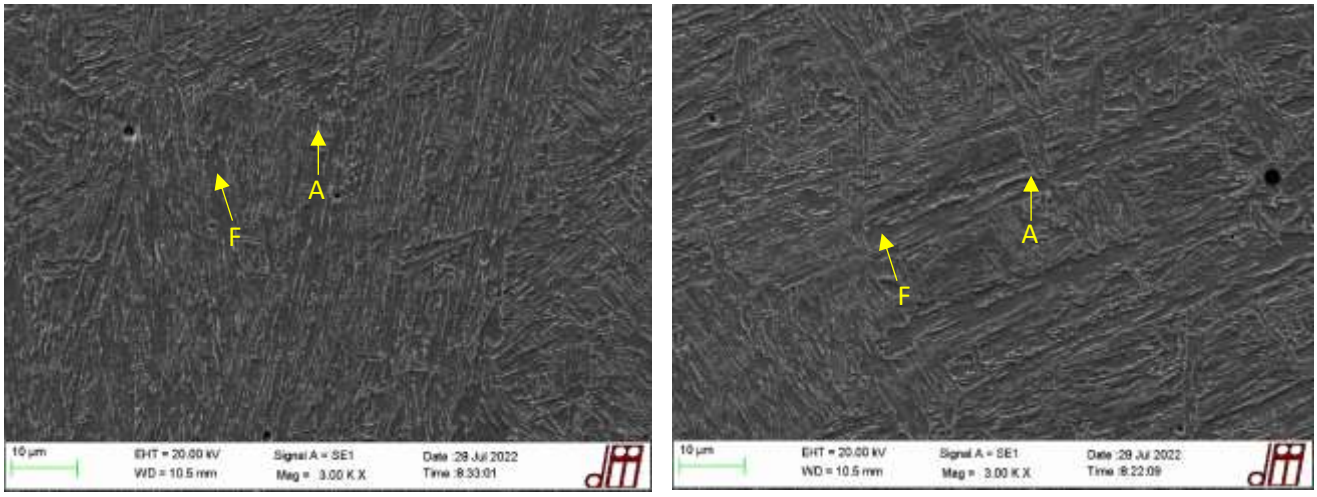

Figure 91 SEM pictures of fusion zone FZ

The microstructure obtained in the fusion zone is composed by a matrix of α-ferrite (the darker zones) with the presence also of austenitic islands. This is confirmed in the XRD diffractometer analysis successively conducted. The base material SEM images are considered as the same obtained in the case of MIG and MMA welding processes.

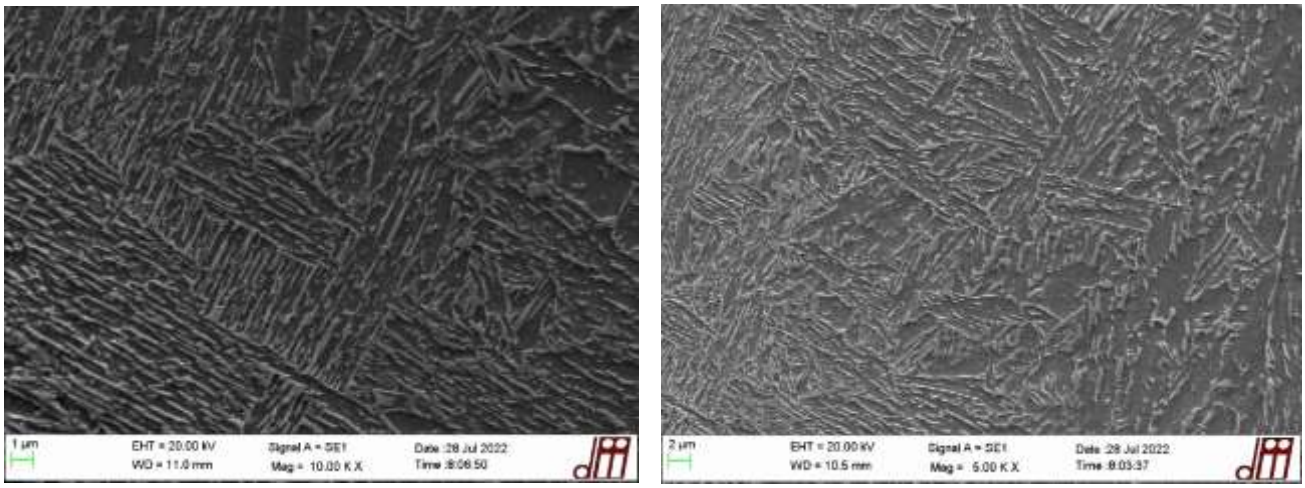

Figure 92 SEM pictures of mixing zone MZ

In *Figure 92* the mixing zone MZ obtained in the TIG welded sample is represented. This is characterized probably by tempered martensite and bainitic microstructure.

8.4 Hardness

The hardness tests were conducted with Vickers micro-hardness procedures on the welded metals. The indentations were taken at the same height of the welded section sample of the other two welding processes, so at about 2 mm from the top. The examinations are managed with Shimadzu Vickers micro-hardness tester, employing a 300 g as load. Successively the two diagonals of each imprint, which has a space of 500 µm from the next one, are measured with the image software analysis Zeiss ZEN.

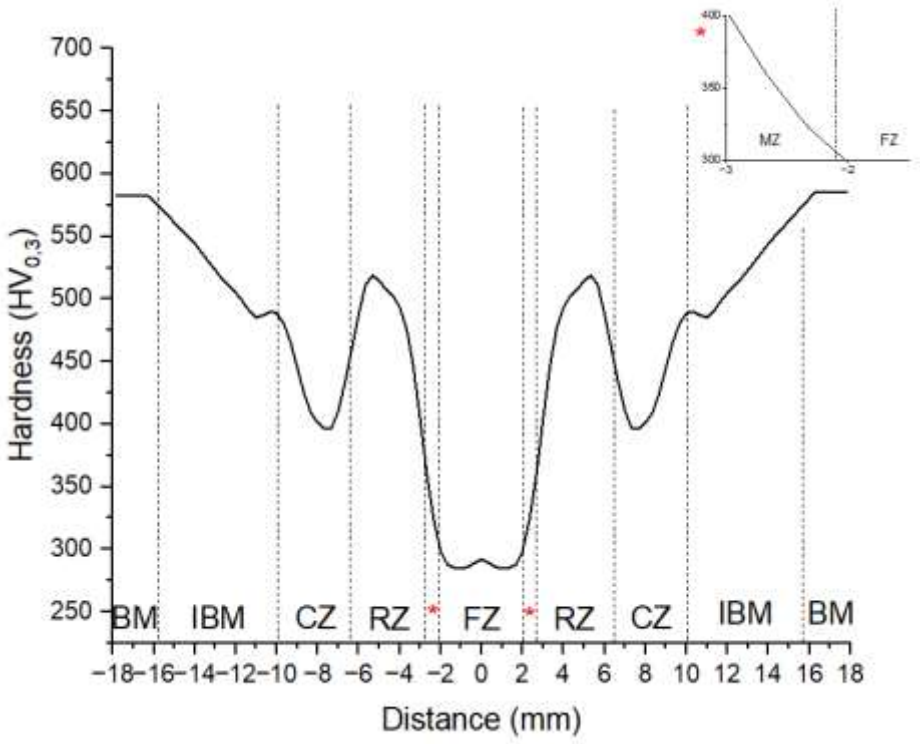

Figure 93 Representation of TIG welded plates hardness development

In *Figure 51* different zones that characterizes the welded section can be distinguished. The central fusion zone FZ, got a hardness value up to 290-300 $HV_{0,3}$. The zone marked with the "*" is the mixing zone MZ, which is immediately after the FZ. This is slightly harder than the fusion zone, with a value between 325-350 $HV_{0,3}$. The refined zone RZ is characterized by a peak of hardness at about 525 $HV_{0,3}$. This is generated by the welding process heat cycles, which take the material at high temperatures and cause the refinement of the microstructure. Successively to the RZ, the coarsened zone CZ is individuated, with the valley hardness result of 390 $HV_{0,3}$. The next zone is the influenced base material IBM, in this there is the progressive increase of the hardness value until it reaches the base material BM resulted in 580 $HV_{0,3}$. The extension of the IBM zone must be highlighted. This is due to the elevate heat input generated by the TIG welding process, which cause a wider altered base material from the weld bead.

The overall horizontal extension of the heat affected zone generated by the TIG welding procedure resulted up to 16 mm.

The hardness tests results of the bainitic steel plates ‘as weld’ with MIG, MMA and TIG welding process are compared.

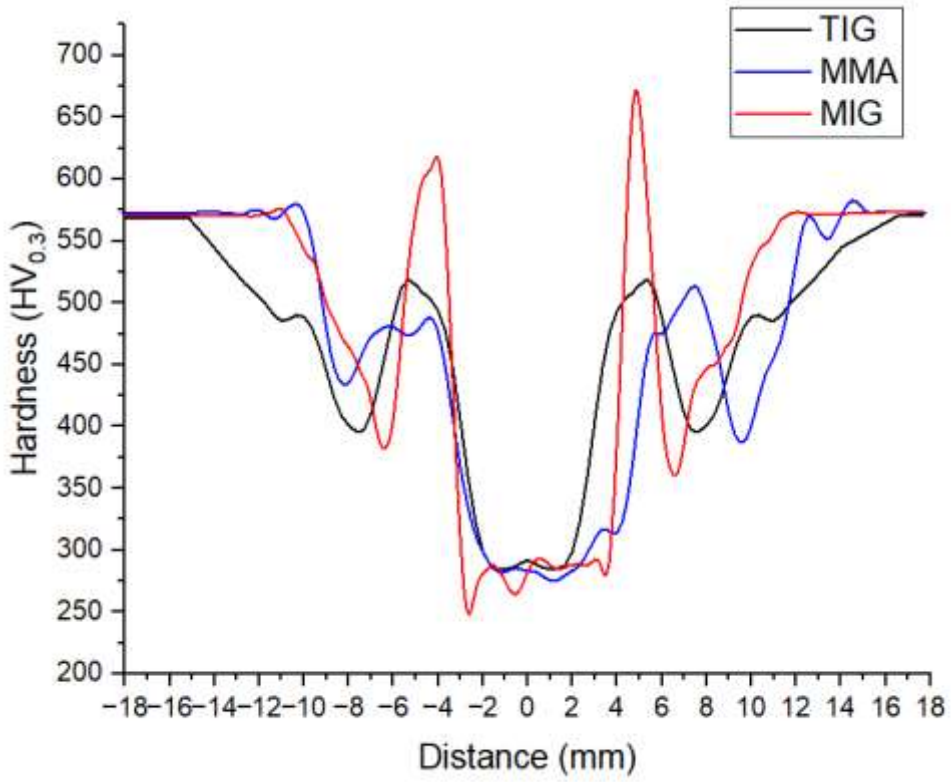

Figure 94 Hardness tests results of the three different welding processes

The hardness results obtained from the examinations of the different welding procedures agree to what could be expected. First, the difference in the heat affected zone width in the three processes could be seen. On the positive side of the x axis, the distance from the center of the weld bead (at 0 mm) at which the material hardness stabilizes, could be considered as the principal indication of the end of the heat affected zone. For the MIG process this is individuated at about 11 mm, for the MMA at 14 mm, and finally for the TIG is recognized at 16 mm. As could be stated from the *Table 9,10* and *11,* the welding process which is characterized by the lower heat input, taking into account welding speed and polarization of the electrode, is the MIG (SMAW). As could be seen from the *Figure 94*, the material welded with SMAW procedure is the one that stabilizes the hardness value of the base material at the lowest distance from the weld bead. The MMA (GMAW) welded plates stabilize the hardness value of the base material at an intermediate distance between the MIG and the TIG (GTAW). This last one generated the wider heat affected zone in comparison with the other two welding procedures. This fact is justified by the higher heat input obtained in the TIG process in

comparison with MMA and MIG. The influence of the heat input magnitude in the heat affected zone width is confirmed by the experimental study of G. Madhusudhan Reddy [30], where the SMAW and GTAW welding processes are compared. Also in this case, the GTAW gives a wider heat affected zone on the base material in comparison with the SMAW.

The heat gain difference between the SMAW, GMAW and GTAW is individuated also in the height and width of the refined zone RZ peaks and coarsened zone CZ valleys. In particular, the RZ peaks of the MMA and TIG processes are quite equal: these are wider and lower in comparison to the one of the MIG sample. This is traduced in a softer microstructure in the RZ and CZ in the case of TIG and MMA, in comparison with the MIG sample. The microstructural alteration is lower in this last one, with the base metal martensitic microstructure that undergo to a lower tempering heat cycle, so higher cooling rate that is traduced in higher hardness value. The other important motivation for the differential hardness values in the RZ and CZ, between the MIG and the other two MMA and TIG welding processes, is the difference in the carbon content between the bainitic steel base material and the low carbon filler metals. In particular, the base material has a C content up to 0,38 % wt., instead in the filler metals employed the average carbon content is 0,07-0,08 % wt. This justifies the lower hardness value of the heat affected zone in the case of TIG and MMA in comparison with MIG: the higher heat input induced by the first two enhanced the diffusion kinetics for the movement of carbon. The base material, which has the highest C content so result depleted from it and get softer, the fusion zone filler metal, which has the lowest C content so result enriched of it and get harder. The study on welding of dissimilar metals conducted by Yuh-Ying You et. al. [24] and Peter Mayr et. al. [25] confirms the migration of alloying elements, such as carbon or chromium, in the correspondence of the fusion zone where high temperatures are reached and the different materials are joined.

8.5 XRD for phase identification and quantification

The TIG welded sample microstructure composition was analyzed with XRD diffractometer.

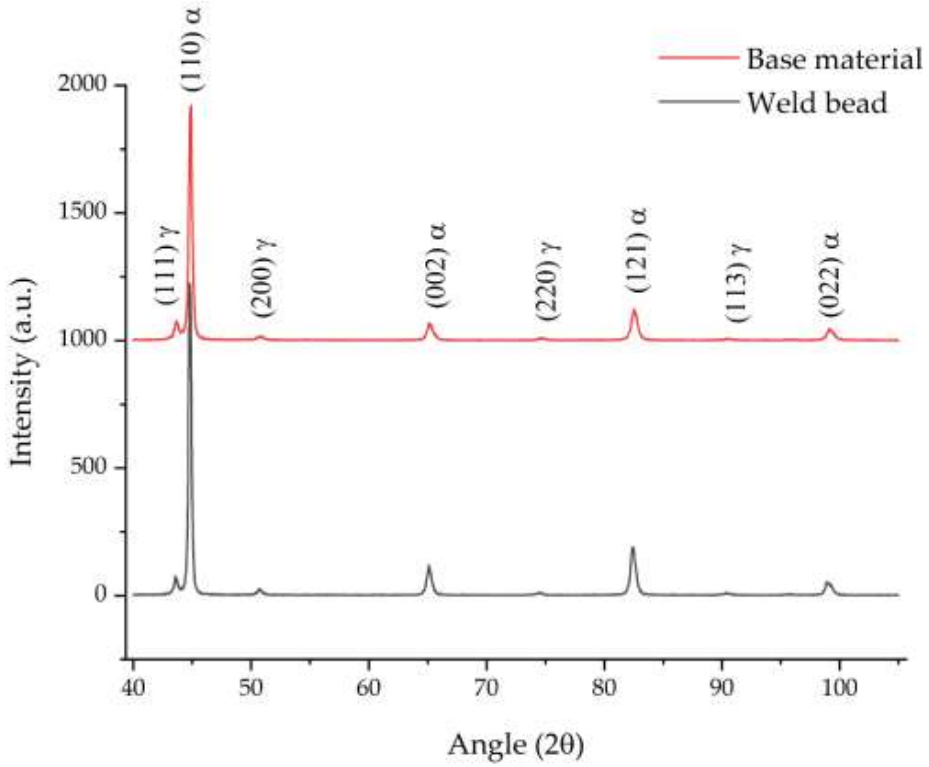

Figure 95 XRD pattern resulted for phase identification of TIG sample 'as weld'

Zone	V_γ	X_γ	V_α	X_α	$V_{\alpha'}$	$X_{\alpha'}$
Weld bead	8.97	0.95	72.57	0.03	18.44	0.42
Base material	5.50	0.58	-	-	94.5	0.24

Table 21 Results of XRD phase quantification for TIG sample 'as weld'. V_γ, volume fraction of retained austenite, X_γ, carbon content wt. % in retained austenite, V_α, volume fraction of α-ferrite, X_α, carbon content wt. % in retained austenite, $V_{\alpha'}$, volume fraction of martensite, $X_{\alpha'}$, carbon content wt. % in martensite

The weld bead composition shows a higher content of martensite in comparison with the ones obtained in the MIG and MMA sample in the 'as weld' condition.

8.6 Austempering heat treatment

The TIG welded sample was subjected to the austempering heat treatment. This consists first in an austenitization stage at 900°C for 5 minutes. The specimen was cooled in air till reaching 350°C, with the temperature of the workpiece monitored by a thermocouple, and after it was introduced in a heat furnace at 325°C for the isothermal stage where the bainitic transformation was completed after 2,5 hours.

The microstructure obtained after the heat treatment was analyzed at the optical microscope. After being mounted into the epoxy resin, grinded and polished, the steel surface is etched with Nital 2 to reveal the nano-bainitic microstructure.

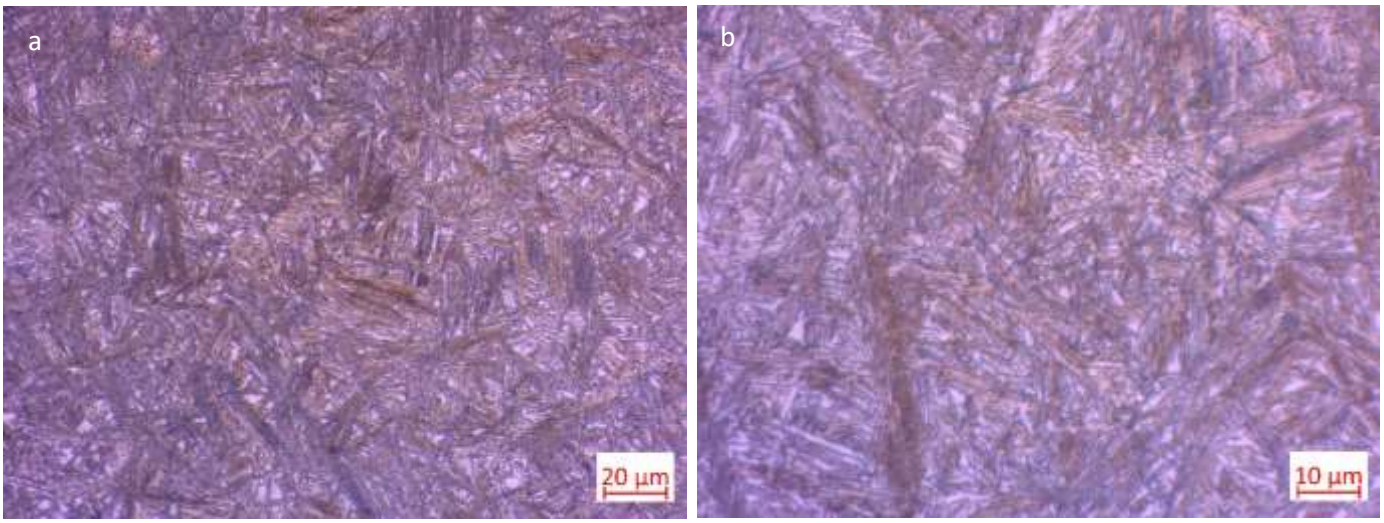

Figure 96 Optical microscope pictures of base material of TIG welded sample austempered at 500x (a) and 1000x (b) magnification

The analysis of the base material microstructure at the optical microscope results acceptable: the bainitic microstructure could be recognized.

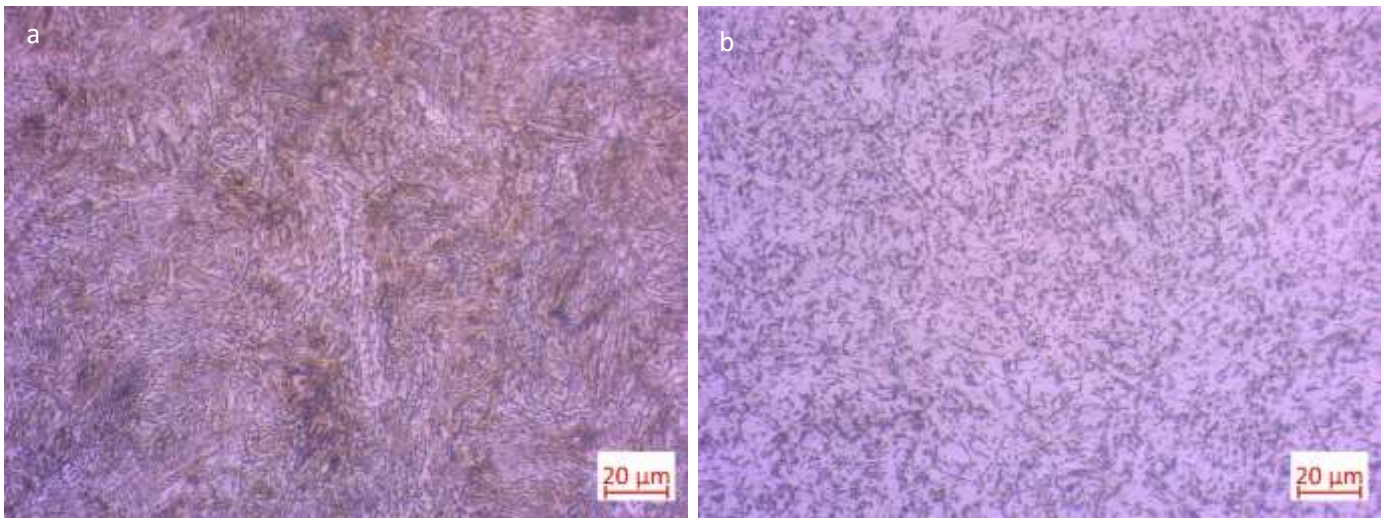

Figure 97 Optical microscope pictures of interface zone (a) and fusion zone (b) of TIG welded sample austempered

The microstructure composition at the optical microscope could be partially analyzed: since the elements that compose the bainitic microstructure obtained after the austempering heat treatment are in the size of nanometer as order of magnitude, the magnifications that could be reached with the optical microscope lens weren't sufficient.

For this reason, the TIG welded sample austempered was analyzed at the scanning electron microscope SEM, where very high magnification could be achieved.

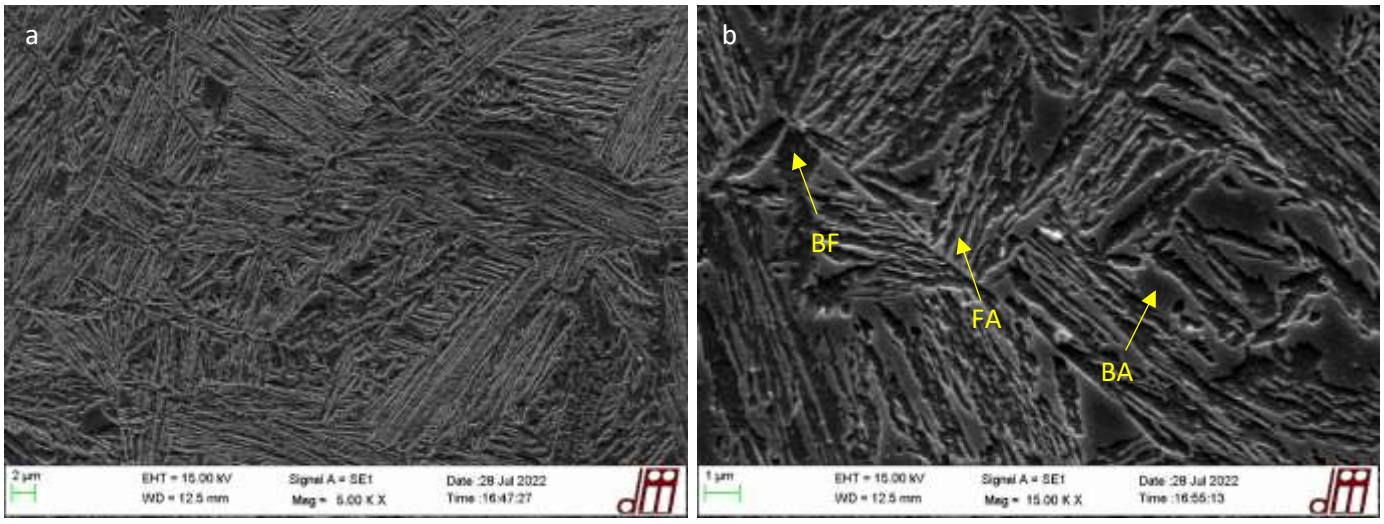

Figure 98 SEM pictures at 5000x (a) and 15000x (b) of base material of TIG welded sample austempered

In picture 'b' the different structures that compose the nano-bainitic one are clearly visible: the blocky austenite grains (BA), the film-like retained austenite (FA), the bainitic ferrite matrix (BF).

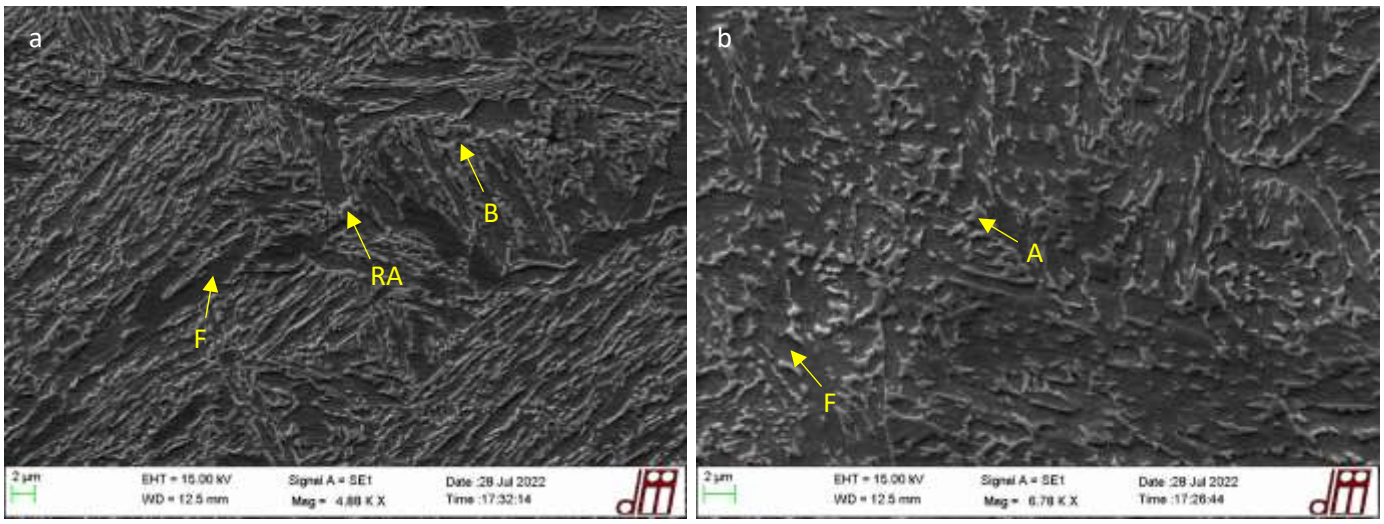

Figure 99 SEM pictures of interface (a) and fusion zone (b) of TIG welded sample austempered. F ferrite, RA retained austenite, B bainite, A austenite

As could be noted from *Figure 77* 'b' the microstructure obtained in the fusion zone is basically unaltered from the austempering heat treatment. In fact, the austenite islands surrounded by the ferritic matrix could be clearly recognized. In picture 'a' the mixing interface microstructure shows

the presence of a non-completely generated nano-bainitic microstructure. Also in this case, the carbon depletion of this zone [24] [25] reduce drastically the retained austenite stability.

Successively to the SEM analysis, the TIG sample austempered hardness was studied. This was done by Vickers micro-hardness test, with 300g as applied load.

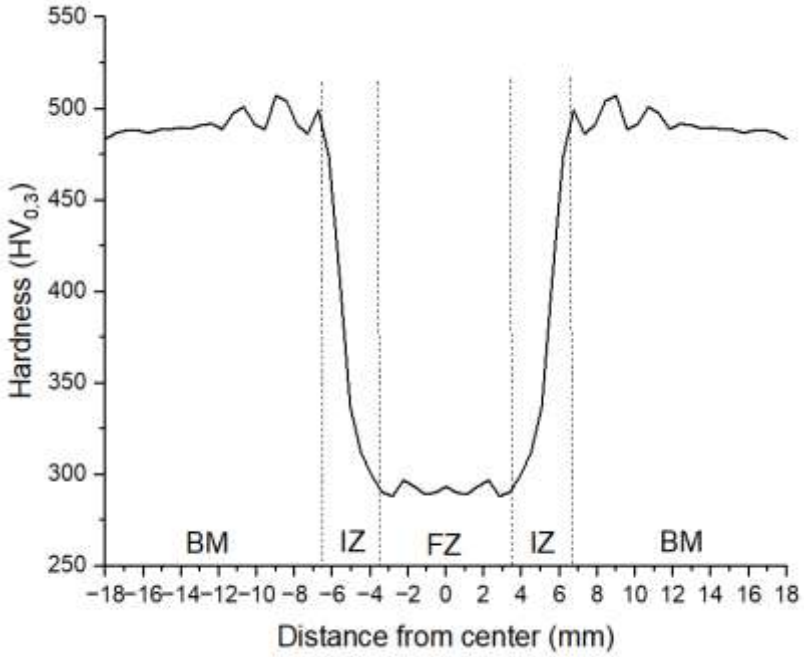

Figure 100 Hardness test results for TIG welded sample austempered

In *Figure 100* the hardness values of the different zones in the TIG specimen austempered are represented. Also in this case, 3 zones could be recognized: fusion zone, interface zone and base material zone. The fusion zone presents a hardness value up to 290-300 $HV_{0,3}$. The base material hardness is confirmed as the one corresponding to the nano-bainitic microstructure obtained after the austempering heat treatment, so 475 $HV_{0,3}$ [27].

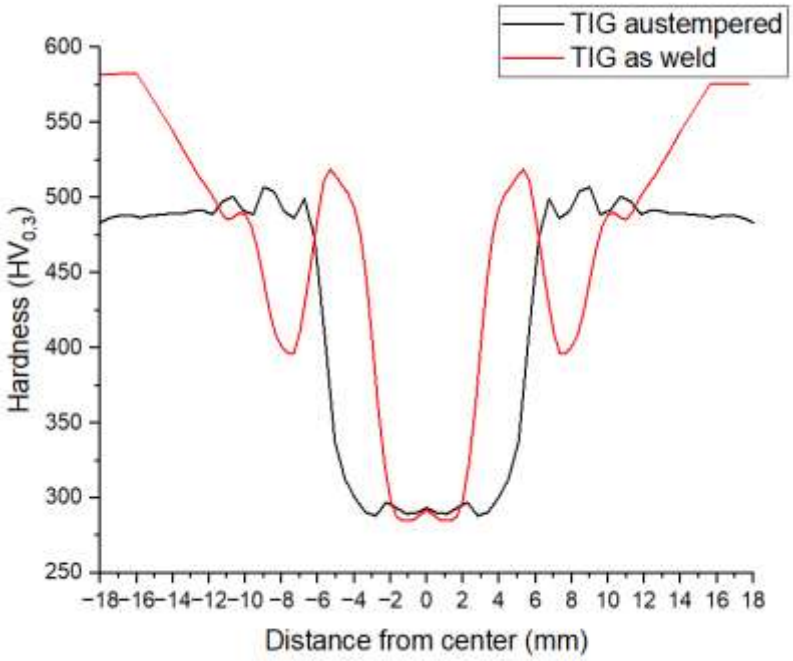

Figure 101 Comparison between hardness test results of TIG sample as weld and austempered

In the case of TIG welded samples, the influence of the austempering heat treatment on the microstructure evolution is very marked. This could be seen when the two condition 'as weld' and 'austempered' are compared, as in *Figure 101*. The peak of the hardness plot registered in the 'as weld' sample completely disappears in the 'austempered' specimen. In this last one, the zone corresponding to the hardness peak of the 'as weld', is represented by a progressive increase of the hardness value from the fusion zone one (290-300 $HV_{0,3}$) to the one of the base material (475 $HV_{0,3}$). When the TIG welded sample undergoes to the austempering heat treatment, also the valley in the hardness plot obtained in the 'as weld' specimen for the coarsened zone, is no more registered. Instead, in this zone the material hardness of the austempered specimen is stabilized at the base material value. This is due to the homogenization of the microstructure due to the austempering heat treatment.

In the comparison between the FZ of the 'as weld' and 'austempered' condition, it could be noted that basically the two zones have the same hardness value. This is traduced in a very low sensibility of the filler metal to the austempering heat treatment. This confirms also the considerations made in the previous SEM analysis of the TIG welded sample.

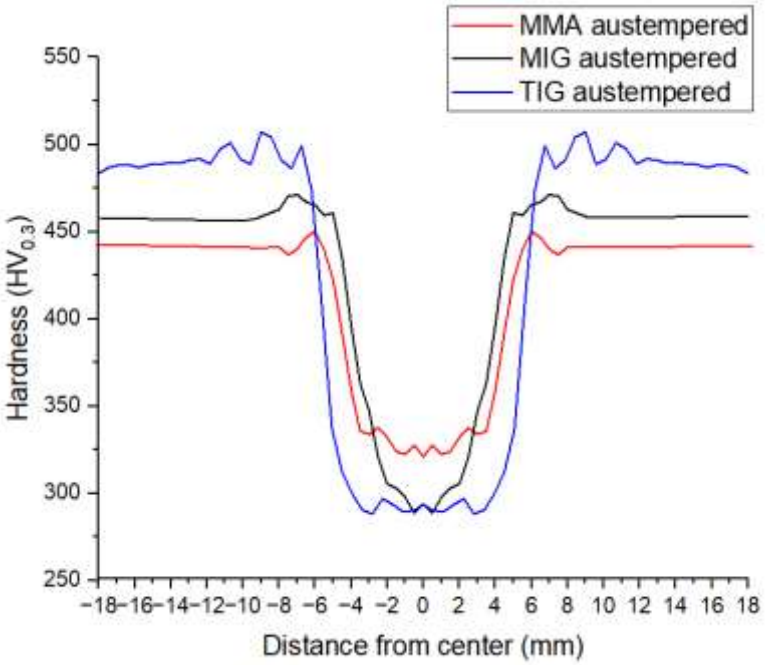

Figure 102 Comparison of the hardness tests results of TIG, MIG and MMA welded specimens austempered

In *Figure 102* the comparison between the hardness plots of the different analyzed austempered welded specimens is reported. The fusion zone hardness values of MIG and TIG results as 290-300 $HV_{0,3}$, which corresponds exactly to the one of the welded steels in the 'as weld' condition. This confirms that the filler metal microstructure is basically not influenced by the austempering heat treatment. Instead, in the case of MMA welded sample austempered, the fusion zone hardness is higher. Since all the filler metals employed in the three different welding processes have essentially the same chemical composition, in particular the carbon content, it could be said that this can be probably justified as an effect of the austempering heat treatment.

The hardness charts in *Figure 94* and *Figure 102* presents a fundamental similarity. This concerns the effect of the heat input on the width of the microstructural alteration of the material due to the welding processes. In fact, also in the case of austempered welded specimens, the TIG one presents a wider influenced zone, in terms of hardness, in comparison with the other two. This is also the one that presents the highest heat input of all welding procedures. Taking the MIG welded sample austempered, this presents the narrowest influenced zone, which is justified by the lowest heat input registered in the welding process in comparison with the other two.

The TIG welded samples austempered microstructure were examined with XRD diffractometer for phase identification and quantification.

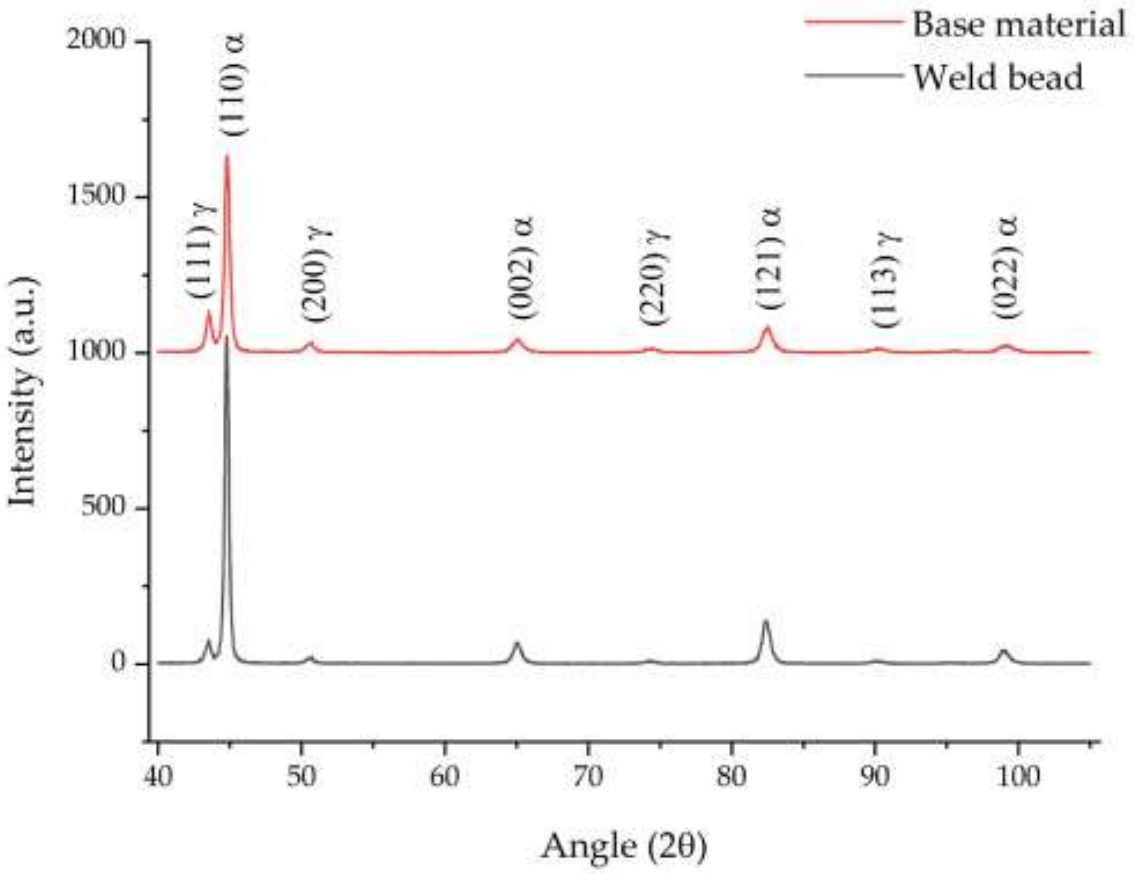

Figure 103 XRD pattern resulted of phase identification of TIG sample 'austempered'

Zone	V_γ	X_γ	V_α	X_α	$V_{\alpha'}$	$X_{\alpha'}$	$V_{\alpha b}$	$X_{\alpha b}$
Weld bead	9.81	1.16	51.40	0.03	38.77	0.17	-	-
Base material	24.08	1.02	-	-	-	-	75.01	1.02

Table 22 Results of XRD phase quantification of TIG sample 'austempered'. V_γ, volume fraction of retained austenite, X_γ, carbon content wt. % in retained austenite, V_α, volume fraction of α-ferrite, X_α, carbon content wt. % in retained austenite, $V_{\alpha'}$, volume fraction of martensite, $X_{\alpha'}$, carbon content wt. % in martensite, $V_{\alpha b}$, volume fraction of bainitic α-ferrite, $X_{\alpha b}$, carbon content wt. % in bainitic α-ferrite.

9. MIG welding process with heat-treated TRIP steel plates

9.1 Visualization and penetrating liquids

The bainitic steel plates, already treated with austempering heat treatment, are welded with MIG procedure. This was done to study the behavior of the base material nano-bainitic microstructure when it undergoes to the welding process heat cycles. It could be useful if, for example, a mechanical component with nano-bainitic microstructure needs to be welded in exercise.
The austempered steel plates welded together are represented in *Figure 104.*

Figure 104 Pictures of austempered steel plates welded with MIG welding process

The weld bead obtained with this second MIG welding process is equal to the one of the first that is conducted, this could be seen by the comparison between *Figure 82* and *Figure 28*. Also in this case, the glassy vein on top of the weld bead was obtained.

The penetrating liquids were conducted as first analysis of the welded plates. The resulted revealing of the red penetrating liquid is reported in *Figure 105*.

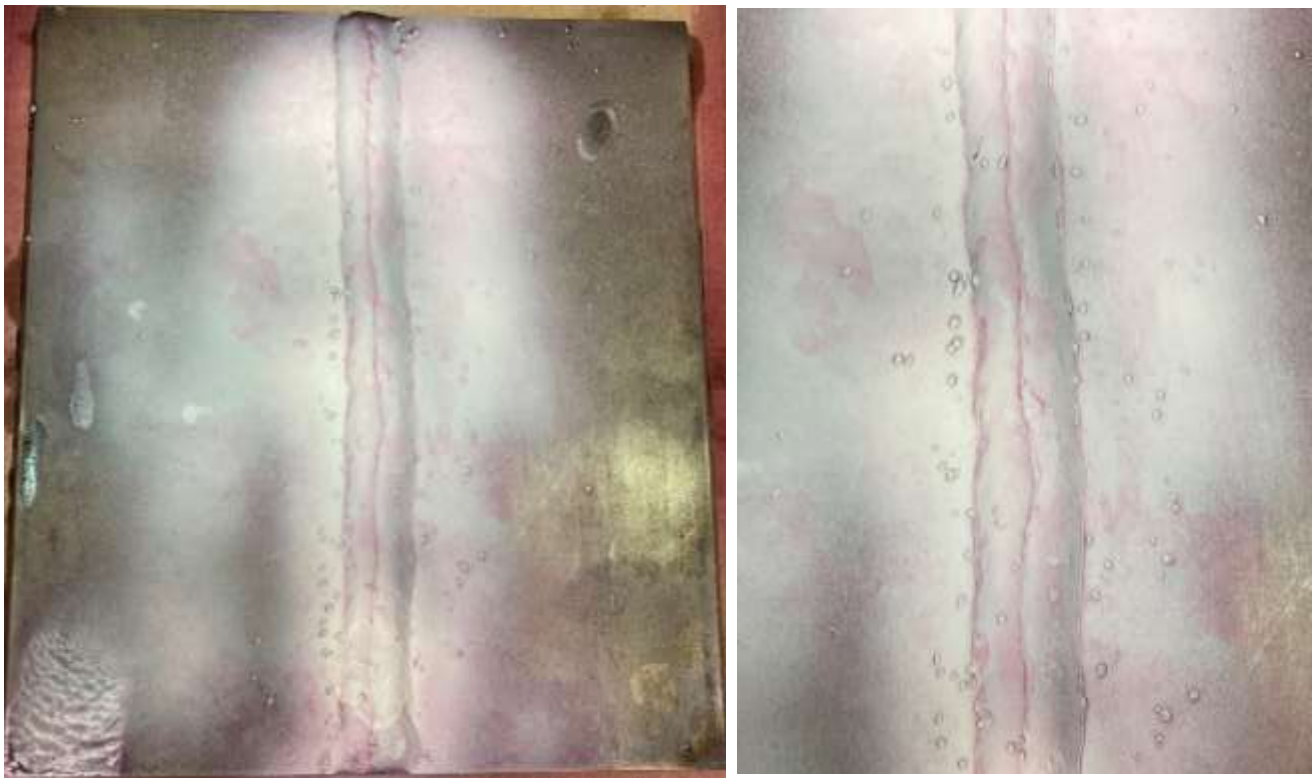

Figure 105 Penetrating liquids results on weld bead of MIG process on austempered steel plates

No marked cracks or cavities were revealed by the white spraying on the steel surface. For this reason, the welding process could be considered as acceptable, without the generation of hot cracking or cold cracking phenomena at least in the outside surface of the welded steels.

9.2 Residual stresses

The residual stresses, generated from the welding process heat cycles, were analyzed with the portable XRD diffractometer. The points where the stress situation was evaluated are reported in *Figure 106*. These are: point 0 on the center of the weld bead, point 1 at the weld bead base, points 2, 3, 4 distributed progressively far from the weld bead.

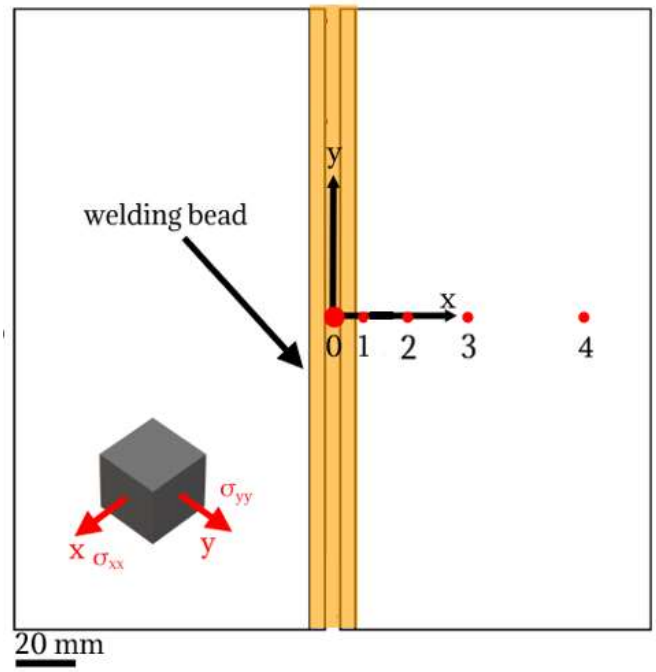

Figure 106 Distribution of residual stresses analyzed points on TRIP steel welded plates

POINT	Stress σ_φ in X plane [MPa]	Stress σ_φ in Y plane [MPa]
0	-116	510
1	-523	17
2	-392	-200
3	-365	-307
4	-735	-917

Table 23 XRD diffractometer results of residual stresses analysis on austempered TRIP steel plates joined with MIG process

The austempered welded plates presents, in the X plane direction of variation of ψ, a compressive stress situation in all the points analyzed. In particular, as it was expected, the compressive stress state is maximum at the point 4, where the tensile stress induced by the welding process is minimized. In the Y plane direction of analysis, the material presents in the point 0 and 1 a tensile stress situation. This is due to the effect of the welding direction that is in concordance to the one of residual stress evaluation in Y plane.

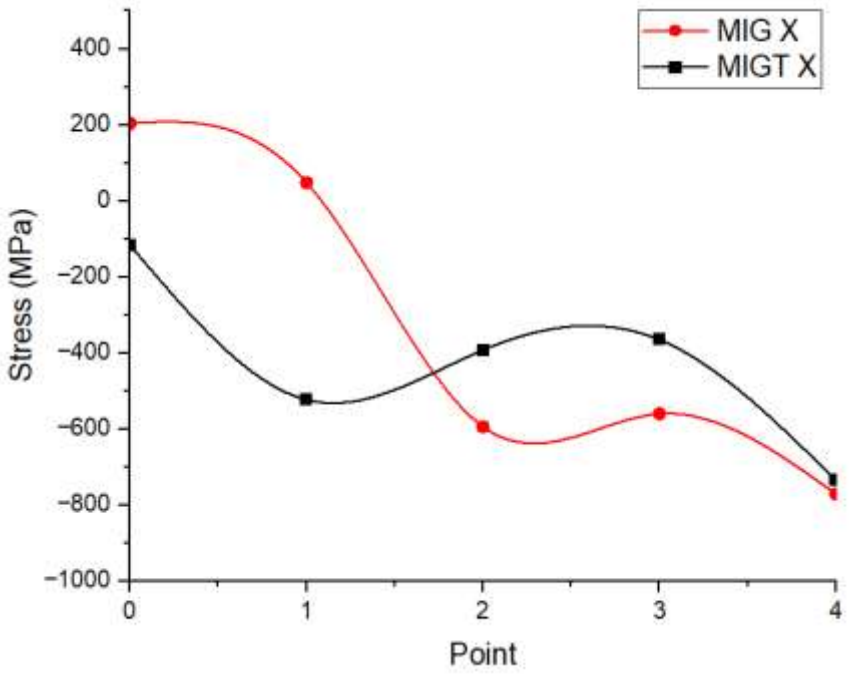

Figure 107 Comparison between residual stresses resulted for welded plates with MIG in the 'as received' condition (MIG) and austempered condition (MIGT) in X plane direction

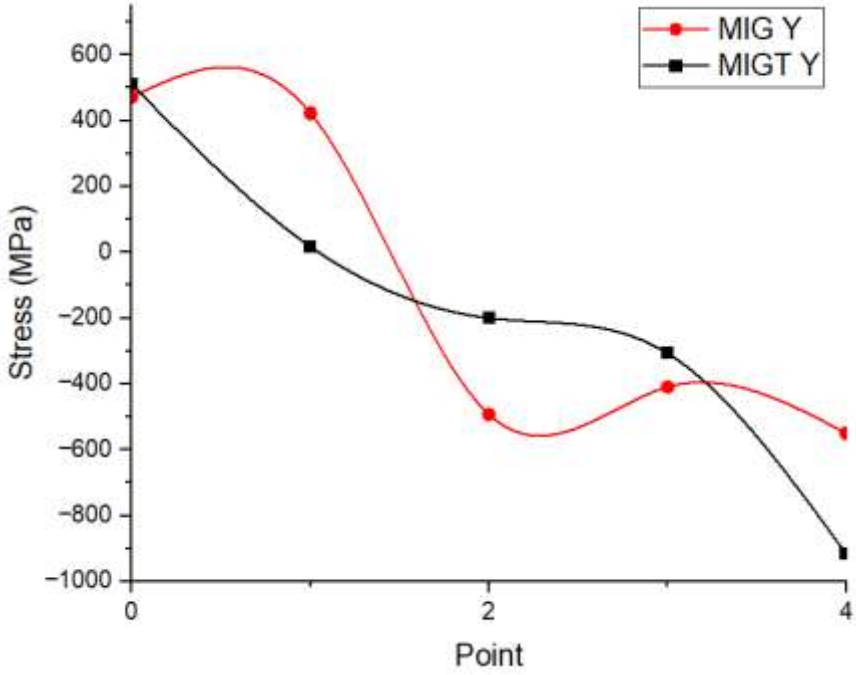

Figure 108 Comparison between residual stresses resulted for welded plates in the 'as received' condition (MIG) and austempered condition (MIGT) in Y plane direction

In the comparison between the XRD tests of the two samples, analyzed in X plane direction, it could be noted that the base material, so points 2, 3, 4, in the MIGT sample has a lower compressive stress situation in comparison with MIG sample, so less negative. This is traduced in a higher tensile stress induced by the welding process in the case of MIGT sample in comparison with the MIG one. The same situation is verified with the analysis of residual stresses in Y direction (a part for the point 4).

9.3 Optical and SEM microscopy

The microstructure of the MIGT welded sample was analyzed at the optical microscope. The steel surface, after being grinded and polished, was etched with Klemm's I chemical attack for the revealing of the different altered zones.

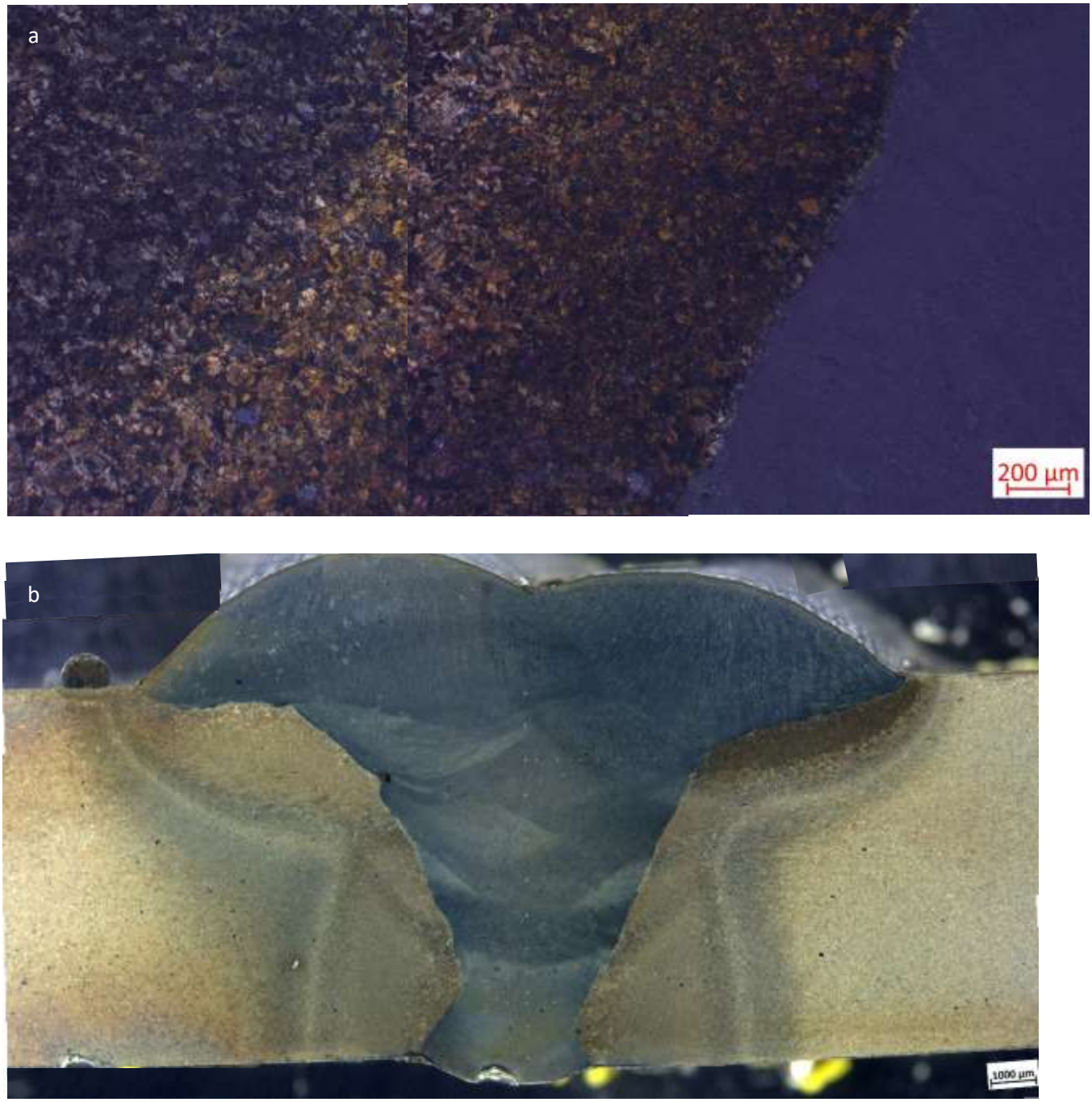

Figure 109 Optical microscope picture of heat affected zone (a), picture of welded section of MIGT sample (b)

The microstructure of the fusion zone and the heat affected zone of the MIGT sample is showed in *Figure 109 a.* The fusion zone is represented in blue on the right side of the image. The heat affected zone shows an initial mixing-coarsened zone and the central refined zone. The secondary coarsened zone in the MIGT sample is not obtained, as could be stated also by the hardness profile evaluated for that sample. This is due to the lower sensibility to the decomposition after welding heat cycles of the bainite in comparison with martensite.

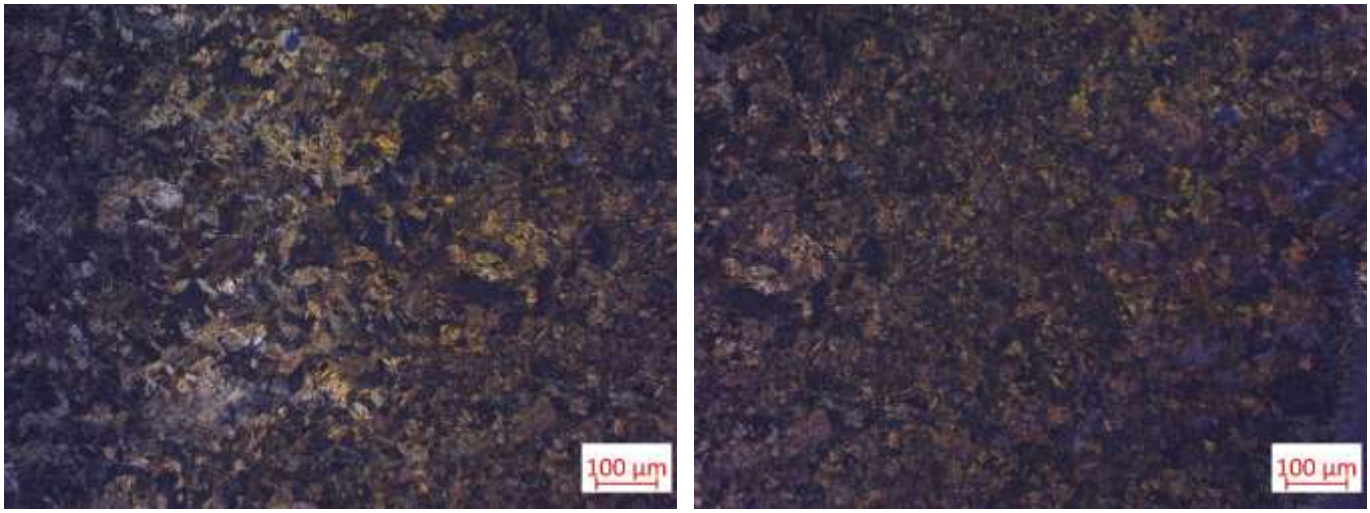

Figure 110 Optical microscope pictures of MIGT sample heat affected zone

The microstructure of the bainitic steel plates austempered joined with MIG welding processes (MIGT sample) was examined with Scanning Electron Microscope.

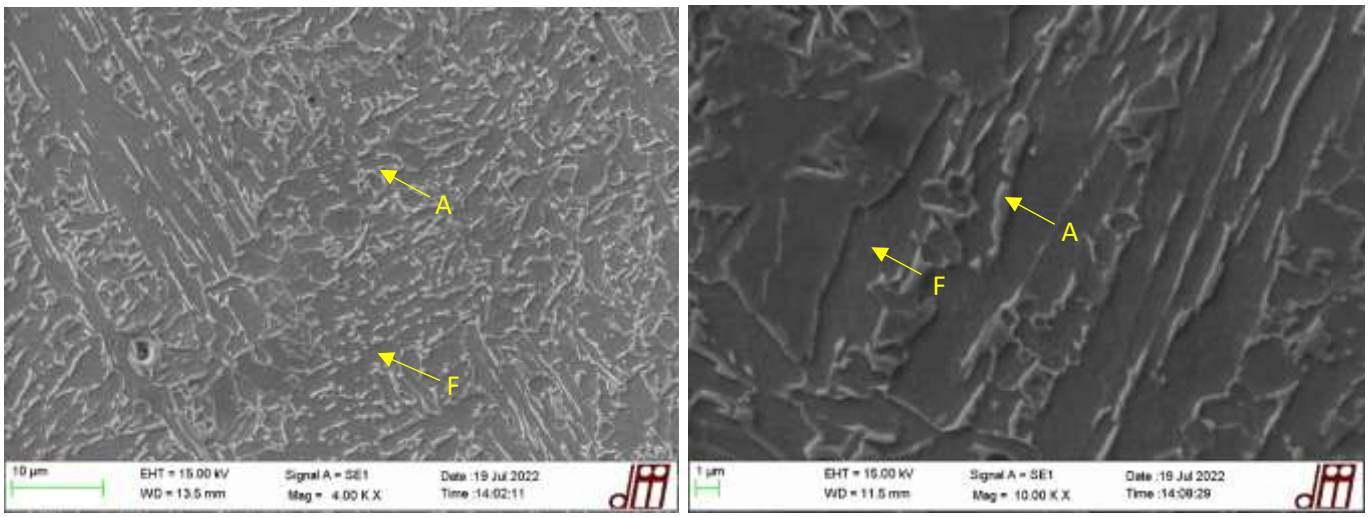

Figure 111 SEM pictures of MIGT fusion zone. A austenite, F ferrite

Since the chemical composition of the filler metal employed for the MIGT sample is very similar to the ones of the other welding processes, so with a very low carbon content, the microstructure obtained is composed by a ferritic matrix with austenite islands.

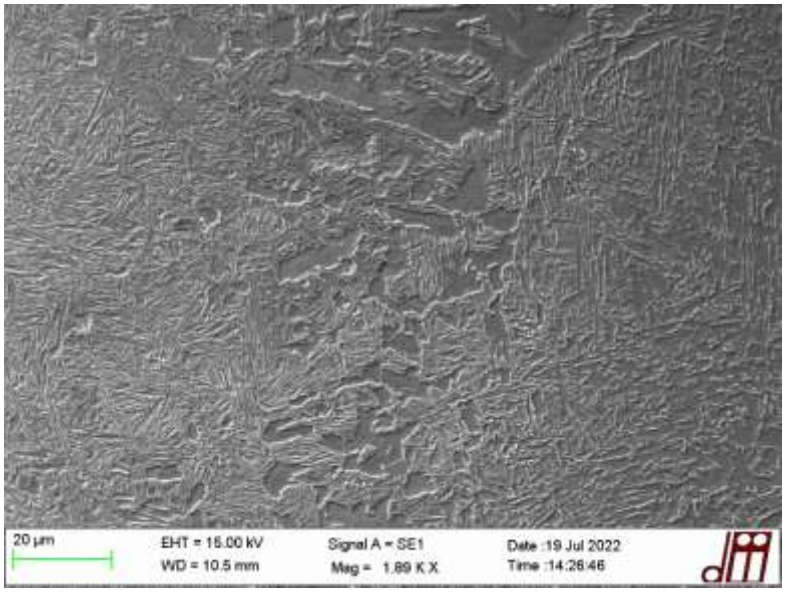

Figure 112 SEM picture of MIGT sample interface mixing zone

In *Figure 112* it could be seen the interface mixing zone between the base material, on the left, and the fusion zone, on the right. Also in this case, the carbon depletion causes the generation of ferritic islands and a reduction of the bainite content in correspondence of the IMZ.

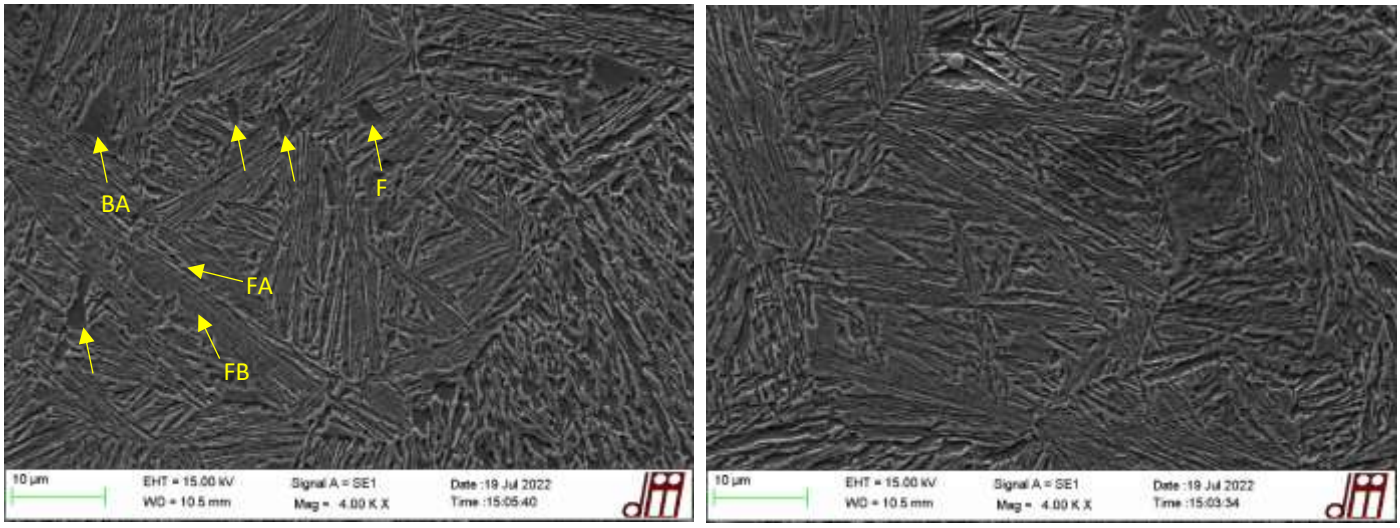

Figure 113 SEM pictures of MIGT sample base material microstructure. F ferrite, BA blocky austenite, FA film austenite, FB, ferritic bainite

In the microstructure obtained in the base material zone of the MIGT sample, the different phases that compose the nano-bainitic structure could be recognized. In comparison with the ones obtained with the other welded samples, there is a lower amount of blocky retained austenite islands.

Moreover, isolated ferritic grains are detected. These could be caused by a prolonged permanence of the bainitic steel plates at high temperatures during the austempering heat treatment, which generate pro-eutectoid ferrite grains.

9.4 Hardness

The hardness of the austempered bainitic steel welded plates with MIG welding process was examined with Vickers micro-hardness test. The indentations are taken at 1.5-2 mm from the top of the weld bead, the same position as the other samples analyzed. For the test a 300g load wass employed.

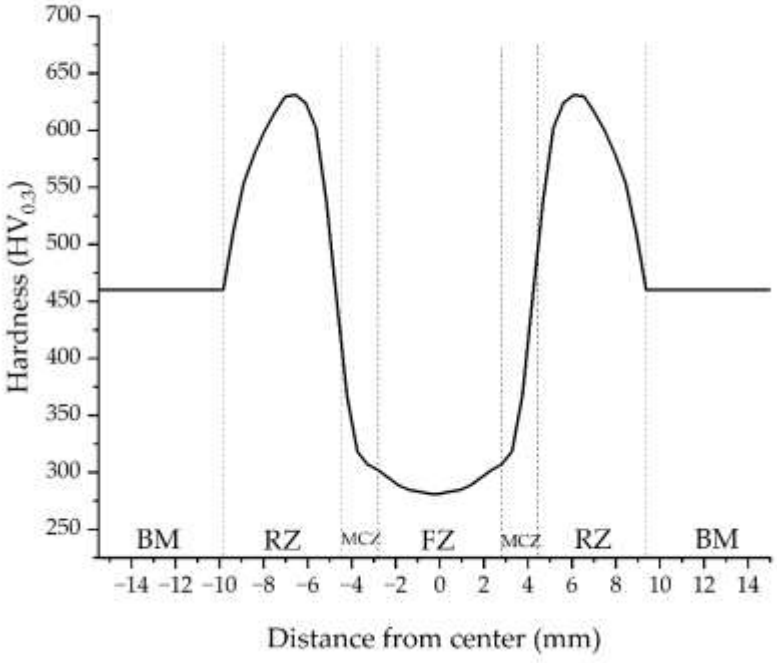

Figure 114 Hardness test results of austempered steel plates MIG welded

The resulted hardness plot from the hardness test conducted on the austempered welded steel plates could be subdivided into 4 zones: the fusion zone FZ, the mixing coarsened zone MCZ, the refined zone RZ, the base material zone BM. The hardness values obtained in the FZ is up to 300 $HV_{0,3}$ on average. The MCZ has a value slightly higher than that, of about 310-320 $HV_{0,3}$. The hardness peak obtained in the RZ reaches a value of 630 $HV_{0,3}$. Successively, the material hardness reduced to a value of 450-460 $HV_{0,3}$ in the BM, which is the one corresponding to the nano-bainitic microstructure obtained with the 'asutempering' heat treatment [27].

.

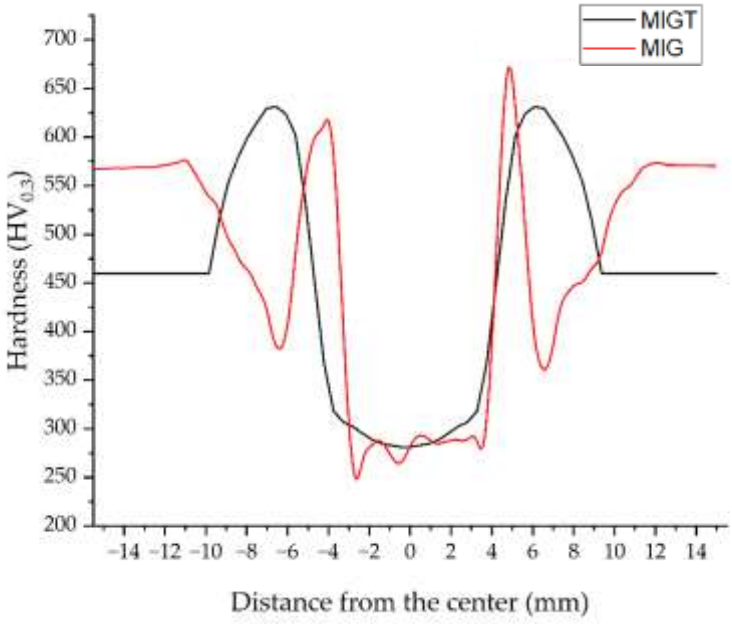

Figure 115 Comparison of hardness test results of MIG welded plates (MIG) and austempered MIG welded plates (MIGT)

In *Figure 115* the comparison between the hardness tests results of MIG welded steel plates and austempered MIG welded steel plates is represented. Since the material employed as filler metal of the solid wire is the same for both the welding processes, the hardness values resulted in the fusion zone of both samples corresponds to 290-300 $HV_{0,3}$. The material hardness plot of the two different samples results different in the heat affected zone. In the first MIG welded sample in the 'as received' state the material hardness reaches a peak in the refined zone and then progressively increase to the martensitic base material hardness after the altered base material zone. Instead, in the austempered MIG welded plates the material hardness follows a wider peak in the heat affected zone, which suddenly stabilizes at the base material hardness. This one is lower than the one of the martensitic microstructure of the first MIG welded sample. The hardness registered in both peaks of the two different samples are quite equals, this confirms that a similar microstructure composition is obtain in the two MIG welding process with different initial metallurgical condition of the bainitic steel plates.

9.5 XRD for phase identification and quantification

The MIGT sample microstructure is analyzed with XRD diffractometer.

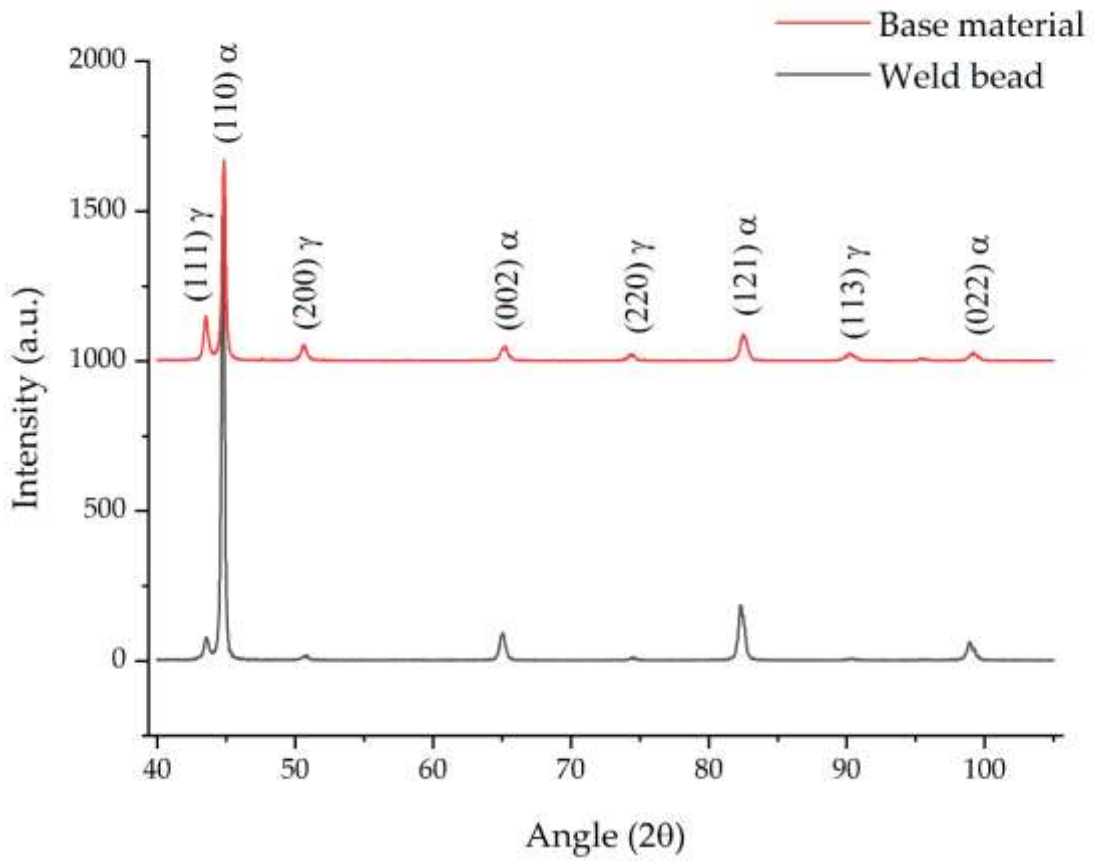

Figure 116 XRD pattern resulted for phase identification of MIGT welded sample

Zone	V_γ	X_γ	V_α	X_α	$V_{\alpha'}$	$X_{\alpha'}$
Weld bead	7.52	0.99	78.67	0.03	13.8	0.44
Base material	24.3	1.04	-	-	75.7	0.17

Table 24 Resuts of XRD for phase quantification of MIGT welded sample. V_γ, volume fraction of retained austenite, X_γ, carbon content wt. % in retained austenite, V_α, volume fraction of α-ferrite, X_α, carbon content wt. % in retained austenite, $V_{\alpha'}$, volume fraction of martensite, $X_{\alpha'}$, carbon content wt. % in martensite

The microstructure of the weld bead is mainly composed by α-ferrite. The content of austenite and martensite is in concordance with the ones obtained for the other welded specimens.

10. Conclusions

The main objective of this study, so to verify the feasibility of different welding processes with bainitic steel, could be considered as successfully achieved.

- From the initial analysis of the welded steel plates in the INE S.p.A. laboratories, during all passes of the welding processes and in the successive cooling stage, no marked defects or failures was detected.
- In the examination of the weld bead surface with the penetrating liquids, the presence of cracks or cavities was not detected for all the three different welded samples. This is traduced as a good attitude, from a macroscopical point of view, of the bainitic steel to be subjected to a welding procedure.
- The analysis of the different section of the welded samples with MIG, MMA and TIG welding processes at the optical and SEM microscope has permitted to give a better assessment of the bainitic steel behavior when it undergoes to the welding procedures, and how it interacts with the dissimilar low-carbon steel that composes the filler metal. From the optical and SEM microscope analysis of the different samples, only isolated porosities are detected, in particular in the MMA welded samples. For this reason, it could be said, since no cracks are detected, that the bainitic steel didn't present the generation of cold- or hot- cracking phenomena.

For the reasons mentioned above, the bainitic steel could be welded without particular difficulties.
In this study on the weldability of bainitic steels a deeper analysis on the base material and filler metal properties was conducted.

- The XRD diffractometry for residual stresses analysis show that the welding processes induces a tensile stress on the bainitic steel plates. This is confirmed by the lower compressive state of the welded plates in comparison with the original ones. The analysis shows the correlation between the heat input and the stress situation induced. In particular, the bainitic steel plates resulted more stressed with TIG welding procedure, where the heat input is the highest, in comparison with MMA and MIG.
- The hardness tests have returned promising results, in concordance to what is expected as the behavior of the different materials to the heat treatments at which are subjected. In particular, the hardness of the base material, so the bainitic steel, resulted always higher in comparison with the one of the fusion zone, so the low-carbon steel of the filler metal. From this, it could be said that weld bead is the weakest zone of the whole structure. On the other hand, the only defects and isolated porosities, detected with the microscopical analysis, have been observed

in the interface zone between the filler metal and the base material. These could be cracks initiation sites that cause premature failure in exercise.

- The tensile tests show that, in general, MMA welded samples are characterized by the highest mechanical properties, individuated in yield strength and ultimate tensile strength UTS. The better mechanical properties obtained in the MMA welded sample could be justified by the higher heat input that cause wider extension of the material alteration. In particular, the carbon migration in the fusion zone could be enhanced, which led to an increase in the strength of this zone where all the welded samples are fractured. However, a deeper investigation must be conducted to better assess the mechanical behavior of the different welded samples.

11. Bibliography and Sitography

[1] P. V. Moghaddam, J. Hardell, E. Vuorinen, and B. Prakash, "The role of retained austenite in dry rolling/sliding wear of nanostructured carbide-free bainitic steels," *Wear*, vol. 428–429, no. November 2018, pp. 193–204, 2019, doi: 10.1016/j.wear.2019.03.012.

[2] J. Chiang, B. Lawrence, J. D. Boyd, and A. K. Pilkey, "Effect of microstructure on retained austenite stability and work hardening of TRIP steels," *Mater. Sci. Eng. A*, vol. 528, no. 13–14, pp. 4516–4521, 2011, doi: 10.1016/j.msea.2011.02.032.

[3] Weld GURU, "MIG vs TIG welding: the main differences." https://weldguru.com/mig-vs-tig-welding/

[4] H. K. D. H. Bhadeshia and J. W. Christian, "Bainite in steels," *Metall. Trans. A*, vol. 21, no. 3, pp. 767–797, 1990, doi: 10.1007/BF02656561.

[5] H. K. D. H. Bhadeshia, "Properties of fine-grained steels generated by displacive transformation," *Mater. Sci. Eng. A*, vol. 481–482, no. 1-2 C, pp. 36–39, 2008, doi: 10.1016/j.msea.2006.11.181.

[6] A. Królicka, A. M. Żak, and F. G. Caballero, "Enhancing technological prospect of nanostructured bainitic steels by the control of thermal stability of austenite," *Mater. Des.*, vol. 211, 2021, doi: 10.1016/j.matdes.2021.110143.

[7] R. A. Cottis, "Hydrogen embrittlement," *Shreir's Corros.*, pp. 902–922, 2010, doi: 10.1016/B978-044452787-5.00200-6.

[8] Welding answers, "Hot cracking vs cold cracking." https://weldinganswers.com/hot-cracking-vs-cold-cracking/

[9] N. Krishna Murthy and G. D. Janaki Ram, "Hot cracking behavior of carbide-free bainitic weld metals," *Mater. Des.*, vol. 92, pp. 88–94, 2016, doi: 10.1016/j.matdes.2015.12.020.

[10] ESABNA, "MIG handbook", [Online]. Available: https://www.esabna.com/euweb/mig_handbook/592mig3_2.htm

[11] M. K. Wibowo, "Welding of TRIP steels," *Dairy Sci. Technol. CRC Taylor Fr. Gr.*, vol. 43, no. June, p. 99, 2015.

[12] K. Weman, "Manual metal arc (MMA) welding with coated electrodes," *Weld. Process. Handb.*, pp. 99–103, 2012, doi: 10.1533/9780857095183.99.

[13] M. A. Wahab, *Manual Metal Arc Welding and Gas Metal Arc Welding*, vol. 6. Elsevier, 2014. doi: 10.1016/B978-0-08-096532-1.00610-5.

[14] Melezy, "Preheating and interpass temperature: importance, benefits, effects on properties." https://melezy.com/preheating-and-interpass-temperature-importance-benefit/

[15] N. Jeyaprakash, A. Haile, and M. Arunprasath, “The Parameters and Equipments Used in TIG Welding: A Review,” *Int. J. Eng. Sci.*, pp. 2319–1813, 2015, [Online]. Available: www.theijes.com

[16] Welding empire, “Tungsten electrodes: how to select size & type.” https://www.weldingempire.com/tungsten-electrodes/

[17] AXXAIR, “The different types of electrodes used in orbital TIG welding.” https://www.axxair.com/en/blog/the-different-types-of-electrodes-used-in-orbital-tig-welding#:~:text=Thorium-Tungsten (yellow 1%25,better emissivity of the electrons

[18] Technoweld, “Type and size of electrode for GTAW.” https://technoweld.com.au/2019/09/18/what-type-and-size-of-electrode-should-you-use-for-gtaw-and-why/

[19] A. K. Singh, V. Dey, and R. N. Rai, “Techniques to improveweld penetration in TIG welding (A review),” *Mater. Today Proc.*, vol. 4, no. 2, pp. 1252–1259, 2017, doi: 10.1016/j.matpr.2017.01.145.

[20] M. Tanaka, S. Tashiro, T. Satoh, A. B. Murphy, and J. J. Lowke, “Influence of shielding gas composition on arc properties in TIG welding,” *Sci. Technol. Weld. Join.*, vol. 13, no. 3, pp. 225–231, 2008, doi: 10.1179/174329308X283929.

[21] A. Królicka, A. Ambroziak, and A. Zak, “Welding capabilities of nanostructured carbide-free bainite: Review of welding methods, materials, problems, and perspectives,” *Appl. Sci.*, vol. 9, no. 18, pp. 1–15, 2019, doi: 10.3390/app9183798.

[22] K. Fang, J. G. Yang, K. J. Song, X. S. Liu, J. J. Wang, and H. Y. Fang, “Study on tempered zone in nanostructured bainitic steel welded joints with regeneration,” *Sci. Technol. Weld. Join.*, vol. 19, no. 7, pp. 572–577, 2014, doi: 10.1179/1362171814Y.0000000227.

[23] P. Sabbadin and A. Campagnolo, “Theory and measuring procedure for the residual stresses assessment based on X-Ray diffraction,” 2017.

[24] Y. Y. You, R. K. Shiue, R. H. Shiue, and C. Chen, “The study of carbon migration in dissimilar welding of the modified 9Cr-1Mo steel,” *J. Mater. Sci. Lett.*, vol. 20, no. 15, pp. 1429–1432, 2001, doi: 10.1023/A:1011616232396.

[25] P. Mayr, C. Schlacher, J. A. Siefert, and J. D. Parker, “Microstructural features, mechanical properties and high temperature failures of ferritic to ferritic dissimilar welds,” *Int. Mater. Rev.*, vol. 64, no. 1, pp. 1–26, 2019, doi: 10.1080/09506608.2017.1410943.

[26] S. Wang, Q. Ma, and Y. Li, “Characterization of microstructure, mechanical properties and corrosion resistance of dissimilar welded joint between 2205 duplex stainless steel and 16MnR,” *Mater. Des.*, vol. 32, no. 2, pp. 831–837, 2011, doi: 10.1016/j.matdes.2010.07.012.

[27] M. Franceschi *et al.*, “Effect of intercritical annealing and austempering on the microstructure and mechanical properties of a high silicon manganese steel,” *Metals (Basel).*, vol. 10, no. 11, pp. 1–19, 2020, doi: 10.3390/met10111448.

[28] F. G. Caballero, M. K. Miller, and C. Garcia-Mateo, “Carbon supersaturation of ferrite in a nanocrystalline bainitic steel,” *Acta Mater.*, vol. 58, no. 7, pp. 2338–2343, 2010, doi: 10.1016/j.actamat.2009.12.020.

[29] J. Jiang, Z. Y. Peng, M. Ye, Y. B. Wang, X. Wang, and W. Bao, “Thermal Effect of Welding on Mechanical Behavior of High-Strength Steel,” *J. Mater. Civ. Eng.*, vol. 33, no. 8, pp. 1–16, 2021, doi: 10.1061/(asce)mt.1943-5533.0003837.

[30] G. Madhusudhan Reddy, T. Mohandas, and K. K. Papukutty, “Effect of welding process on the ballistic performance of high-strength low-alloy steel weldments,” *J. Mater. Process. Technol.*, vol. 74, no. 1–3, pp. 27–35, 1998, doi: 10.1016/S0924-0136(97)00245-8.

Ringraziamenti

Ringrazio il relatore di tesi Prof. Dabala', il correlatore Franceschi Mattia per avermi aiutato durante il progetto. Ringrazio Carbone Massimiliano, e tutti i professori che hanno partecipato al lavoro di tesi. Ringrazio Miotti Alvise e tutti i tecnici di INE S.p.A. Ringrazio la mia famiglia e i miei amici per avermi sostenuto e accompagnato in tutto il mio percorso.